

PION INDUCED PION PRODUCTION ON OXYGEN AT 280 MEV

By

FRANCIS MARTIN ROZON

B.Eng. (Phys.), University of Saskatchewan, 1983,

M.Sc., University of British Columbia, 1985,

A THESIS SUBMITTED IN PARTIAL FULFILLMENT OF
THE REQUIREMENTS FOR THE DEGREE OF
DOCTOR OF PHILOSOPHY

in

THE FACULTY OF GRADUATE STUDIES

Department of Physics

We accept this thesis as conforming
to the required standard

THE UNIVERSITY OF BRITISH COLUMBIA

September 1988

© Francis Martin Rozon, 1988

In presenting this thesis in partial fulfilment of the requirements for an advanced degree at the University of British Columbia, I agree that the Library shall make it freely available for reference and study. I further agree that permission for extensive copying of this thesis for scholarly purposes may be granted by the head of my department or by his or her representatives. It is understood that copying or publication of this thesis for financial gain shall not be allowed without my written permission.

Department of PHYSICS

The University of British Columbia
1956 Main Mall
Vancouver, Canada
V6T 1Y3

Date SEPT. 6, 1988

Abstract

A first coincident measurement of the pion induced pion production reaction cross-section on a complex nucleus ($A > 2$) has been successfully performed. In particular, the reaction $^{16}\text{O}(\pi^+, \pi^+\pi^-)$ was measured at 280 MeV incident pion energy. The only previous published measures of this reaction on nuclei consisted of a dated measurement done on emulsion nuclei [BBD*69] and did not provide very stringent limits to the nuclear cross section. Single arm experiments have previously been done elsewhere on the proton [BJK*80] and the deuteron [PGM*84].

The reaction was measured at TRIUMF using the QQD magnetic spectrometer in coincidence with the CARUZ [RGR88], a total absorption scintillator range telescope. The measured four-fold differential cross sections were extrapolated to the unmeasured portions of the phase-space to extract the total reaction cross-section at 280 MeV, which was found to be

$$\sigma_{tot} = 2.250 \pm .350 mb.$$

The $(\pi, 2\pi)$ cross-section is thus observed to provide approximately 40% of the inclusive double charge exchange cross section [Woo84] at this energy.

The model of [OV86] is found to explain many of the features of the data, including σ_{tot} . The present data do not preclude effects due to pion condensate precursor phenomena as proposed by [CE83] but they do not support the existence of a strong effect. The data are also compared to kinematical Monte Carlo simulations of some possible reaction mechanisms and it is found that the presence of an intermediate Δ can aid the explanation of the low energy features

of the π^+ energy spectrum.

Table of Contents

Abstract	ii
List of Tables	vii
List of Figures	ix
Acknowledgements	xii
 I Introduction	 1
I.1 An Introduction to $\pi - \pi$ Scattering and the $(\pi, 2\pi)$ Reaction . . .	3
I.2 Summary	15
 II The Experiment	 16
II.1 Beamlines and Beam Monitoring	16
II.1.1 M13	17
II.1.2 M11	17
II.1.3 Beam Counters	18
II.2 Experimental Apparatus	21
II.2.1 The QQD	21
II.2.2 The CARUZ	25
II.2.3 Targets	30
II.3 Data Acquisition and Electronics	31
II.3.1 Data Acquisition	33
II.3.2 QQD Electronics	34
II.3.3 CARUZ Electronics	36
II.3.4 Computer Event Logic and Beam Electronics	38

III Data Reduction	42
III.1 Calibration	42
III.1.1 Beam Monitor Calibrations	43
III.1.2 QQD Calibration	47
III.1.2.1 Delta Coefficients	48
III.1.2.2 Momentum Acceptance	53
III.1.2.3 Removal of QQD Backgrounds	56
III.1.3 CARUZ Calibration	59
III.1.3.1 Pulse Response and TOF	61
III.1.3.2 Energy Calibration and Mass Separation	67
III.2 Cross Sections	75
III.2.1 Calculating Four-Fold Differential Cross Sections	79
III.2.2 Integrated Cross Sections	80
III.2.3 Contribution of Backgrounds	90
IV Theoretical Approaches and Simulations	93
IV.1 The Free ($\pi, 2\pi$) Reaction	93
IV.2 ($\pi, 2\pi$) as a Nuclear Probe	97
IV.3 Monte Carlo Reaction Simulations	117
V The Results	123
V.1 Total Cross Section	123
V.2 Differential Cross Sections	124
V.2.1 Positive Pion Spectra	125
V.2.2 Negative Pion Spectra	132
V.2.3 Missing Mass	134
V.3 Summary	135

Bibliography	140
A Tabulations of Differential Cross Sections	148
B Delta Coefficients	155

List of Tables

I	Table of the dimensions of the CARUZ components and their distances to the scattering target location.	28
II	A table of various targets employed in the $(\pi, 2\pi)$ experiment indicating their thicknesses.	31
III	Summary of reference ^{12}C elastic scattering cross sections at 50° (lab angle) used to obtain the QQD solid angle as a function of momentum. The errors quoted include normalization errors where given.	55
IV	Table of the coefficients used to describe the QQD momentum acceptance.	58
V	Response data for the CARUZ. The values in parentheses include the response of the CARUZ to decay muons from the stopped pions. The response is given in arbitrary units as determined by the electron calibration discussed in the text.	66
VI	Correction factors for extrapolating the π^+ energy spectra in the CARUZ and the π^- spectra in the QQD.	83
VII	The single differential cross sections as a function of the angle of the π^- and the corresponding error. The error includes statistical errors as well as errors from the previous extrapolations.	88
VIII	Errors present in the $(\pi, 2\pi)$ experiment, given in percentages. . .	89
IX	The four-fold differential cross section (units of $\text{nb}/(\text{sr}^2 \text{ MeV}^2)$) as a function of T_{π^+} for the three QQD angle settings. The data includes both QQD momentum settings and both CARUZ angle settings.	149
X	The triple differential cross section (units of $\text{nb}/(\text{sr}^2 \text{ MeV})$) as a function of T_{π^-} for the three QQD angle settings. The data includes both CARUZ angle settings.	150
XI	The double differential cross section (units of $\mu\text{b}/\text{sr}^2$) as a function of θ_{π^+} for the three QQD angle settings. The data includes both QQD momentum settings.	151
XII	The four-fold differential cross section (units of $\text{nb}/(\text{sr}^2 \text{ MeV}^2)$) as a function of T_{π^+} for the three QQD angle settings. The data includes only the high QQD momentum, 50° CARUZ setting. . .	152
XIII	The triple differential cross section (units of nb/sr^2) as a function of θ_{π^+} for the three QQD angle settings. The data includes only the high QQD momentum, 50° CARUZ setting.	153

XIV	The triple differential cross section (units of nb/(sr ² MeV)) as a function of T_{π^-} for the three QCD angle settings. The data includes only the 50° CARUZ angle setting.	154
XV	Coefficients for the δ_4 calculation in terms of the front wire chamber coordinates and WC4X with terms to second order in chamber coordinates and in δ	156
XVI	Coefficients for the δ_5 calculation in terms of the front wire chamber coordinates and WC5X.	157

List of Figures

1	The a) one point pion pole, b) one point pion contact, c) two point and d) three point diagrams contributing to the phenomenological Lagrangian typically used in describing the free $(\pi, 2\pi)$ reaction. . .	7
2	The energy dependence of the $p(\pi^-, \pi^+)$ reaction cross section data from [BJK*80]. The curve is a polynomial fit to the data in terms of the integrated phase-space and energy above threshold (see [BJK*80]).	9
3	The energy dependence of the total cross section, σ_{tot} , as calculated by the various authors discussed in the text. Results are shown for both of the production reactions $^{16}O(\pi^+, \pi^+\pi^-)$ and $^{18}O(\pi^-, 2\pi^-)$. .	14
4	Configuration of the M11 channel.	19
5	Showing the QQD, the CARUZ and the various beam monitors. . .	23
6	A close view of the CARUZ showing the relative sizes and positions of the components.	27
7	A scale drawing of the gelled water target used for the $(\pi, 2\pi)$ measurement.	32
8	A diagram of the QQD related electronics. The key in the figure defines the symbols used for the CAMAC and NIM components. . .	35
9	The electronics used for the CARUZ section of the apparatus. The key is the same as for Figure 8. PD denotes a passive divider. . . .	37
10	Showing the final LAM definition, computer related electronics, and electronics for the beam monitoring. The key is the same as for Figure 8. Delays are not shown.	39
11	A typical M11 TOF spectra at incident pion kinetic energy of 84 MeV used to separate pions from electrons and muons in the incident beam at low channel energies.	44
12	The measured hodoscope and in-beam counter flux corrected for multiple pions per beam burst versus the width of the horizontal jaw in the channel. The shape follows that of the expected flux for the channel settings as given in [TUH87].	46
13	Showing the QQD wire chamber traceback to the empty target to establish cuts for background elimination from the target frame. . .	49
14	A typical energy spectrum obtained from the calculated δ for the nominal 0% elastic scattering run on ^{12}C	52
15	A typical DDIF spectrum, the difference between δ_4 and δ_5 , showing the applied cuts, which is used to aid in removing pions which decay to muons during flight in the QQD. This spectrum also provides a measure of the QQD's intrinsic resolution without the effects of the finite beam energy width.	54

16	The measured momentum acceptance of the QQD spectrometer showing the solid angle as a function of the percentage change in the scattered pion momentum from the nominal central value.	57
17	Scatterplot of δ_5 against the timing in E1 corrected for the particle flight time in the CARUZ. The central energy of the QQD is 84 MeV. The $e - \pi$ separation is clear. The pion definition band shown is the intersection of the electron removal and pion TOF band cuts for this setting.	60
18	The response spectrum produced by 50 MeV stopping pions. The features of the spectrum are discussed in the text.	65
19	Showing the $\pi^+ - e^+$ mass separation in a velocity versus $E \cdot \Delta E$ plot for 128 MeV/c particles (50 MeV pions).	68
20	A TOF- $E \cdot \Delta E$ plot showing the separation of the pion and protons in the CARUZ. Some deuterons are also visible.	69
21	A TOF-E plot showing the $\pi^+ - p$ (and deuteron, d) separation where π^+ , p and d are denoted by squares, plusses and diamonds respectively. The particles were mass-identified from the E- ΔE plot. .	70
22	Response of the CARUZ to positrons (circles), stopping pions with decay muon (diamond) and linear fit (dash-dot line), stopping pions alone (squares) and Birk's formula fit (solid line), stopping protons (triangles) and Birk's formula fit (dotted line). Error bars are smaller than the drawn points. See text for more details.	72
23	The target loss correction as calculated by the method from [CSZ76]	78
24	The measured energy distribution of π^+ in the CARUZ with the full data set with the QQD at 50° and the fitted polynomial. The fitting constraints are discussed in the text.	82
25	The measured energy distribution of π^- in the QQD at 50° . The curve represents the fitted polynomial. Data point errors are statistical.	84
26	The angular distribution of π^+ in the CARUZ for the QQD at each of the three settings with the fitted Legendre polynomial series to extrapolate to undetected portions of the angular phase space. . . .	86
27	The angular distribution of π^- for the different QQD angular settings used in the experiment with the fitted Legendre polynomial series. .	87
28	Schematic representation of the $(\pi, 2\pi)$ reaction indicating the labelling for the particle momenta. The circular region contains the mechanisms described by the various forms of effective Lagrangians. The pions are shown as dashed lines, while the nucleons are shown as full lines.	95
29	Some of the 32 additional diagrams used in the model of [OV85] showing contributions due to the Δ , ρ , ϵ and N^* intermediate states.	98
30	A diagrammatic representation of nucleon-hole and Δ -hole excitations in the nuclear medium contributing to the pion self-energy. . .	100

31	Predictions for the $^{16}\text{O}(\pi^+, \pi^+\pi^-)$ reaction by the three authors discussed above compared to the experimentally evaluated total cross section. Note that the Rockmore curve (lower solid curve) contains the corrections discussed in the text. The square point is the measured datum.	105
32	A diagram showing the part of the pion-nucleus optical potential corresponding to a particle-hole- 2π excitation, used for the calculation of the $(\pi, 2\pi)$ process.	111
33	The $\Delta\Delta$ mechanism [BTWW82,SWB83] showing the formation of the $\Delta\Delta$ state and its decay into 4 nucleons or into two pions and two nucleons.	118
34	The energy spectrum of π^+ 's for the data set with the QQD at 50° . The thick solid line is the phase-space prediction. The two other curves are the results from [OV87] as discussed in the text.	126
35	The energy distribution of π^+ in the CARUZ for the CARUZ at 50° and the QQD at high momentum. The QQD is at a) 50° , b) 80° and c) 115° . The curves represent the model calculations of [OV87]. . . .	128
36	The energy distribution of π^+ in the CARUZ for 50° QQD data compared to the results of the intermediate Δ (solid) and $\Delta\Delta$ (dashed) reaction simulations.	130
37	The angular distribution of π^+ in the CARUZ. The QQD is at a) 50° , b) 80° and c) 115° . The thin solid curve is the Δ model prediction while the thick dashed and solid lines are results of [OV87].	131
38	The energy spectrum of π^- 's for the data sets with the QQD at a) 50° , b) 80° and c) 115° . The curves are results of [OV87] and are discussed in the text.	133
39	The missing mass spectrum for the two detected final state pions for the data set with the QQD at 50°	136

Acknowledgements

It is finally time to put some words down for an acknowledgement. I had decided early on in the writing of this thesis that this section would not go into the computer until all the other parts were completed. That time has come, though at one time it seemed far in the future. Writing this cumbersome document was tortuous at times, as it becomes difficult to think of different ways to say “we measured this” and other such phrases.

There are many people to thank for helping me in the completion of this work. Some of you I will name, whether you consent or not. The rest who are not named will just have to imagine that I’m talking about you. Dick Johnson supervised my tenure as a graduate student at UBC, first as a masters student and then a doctoral student, getting five years of work from me without having to pay a cent in salary. He did however graciously pay for my airline ticket to Italy so that I could attend the Piscat Cortina ski conference. Nevio Grion and Rinaldo Rui formed the Italian connection in this work. Their hard work made sure that pions were indeed produced. They also gave me enough per diem money in Italy to pay for my ski lift tickets. I would like to thank my external examiner for condemning my jargon filled english. But then, what the hell, I’m not an Englishman, eh! The distractions provided by the ongoing experiments of other graduate students and post-docs and questions about their analyses were much needed so that I could maintain some semblence of sanity. Lastly, I would like to thank my wife, Lori, for being here and for putting up with me while this was being written.

Chapter I

Introduction

The history of the pion dates to 1935 when Yukawa [Yuk35] proposed the existence of a meson to mediate the strong nuclear forces. It was not until 1947 that the pion was experimentally identified in cosmic ray experiments [LMOP47]. The pion proved soon after to be an interesting particle, existing in three charge states, π^+ , π^0 , π^- , thus having an isospin of 1, with masses of 139.56 MeV and 134.96 MeV for the charged and neutral states respectively. The pion is a boson, that is, it satisfies Bose statistical laws, and can be created or destroyed singly. This is true of any boson which has a zero net fermion (lepton or baryon) quantum number (other quantum numbers such as strangeness must also be conserved). A non-zero value prevents such absorption or creation phenomena for bosons like the α particle.

The pion is able to excite many resonances when interacting with nucleons. The $\Delta(1232)$ resonance (width $\Gamma \sim 115$ MeV) is the most easily recognized and is an important factor in almost any pion reaction channel for low to medium energy pions. The Δ exists in four charge states, the Δ^- , Δ^0 , Δ^+ and Δ^{++} , and is characterized by the average mass of the Δ quartet of 1232 MeV and by its quantum numbers of spin 3/2 and isospin 3/2.

The pion can undergo many types of interactions with nucleons or nuclei. The available reaction channels include elastic and inelastic scattering, absorption, single and double charge exchange (SCX and DCX) and pion production. The pion production channel, or $(\pi, 2\pi)$ to denote the single pion production reaction,

becomes the dominant inelastic channel above 600 MeV pion kinetic energy in the case of pion reactions on free nucleons. However, for the energy region of interest here, the $(\pi, 2\pi)$ reaction cross section is still quite small in comparison to nuclear pion reactions like absorption. The Δ remains an important factor for the description of π -nucleus reactions as can be ascertained from the resonant behaviour of the cross sections of various pion reaction channels in the Δ resonance region.

The coupling strengths of the π -N to Δ given by the Clebsch-Gordon coefficients for a $\frac{1}{2} \otimes \frac{3}{2}$ isospin system tell us that for reactions such as elastic or inelastic scattering, a $\pi^+(\pi^-)$ will be more sensitive to the proton (neutron) distribution in the nucleus than the neutron (proton) distribution. Indeed this has been the basis for the use of pions to measure neutron distributions in nuclei with pions of Δ resonance energy down to 50 MeV (for example [Roz85]). For the $(\pi, 2\pi)$ reaction where we want to measure a $\pi^+\pi^-$ pair in the final state, the sensitivity is reversed as the pair is produced through the reaction

$$\pi^+ + n \rightarrow \pi^+ + \pi^- + p.$$

A $\pi^+\pi^-$ pair cannot be produced if a π^+ interacts with a proton alone.

Some pion reactions require the direct participation of at least two nucleons in the reaction. Absorption requires two nucleons for energy and momentum conservation, while double charge exchange requires two nucleons to conserve charge. It is possible through a rapidity analysis of data to estimate the number of nucleons involved directly in the reaction, however the results can be ambiguous (for example, see [Woo84]). A concept of some use in examining many features of pion-nucleus physics is the idea of an effective number of nucleons, N_{eff} , in the nucleus able to participate in a reaction. The assumption for this is that one-body effects dominate a reaction or at least certain kinematical regions of the reaction.

Values of N_{eff} have been obtained for a variety of nuclei from backward angle quasi-elastic pion scattering [ANA*81]. At 280 MeV on ^{16}O a value of ~ 3 nucleons can be estimated. As a result of the presence of two final state pions in the $(\pi, 2\pi)$ reaction, versus only a single pion in the quasi-elastic reaction case, one might expect the value of N_{eff} to be marginally smaller than this due to additional attenuation effects in the final state.

I.1 An Introduction to $\pi - \pi$ Scattering and the $(\pi, 2\pi)$ Reaction

Pion beams are of insufficient quality to practically attempt direct methods such as $\pi - \pi$ scattering or the formation of ponium atoms to study the $\pi - \pi$ system. The experimenter must resort to studying reactions where $\pi - \pi$ vertices appear. The $N(\pi, 2\pi)$ reaction is the best available method to study the $\pi - \pi$ system to extract such quantities as scattering lengths. To examine the $(\pi, 2\pi)$ reaction here, some of the background theoretical processes will be outlined. Much of the material follows presentations in [MMS76, Sch84].

Pions participate in the electroweak interaction, as evidenced by the existence of pion decay, as well as in the strong interaction. This indicates that the Lorentz structure, quantum numbers and selection rules of the weak hadronic matrix elements should be considered in examining pion interactions. Consider the matrix element of an axial vector operator between a one pion state and the vacuum

$$\langle 0 | A_{\alpha}^i(x) | \pi(q) \rangle$$

where i is an isospin index and α a coordinate index. The axial vector operator behaves under rotation as $(0^-, 1^+)$, that is, the scalar part of the operator has a spin/parity of 0^- and the vector part has spin/parity of 1^+ . The operator can thus couple the one pion state ($J^{\pi} = 0^-$) to the ground state vacuum ($J^{\pi} = 0^+$).

The matrix element can then be non-zero and at least some part of A_α must be proportional to the pion field. The matrix element then represents a current from the vacuum state to the one pion state, that is, it is a vector itself and can be expressed in terms of the four-momentum q as

$$\langle 0 | A_\alpha^i(x) | \pi(q) \rangle = i \frac{f_\pi}{(2\pi)^{3/2}} q_\alpha e^{-iqx}.$$

For the moment, f_π is simply a proportionality constant.

The divergences of the A_α 's define pseudoscalar fields that have the same Lorentz behaviour as the pion field ϕ , and A_α^3 , $A_\alpha^{1\pm i2}$ have the same quantum numbers as the π^0 and π^\pm . Using a properly normalized pion field, one then can write, for the divergence, the PCAC guess that

$$\partial^\alpha A_\alpha^i(x) = f_\pi m_\pi^2 \phi^i(x)$$

where

$$f_\pi = 93.2 \text{ MeV}$$

is now the pion decay constant [NRDS*79] as determined from the decay width

$$\Gamma(\pi \rightarrow \mu\nu) = \frac{G^2 f_\pi^2}{4\pi} \frac{m_\mu^2}{m_\pi^2} (m_\pi^2 - m_\mu^2)^2.$$

G is the weak interaction Fermi coupling constant.

The divergence relation above defines the partial conservation of axial current (PCAC) hypothesis. In the limit of $m_\pi \rightarrow 0$ (a massless pion) or $f_\pi \rightarrow 0$ (a pion that does not decay), PCAC becomes CAC. The smallness of the pion mass on the nucleon scale says that the axial current is almost or partially conserved. What PCAC does is define a specific off-shell dependence of the matrix elements of the interpolating pion field in terms of the matrix elements of the axial current $A_\alpha^i(x)$ and says that the matrix elements of $\partial^\alpha A_\alpha^i(x)$ vary smoothly with the off-shell pions' mass. PCAC allows one to build soft-pion theories ($q^2 = 0$) and tells how to extrapolate them to the physical region ($q^2 = m_\pi^2$).

The PCAC hypothesis also allows one to relate f_π to the πNN coupling constant $g_{\pi NN}$, and the axial and vector current form factors, g_A and g_V , through the Goldberger-Treiman relation [GT58]. If we take the matrix element of the pion field between single nucleon states and use PCAC to extrapolate to the physical region, the Goldberger-Treiman relation is obtained as

$$f_\pi = \frac{m_N g_A}{g_{\pi NN} g_V}$$

where m_N is the nucleon mass and all constants on the right hand side can be experimentally determined. The relation yields $f_\pi = 87$ MeV, which is about the accuracy expected for comparisons of results obtained using the PCAC hypothesis to experimental values. Note that in some literature, f_π is defined to include an additional factor of $\sqrt{2}$.

In the SU(3) quark model, one can construct vector and axial vector currents and from these currents form chiral currents (these contain the helicity projection operator $(1 - \gamma_5)/2$). The chiral currents can be shown to satisfy a set of commutation relations forming an algebra of chiral SU(3)⊗SU(3). These relations are the basis for current algebra and are supposed to be valid even when the vector and axial vector currents are not strictly conserved. From current algebra, one can obtain values for the s-wave I=0 and I=2 $\pi - \pi$ scattering lengths, a_0^0 and a_0^2 [Wei66].

A simpler method of calculating scattering lengths and cross sections is to construct a phenomenological effective Lagrangian which satisfies the requirements of current algebra and PCAC in the soft pion limit. The form of the effective Lagrangian commonly used was introduced by Weinberg [Wei67] with the addition of a chiral symmetry breaking term by Olsson and Turner [OT69]. The symmetry breaking is parameterized by ξ which essentially measures the departure from the PCAC hypothesis.

The s-wave $\pi\pi$ interaction Lagrangian can be written, including the symmetry breaking, as

$$\mathcal{L}_{\pi\pi} = - \left(\frac{g_{\pi NN}}{m_N} \right)^2 \left(\frac{g_V}{g_A} \right)^2 \left[\phi^2 \partial_\mu \phi \partial^\mu \phi - \frac{1}{2} \left(1 - \frac{1}{2} \xi \right) m_\pi^2 \phi^4 \right].$$

This is only part of the effective Lagrangian needed to describe pion production and describes only the $\pi-\pi$ vertex in the one point pole diagram in Figure 1. The complete Weinberg Lagrangian can be written as

$$\mathcal{L}_{eff} = \mathcal{L}_o + \mathcal{L}_{\pi\pi} + \mathcal{L}_{NN\pi} + \mathcal{L}_{NN\pi\pi} + \mathcal{L}_{NN\pi\pi\pi}$$

where

$$\mathcal{L}_o = \bar{\psi}(i\gamma\partial - m_N)\psi + \frac{1}{2}\partial_\mu\phi\partial^\mu\phi - \frac{1}{2}m_\pi^2\phi^2$$

contains the nucleon and pion mass and energy terms with ψ being the nucleon field. The remaining terms describe the interaction part of the Lagrangian, that is, those that enter into a standard construction of a transition T matrix and hence the evaluation of the cross section. The interaction terms are

$$\mathcal{L}_{NN\pi} = \left(\frac{g_{\pi NN}}{2m_N} \right) \bar{\psi} \gamma_\mu \gamma_5 \vec{\tau} \psi \cdot \partial^\mu \vec{\phi}$$

which describes the pion absorption/creation vertex,

$$\mathcal{L}_{NN\pi\pi} = - \left(\frac{g_{\pi NN}}{2m_N} \right)^2 \left(\frac{g_V}{g_A} \right)^2 \bar{\psi} \left[\gamma_\mu + \frac{K_v}{i2m_N} \sigma^{\mu\nu} (p_i - p_f)_\nu \right] \vec{\tau} \psi \cdot (\vec{\phi} \times \partial^\mu \vec{\phi})$$

which describes pion nucleon scattering and

$$\mathcal{L}_{NN\pi\pi\pi} = - \left(\frac{g_{\pi NN}}{2m_N} \right)^2 \left(\frac{g_V}{g_A} \right)^2 \bar{\psi} \gamma_\mu \gamma_5 \vec{\tau} \psi \cdot (\partial^\mu \vec{\phi}) \phi^2$$

which describes the pion contact diagram of Figure 1. In $\mathcal{L}_{NN\pi\pi}$, $K_v = 1.85$ is the nucleon anomalous magnetic moment factor, $\sigma^{\mu\nu}$ is the antisymmetric tensor defined as

$$\sigma^{\mu\nu} = \frac{i}{2} (\gamma^\mu \gamma^\nu - \gamma^\nu \gamma^\mu)$$

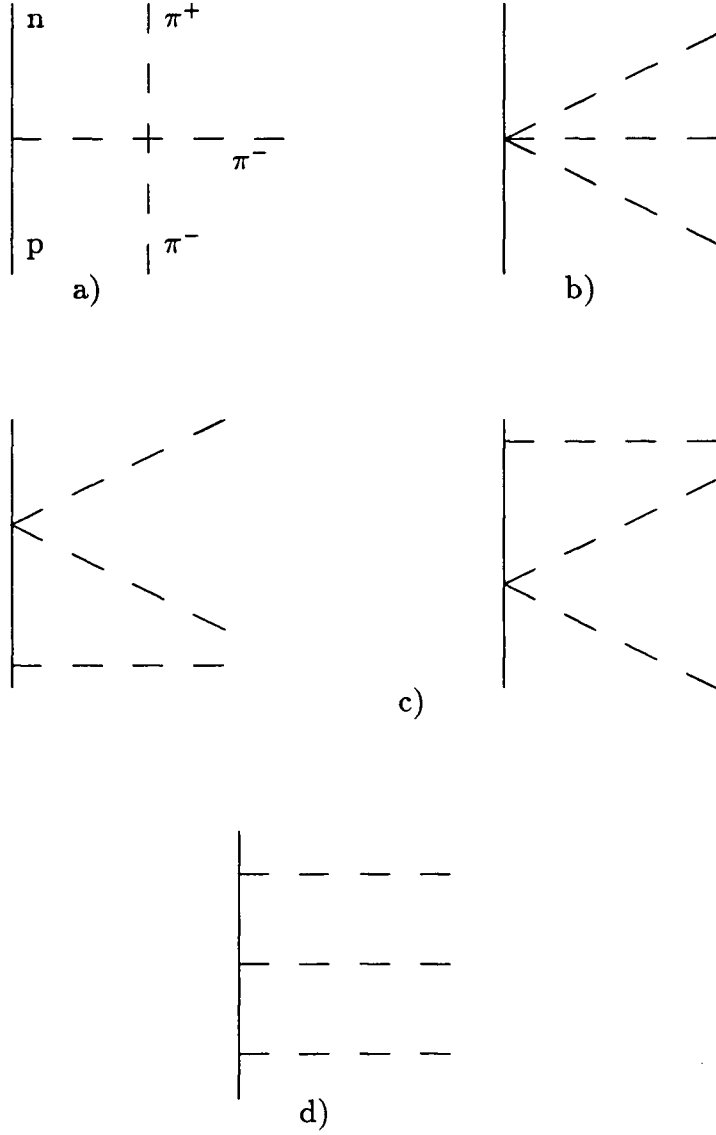


Figure 1: The a) one point pion pole, b) one point pion contact, c) two point and d) three point diagrams contributing to the phenomenological Lagrangian typically used in describing the free $(\pi, 2\pi)$ reaction.

and p_i and p_f are the initial and final nucleon momenta. τ is the nucleon isospin operator and the γ 's are the standard Dirac matrices.

The effective Lagrangian can be used to evaluate the pion production cross section and related quantities such as the scattering matrix element and scattering lengths. For the case of the reaction

$$\pi^- + p \rightarrow \pi^+ + \pi^- + n$$

it gives for the matrix element

$$\langle |M|^2 \rangle^{1/2} = (-2.475 + 1.093\xi) m_\pi^{-3}$$

and for the scattering lengths

$$a_0^0 = \left(\frac{14 - 5\xi}{16\pi} \right) m_\pi \left(\frac{g_{\pi NN}}{2m_N} \right)^2 \left(\frac{g_V}{g_A} \right)^2$$

and

$$a_0^2 = - \left(\frac{\xi + 2}{8\pi} \right) m_\pi \left(\frac{g_{\pi NN}}{2m_N} \right)^2 \left(\frac{g_V}{g_A} \right)^2.$$

The best quality measurements of the free pion production reaction on a nucleon is a recent single arm spectrometer experiment that measured the double differential cross section of the produced π^+ for incident π^- energies from 203 MeV to 357 MeV [BJK*80,Man81]. The measured cross sections for that measurement are displayed in Figure 2. The extracted matrix element was extrapolated to threshold and a comparison with the effective Lagrangian prediction gave $\xi = -0.03 \pm .26$, a result consistent with 0 in agreement with the Weinberg form. The resultant values for the scattering lengths are then

$$a_0^0 = .178 \pm .016 m_\pi^{-1} \quad a_0^2 = -.049 \pm .007 m_\pi^{-1}.$$

The isoscalar scattering length can also be obtained from the measure of the K_{e4} decay mode [REF*77] and yields results consistent with the spectrometer experiment.

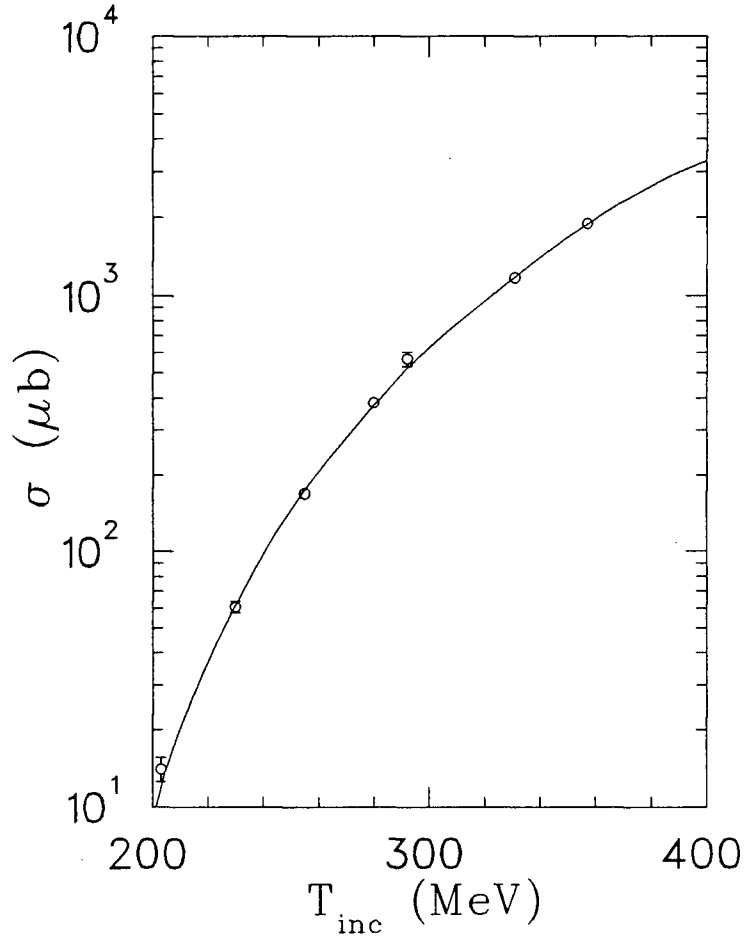


Figure 2: The energy dependence of the $p(\pi^-, \pi^+)$ reaction cross section data from [BJK*80]. The curve is a polynomial fit to the data in terms of the integrated phase-space and energy above threshold (see [BJK*80]).

The effective Lagrangian outlined above is reasonably good for describing the pion production reaction at threshold. It has several short-comings in that it does not include any effects from isobars or other intermediate states such as the Δ , the ρ or the N^* . These states can provide a substantial contribution to the production amplitude close to and even at threshold. These contributions are the focal point of the isobar analyses [Man81,ACG*79] that have been carried out on pion production data from the spectrometer experiment mentioned above as well as more kinematically complete but statistically less accurate bubble chamber data ([JAS74] and references therein). The isobar analyses determine a value of ξ consistent with zero. From fitting the data, strengths can be assigned to various intermediate state channels where the reaction has proceeded as

$$\pi^- + p \rightarrow \pi^- + \text{int. state} \rightarrow \pi^- + \pi^+ + n.$$

The states chosen typically include the Δ , ρ and ε (from N^* decay).

The spectrometer experiment measuring the $p(\pi^-, \pi^+)$ reaction was kinematically incomplete in that it did not detect the second pion in the reaction. The lowest energy coincident experiment on the proton is a bubble chamber experiment [JAS74] at 300 MeV with relatively low statistics. From Figure 2, we can see that the cross section drops very fast with decreasing incident pion energy so that at 280 MeV the cross section is approximately 370 μb , making a coincident measurement even more difficult. A coincident measurement would likely be much cleaner however, than the single arm experiment such as [BJK*80] which faced backgrounds up to 10 times the signal near threshold. In an effort to boost the measureable cross section, one can either raise the pion energy above 280 MeV, which is currently not practicable with the TRIUMF M11 facility, or one can go to a nuclear target to increase the number of scattering centers available.

Once one chooses to examine the $(\pi, 2\pi)$ reaction in a nucleus, quantities

associated with a measurement of the free $(\pi, 2\pi)$ reaction could be greatly obscured by nuclear effects. For the one-body mechanism of pion production, the presence of the other nucleons in the nucleus has many effects. They can move the production amplitude off-shell, they will distort the incident and exiting pion waves and they can alter the formation and propagation of intermediate states. Mechanisms directly involving two or more nucleons can also occur, which will add to the production amplitude. Such a mechanism, the $\Delta\Delta$ formation has been proposed as a mechanism contributing to the $A(\pi, 2\pi)$ process [BTWW82,SWB83]. The $(\pi, 2\pi)$ reaction thus offers a new way to examine the behaviour of the pion in the nuclear medium.

The $A(\pi, 2\pi)$ process has received relatively little experimental or theoretical attention in comparison to the study of the free production processes. A spectrometer experiment similar to [BJK*80] has been carried out measuring the process $d(\pi^\pm, \pi^\mp)$ [LAW*86], which is a clean signature of pion production in the deuteron as double charge exchange cannot occur. The deuteron is only loosely bound however, and the constituent nucleons can almost be considered free. Indeed, the total cross sections measured were consistent with the free cross sections and the differential cross sections agreed with a quasi-free production model based on the amplitudes obtained from analyses of the free pion production data.

The only published experimental results on a nucleus heavier than deuterium, before the experiment described in this thesis was performed, was an emulsion experiment [BBD*69] measuring the process $A(\pi^+, \pi^+\pi^-)$ with the result of $\sigma_{tot} = 300 \pm 100 \mu b$ at 270 MeV. The A is not specified in any detail. The emulsion experiment also measured the DCX reaction and from a comparison of that paper along with subsequent DCX measurements from the same group with the results of [Woo84], indicates that there is a normalization problem, the

emulsion results being at least a factor of two low. A measurement of the $(\pi, 2\pi)$ reaction on any nuclei with $A > 3$ requires a coincident measurement as a single arm experiment will measure the contributions from DCX as well as from the $(\pi, 2\pi)$ reaction. A simple estimate based upon the effective nucleon number, N_{eff} , of about 3 indicates that the cross section could be of order 1.1 mb for the reaction $^{16}O(\pi^+, \pi^+\pi^-)$ whereas simply multiplying the free $p(\pi^-, \pi^+\pi^-)$ reaction cross section by the number of neutrons gives 3.0 mb.

There have been three separate recent theoretical approaches in the literature calculating the $A(\pi, 2\pi)$ reaction. These generally start from some form of the Weinberg effective Lagrangian written in a non-relativistic form so that it can be used in the description of the nuclear process. Two-body mechanisms are not considered in any great detail, only the one-body mechanism described by the Weinberg form. There are no cross section predictions for the $\Delta\Delta$ model. It is interesting to note that the $(\pi, 2\pi)$ process can be simply connected to the DCX reaction. If a nucleon line is added to one of the outgoing pion lines in the diagrams of Figure 1, they become diagrams describing the DCX process. In discussions of the DCX process, such diagrams are called meson exchange current (MEC) diagrams. It is clear that any theoretical DCX calculation should include the contributions from these $(\pi, 2\pi)$ diagrams and their importance has indeed been demonstrated [OSVW83].

Cohen and Eisenberg [CE83] examine the $(\pi, 2\pi)$ reaction as a possible means of finding effects due to the pion condensate precursor phenomena which are characterized by the Migdal parameter, g' . They give calculations for the reactions $^{16}O(\pi^+, \pi^+\pi^-)$ and $^{16}O(\pi^+, 2\pi^+)$. The results of the $^{16}O(\pi^+, \pi^+\pi^-)$ calculation are shown in Figure 3 as x's at an incident energy of 284 MeV with g' values of .40, .55 and .70 for decreasing values of the cross section. The $^{16}O(\pi^+, 2\pi^+)$ calculation results are similar and about 20% higher. The precursor

phenomena arise from the possibility that above certain nuclear densities, the pionic modes of excitation may have an effective mass ≤ 0 so that it would be energetically favorable for pions to condense out of the medium [Mig78]. The precursor phenomena are related to the spin-isospin correlations in nuclei. It is predicted that in some reactions, near momentum transfers of $q \sim 2 - 3 m_\pi$, one might see enhancements in cross sections due to the onset of the condensate. The $(\pi, 2\pi)$ reaction in the vicinity of $T_\pi = 300$ MeV meets this condition. The precursor phenomena are currently disfavored due to the lack of observable effects in reactions such as (p, p') [HGI*80, MGB*80] or (π^+, γ) [MVEL*84] at the appropriate q .

Rockmore [Roc83] makes a simpler estimate, from the calculational point of view, of the process $^{18}\text{O}(\pi^-, 2\pi^-)$. The results he obtains are significantly different from the results of [CE83], differing by several orders of magnitude as can be seen from Figure 3 where Rockmore's results are shown as the lower solid line.

The most complete theoretical results come from Oset and Vicente-Vacas. They develop a more complex model of the elementary reaction including Lagrangian terms describing the intermediate isobars [OV85]. The model shows the importance of these isobars in accurately predicting the magnitude of the free $p(\pi^-, \pi^+ \pi^-)$ reaction. The contribution of the N^* is especially important near threshold. The content of this model is then simplified somewhat and applied to the $A(\pi, 2\pi)$ process [OV86]. Precursor effects are taken into account and shown to be small. A substantial effect is found resulting from the binding of the final state pions in the nuclear medium. Predictions for $^{16}\text{O}(\pi^+, \pi^+ \pi^-)$ are shown in Figure 3. The dashed line is the result with no binding effect or precursor effect, the middle dot-dashed line results from the inclusion of the binding effect and the upper solid line results from also including effects from precursor phenomena.

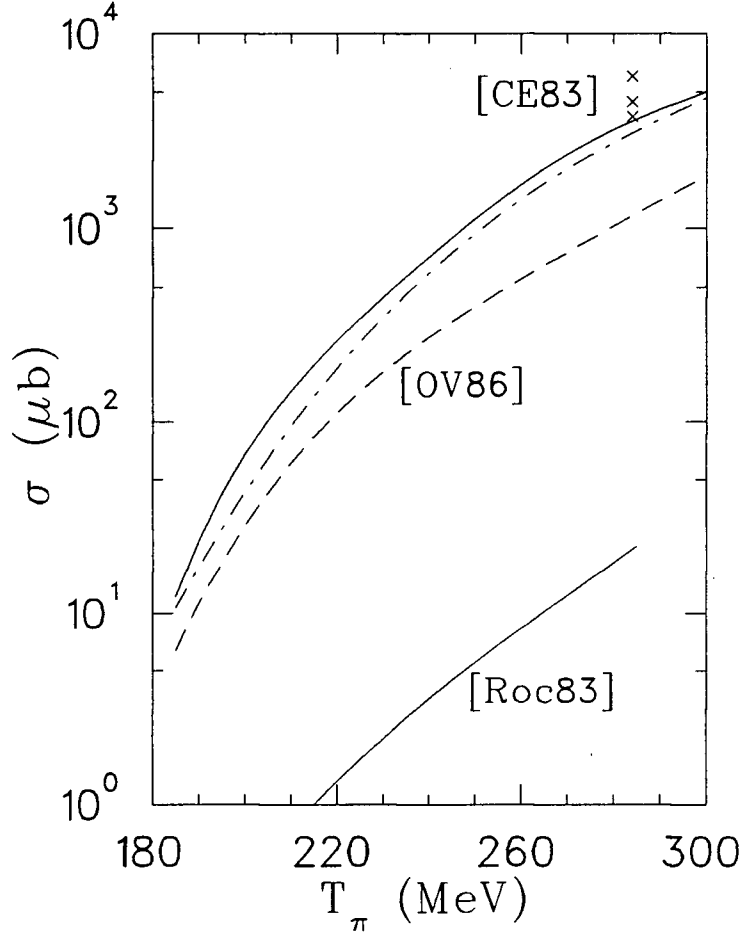


Figure 3: The energy dependence of the total cross section, σ_{tot} , as calculated by the various authors discussed in the text. Results are shown for both of the production reactions $^{16}\text{O}(\pi^+, \pi^+\pi^-)$ and $^{18}\text{O}(\pi^-, 2\pi^-)$.

Results for the reaction $^{16}\text{O}(\pi^+, 2\pi^+)$ are also given in [OV86] and are approximately a factor of 7 below the results for the $^{16}\text{O}(\pi^+, \pi^+\pi^-)$ calculation.

I.2 Summary

The $(\pi, 2\pi)$ reaction on heavier nuclei has, up to now, received little experimental attention. The work reported here provides new data that can be studied in detail and with additional results from the Oset model [OV87], the differential cross sections can be compared to the theoretical predictions. The measurement required clean identification of the outgoing π^+ and π^- to identify the reaction properly, providing information on the energy and angle of each of the two final state pions. The apparatus used to measure the reaction products will be discussed in Chapter II and shown to be well suited to the experimental needs.

The calculation of the cross sections from the data as well as the calibration work will be discussed in Chapter III. Details of the geometry and performance of the total absorption range telescope, the CARUZ, have been published [RGR88] and are discussed. Results from the data run of 1986 have been published [GRR*87]. A full scale paper containing the full results of the 280 MeV data is forthcoming.

The theoretical approaches to the $\text{A}(\pi, 2\pi)$ reaction will be discussed in more detail in Chapter IV. Some of the shortcomings present in particular models will be discussed as well as some of the superior features of the models. The methods of the Monte Carlo analysis used to study the reaction will also be presented in Chapter IV. A comparison of the theoretical and Monte Carlo results with the data will be presented in Chapter V.

This thesis concerns primarily the measurement of the $^{16}\text{O}(\pi^+, \pi^+\pi^-)$ reaction at 280 MeV and so does not yield any indication of the energy or A dependence of the reaction. Such a topic could be addressed in further work.

Chapter II

The Experiment

The experiment to measure the $^{16}\text{O}(\pi^+, \pi^+\pi^-)$ reaction at 280 MeV was carried out at the Tri-University Meson Facility – TRIUMF [Ric63]. The centre of the TRIUMF facility is the cyclotron which can provide intense beams of polarized or unpolarized protons in the energy region of 180-520 MeV. Two of the many secondary meson channels on the meson hall side of the cyclotron were used to carry out the calibration and experimental measurement work. Both view the 1AT1 production target which, for this work, was a 1 cm pyrolytic graphite target. An unpolarized 500 MeV proton beam was used for the primary beam, with typical intensities of $130\mu\text{A}$. The initial phase of the experiment was carried out in 1986, with the first CARUZ calibration work being done in February and the first data taking runs in the summer. A second run was carried out in 1987 to finish off the measurement at 280 MeV and at the same time start a measurement of the $(\pi, 2\pi)$ reaction on the deuteron (the deuteron data is not presented here).

II.1 Beamlines and Beam Monitoring

The M13 channel was used for the initial CARUZ calibration run to establish the operational characteristics of the new device. The M11 channel was used for the actual experimental data taking and QGD calibration work. The beamlines can be controlled by the experimenter through the PBX program [Sar86] which runs on the MESON μVax . To allow for the wide ranges of incident particle fluxes used for various stages of the work, several counter arrangements for counting the

incident particle beams were used allowing incident fluxes of up to $10^7 \pi s^{-1}$ to be reliably measured.

II.1.1 M13

M13 is a low energy channel capable of delivering particles with momenta in the range 20–150 MeV/c which made it well suited for supplying beams for the original CARUZ calibration. In the lower part of the momentum range, M13 functions primarily as a muon channel. At higher momenta, pion fluxes of several $10^6 s^{-1}$ can be reached. The channel is 9.4 m long, short enough to give a high flux, clean low energy pion beam at the achromatic final focus. The time-of-flight (TOF) structure of the beam makes $\pi - \mu - e$ separation easy and an in-channel CH_2 absorber removes protons and heavier particles from the beam so that any beam contamination can be easily handled. See [OWMD83] for more details.

II.1.2 M11

The M11 channel is a medium energy pion channel capable of handling particle momenta in the range 150–400 MeV/c. The configuration of the M11 channel is shown in Figure 4. The channel's dispersion is $1.8 cm / \% \Delta p / p$ at the intermediate focus and the channel is tuned to an achromatic spot at the prospective target location. The particle beam takeoff angle is 3° relative to the primary proton beam. Like M13, M11 also has a mid-plane absorber. However, at the upper end of the M11 momentum range, the absorbers cannot cause a sufficiently large momentum change to the protons to cleanly separate them from the pions (that is, for π^+) and a significant number of protons can be delivered near the target. In practice, one has to install some form of beam shield at the beamline entrance into the experimental area that blocks the protons while allowing the pions to reach the target location. These protons come from inelastic reactions of the primary

beam in the target. TOF separation of $\pi - \mu - e$ is possible for the lower channel momenta as for the M13 channel. At higher momenta, TOF separation becomes difficult but the fluxes of electrons and muons become quite small relative to the pion flux so that TOF separation is not important. Typical beam spots are 1.1 cm horizontally by 1.0 cm vertically (full width at half maximum – FWHM). See [TUH87] for more details regarding the characteristics of the channel.

II.1.3 Beam Counters

Several different counter arrangements were employed in the experiment to monitor the incident particle beam. The counter layout used in 1987 was slightly different than that used in 1986. The arrangements used in 1986 will be discussed first and then changes introduced for the 1987 run will be covered.

For QCD calibration work, an in-beam set of counters was used to count the flux. This set consisted of three plastic scintillators (NE110) which were fitted with RC8575R phototubes, called B1, B2 and B3 (collectively denoted by H_u in Figure 5). These were placed upstream of the target. The smallest counter, B1, was a 6 cm diameter circular counter and was 30 cm upstream of the target. The size and positioning of the B counters ensured that they intercepted the bulk of the incident pion beam. The fraction of beam that they missed could be estimated from REVMOC [KR83] assuming some beam spot size and divergence characteristics for the M11 channel. This estimation is further discussed in section III.1.1. The coincidence $(B1 \cdot B2 \cdot B3)$ is a reasonable measure of the incident flux when the flux is low enough so as to not saturate the bases (that is, less than 5-6 MHz). To find the true pion flux, one must account for the possible presence of multiple pions in each beam burst. Assuming a Poisson distribution for

the number of pions per burst, the correction is given by the simple form [Bar85a],

$$\frac{\mu_o}{\mu} = \frac{-\mu_o}{\ln(1 - \mu_o)} \simeq 1 - \frac{\mu_o}{2}$$

where μ_o is the observed number of pions per beam burst and μ is the true number.

As the flux used for the experimental measurement was approximately $10^7 \pi s^{-1}$, the in-beam counters discussed above would not function and so were removed from the beam at those times. However, a hodoscope placed about 2 m downstream of the target (H_d in Figure 5) remained in the beam to count the flux. It was constructed of four small (10 cm by 10 cm) counters arranged to form a square, with the beam centered on the center of the square. Each counter then intercepted approximately one-quarter of the beam and thus remained usable even at the higher fluxes. To provide an accurate measure of the beam flux, the counter was calibrated against the in-beam counters for a wide range of fluxes. This calibration is discussed further in section III.1.1. The construction of this counter also provides a convenient method of monitoring the beam position as any movement in the beam position causes a shift in the ratios (left/right) or (up/down).

A further method of measuring the incident beam was provided by the three additional counters, $\pi 1$, $\pi 2$ and $\pi 3$. These three counters were aligned so as to view the downstream side of the hodoscope, where a 6 mm thick piece of aluminum had been attached to the hodoscope. The coincidence ($\pi 1 \cdot \pi 2 \cdot \pi 3$) then measures pions which scatter from the hodoscope or attached aluminum piece towards the π counters. The coincidence rate in the π counters is then simply proportional to the incident flux, assuming no large beam position shifts occur on the hodoscope. This monitor was not extensively used as the hodoscope was found to be a reliable counter for the measurement of the pion flux.

The beam monitoring apparatus was changed somewhat for the 1987 runs to accommodate a high rate capable in-beam wire chamber [HFO*87]. This chamber, called the PCOS chamber here as it uses the PCOS III system for the readout of individual wires, has a horizontal position resolution of .7 mm (the wire spacing). It can easily handle the typical pion fluxes used in the experiment and was not removed for the high flux running. This chamber was placed approximately 15 cm upstream of the target and was required for improved particle ray tracing to help in reducing background from the target foils of the deuterium target experiment run subsequent to the oxygen experiment. With this chamber present, only the B1 and B2 upstream counters were used for calibration work, as the PCOS chamber could replace the function of B3.

II.2 Experimental Apparatus

The experimental apparatus consisted of the QQD and its associated target chamber, the CARUZ and the various beam counters discussed above in section II.1.3. The QQD was used to detect the outgoing π^- while the CARUZ detected the low energy π^+ .

II.2.1 The QQD

The QQD (quadrupole-quadrupole-dipole) spectrometer [SDB*84] has the capability of measuring pions of energies ranging from 20 MeV up to over 100 MeV in several steps. The QQD's flight path is 2.5 m to the rear scintillators, which is sufficient to provide excellent spectrometer TOF separation to discriminate against electrons traversing the QQD to greater than 170 MeV/c (corresponding to 80 MeV pions). This discrimination capability has been especially important for experiments measuring low cross section reactions, like DCX and $(\pi, 2\pi)$. The spectrometer is shown along with the CARUZ and the various beam counters in

Figure 5. The two quadrupoles serve to increase the spectrometer solid angle to $\sim 16 \text{ msr}$ and the dipole bends the pions 70 degrees horizontally to the left. The QQD has a large momentum acceptance, approximately $\pm 20\%$. The solid angle is nearly constant over about one-half the momentum acceptance range. The focal plane of the spectrometer is beyond the last wire chamber and is tilted at 72 degrees with respect to the central ray of the spectrometer when both quadrupoles are in operation. The first quadrupole, QT1, was not used for this experiment as a short circuit existed in its power coils, preventing their energization. QT1 has only a small effect on the solid angle ($\sim 5 - 10\%$ increase), as most of the solid angle increase results from the vertical focussing in QT2. The absence of QT1 thus has little effect on the experimental counting rate but does move the spectrometer focal plane upstream of the wire chambers.

The detection equipment for the QQD consists of four Multi Wire Proportional Counters, MWPC's or wire chambers, and three plastic scintillators (NE110) placed after the last two wire chambers. The scintillators, E1, E2, and E3, are large enough to cover the wire chambers and are 6.4 mm, 6.4 mm and 12.7 mm thick respectively. E1 and E2 have a phototube on each end of the scintillator while E3 has two on each end. An additional scintillator was used for the 1987 runs which is not shown in Figure 5. This was a scintillator of dimensions 40 cm by 10 cm by 6 mm which was placed inside the QQD vacuum tank between the pole faces. This counter was used to aid in reducing background arising primarily from $\pi - p$ elastic and quasi-elastic scattering as discussed in section III.1.2.3.

The wire chambers monitor the trajectory of the pions as they travel through the QQD. Two of the chambers are placed before the QQD dipole at the WC1 and WC3 positions and two after the dipole at WC4 and WC5 locations. The two

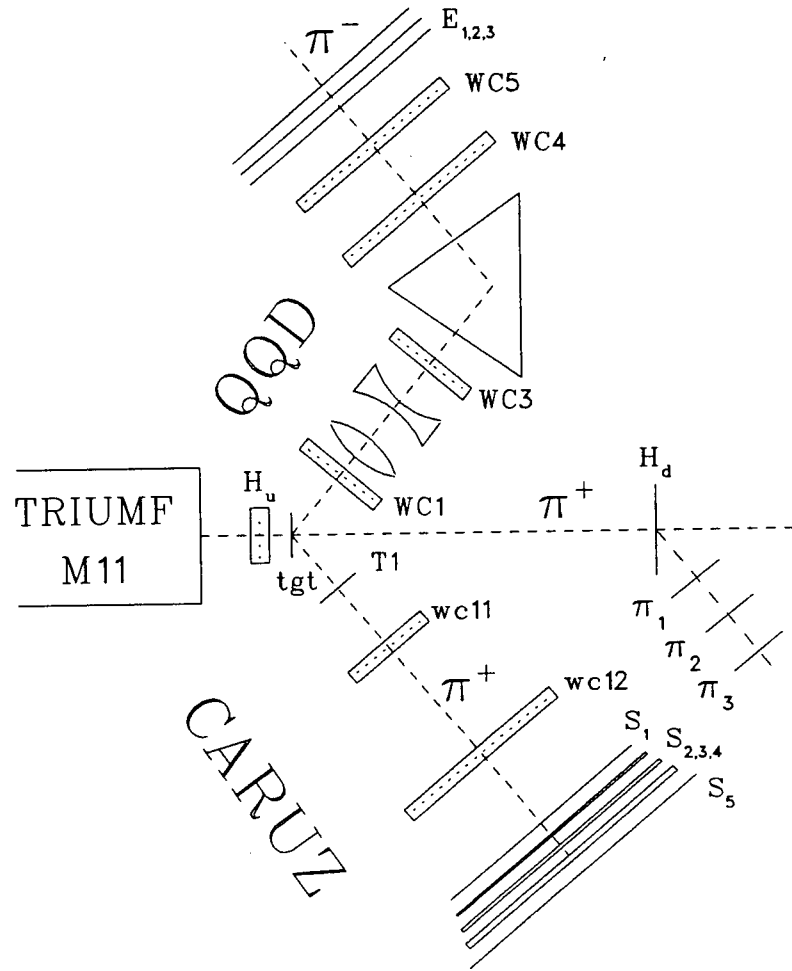


Figure 5: Showing the QCD, the CARUZ and the various beam monitors.

back end chambers use an argon-isobutane gas mixture while the front chambers use a helium-isobutane mixture to reduce multiple scattering. Only three chamber positions are, in principle, required to reconstruct the pion momentum. Having four position coordinates allows a check of the consistency of the calculated momenta to help eliminate muons resulting from in-flight pion decay in the QQD. The coordinate directions are defined such that z is along the flight direction of the detected particle and y is vertical, thus x is positive towards the particle's left.

The wire chambers are constructed with three parallel planes of wires. The middle plane is the anode plane which is supplied with a positive high voltage, while the outer two cathode planes are grounded. The cathode plane supplying the y -direction information has its wires oriented horizontally, parallel to the anode plane wires. The remaining cathode plane supplies the x -direction information and has its wires oriented vertically. The cathode wires are connected to printed circuit delay lines and the signals from each end of the delay line are timed in time-to-digital convertors (TDC's). The anode wires provide a fast logic pulse which can be used in the electronic logic (see section II.3.2).

The position of the particle track through a wire chamber is related to the difference of the times of the minus and plus sides of the delay lines simply by

$$X_i = m_i \cdot (tdc_{i-} - tdc_{i+}) + b_i$$

where X , m , and b are respectively the position, the conversion factor for time to position and the offset for the i^{th} position coordinate. The sum of the TDC values for the left and right delay line ends should give a constant value (leaving out the ionization drift time) related to the length of the delay line. Thus, a sum value in the proper sum range indicates a valid wire chamber signal. The construction of the wire chambers, along with a few assumptions, provides the information needed to determine fully the conversion factors and offsets. When a particle passes

through the chamber, it leaves an ionization path. The freed electrons drift towards the anode plane and avalanche around an anode wire creating a large pulse on that wire. This pulse induces pulses in the nearby cathode wires. As mentioned above, the y-plane wires are parallel to the anode wires. Thus, the y-plane cathode wire nearest the anode wire where the avalanche took place will have the largest induced pulse and will determine the position in the y-direction resulting in a discrete set of observable y positions corresponding to the parallel anode wires. As the anodes are 2 mm apart, one can then readily find the proper conversion factor.

The x-plane does not see discrete avalanche locations and so does not provide the conversion factor so easily. For WC1 and WC3, the x delay line is identical to the y line, so one can assume that the x and y slopes are equal. The back wire chambers have the x delay lines split into three pieces, with each segment containing 203 wires spaced 1 mm apart. Particles that pass between segments or very close to the segment edges can fire both segments. By looking at instances of double firings and requiring the position of these firings to correspond to the segment edges, one obtains the conversion factor as well as the offset. The left and right segments are assumed to have the same conversion factors as the middle segment as the delay lines are the same. The offsets for the y coordinates, as well as the x in WC1 and WC3, are obtained by centering the obtained position distributions for the relevant coordinate.

II.2.2 The CARUZ

The detector used in coincidence with the QQD had several constraints on its design and construction. It was intended for the detection of π^+ 's without concern for detection of π^- 's, as two π^- can not be produced in a single pion production reaction with an incident π^+ . Thus a detector that stops the particle could be

employed without the problem of nuclear star formation that stopping π^- produce. The detector needed to have as large a solid angle as was reasonably possible and be able to operate close to the target. A clean mass-separation between electrons, pions and protons was required so good timing resolution and moderate energy resolution were desirable.

To meet these needs in an inexpensive device, the CARUZ telescope was designed and built. It has a large solid angle (190 msr), moderate energy resolution for particles stopping in the device and good timing resolution so that it can function well in coincidence.

The CARUZ consists of two wire chambers using an argon-isobutane gas mixture and six NE102A plastic scintillators (the first scintillator is actually made of Bicron BC 412, a NE102A equivalent) as shown in Figure 6. The components are supported by a heavy duty angle iron frame which sits on the same track that supports the QQD. The geometry of the components of the CARUZ is given in Table I. The MWPC's have delay line readouts on the grounded cathode planes and a fast logical output from the anode planes for use in event logic if this is desirable. WC12 is in fact a backup rear wire chamber for the QQD. WC11 is a standard TRIUMF chamber with etched strips on an aluminized mylar foil, instead of wires, acting as the cathode plane. The wire chambers are calibrated in the same manner as those chambers in the QQD. The MWPC's can trace particle trajectories backwards to the target location and forwards to the scintillator stack. The MWPC's have typical intrinsic position resolutions of approximately 1 mm.

The tracing abilities of the MWPC's make it possible to detect or "tag" some of the inflight decays of the pions into muons. Most of the decay muons still stop in the CARUZ due to its large size. From the experimental point of view, it is not required to discriminate against these decay muons as they result from the

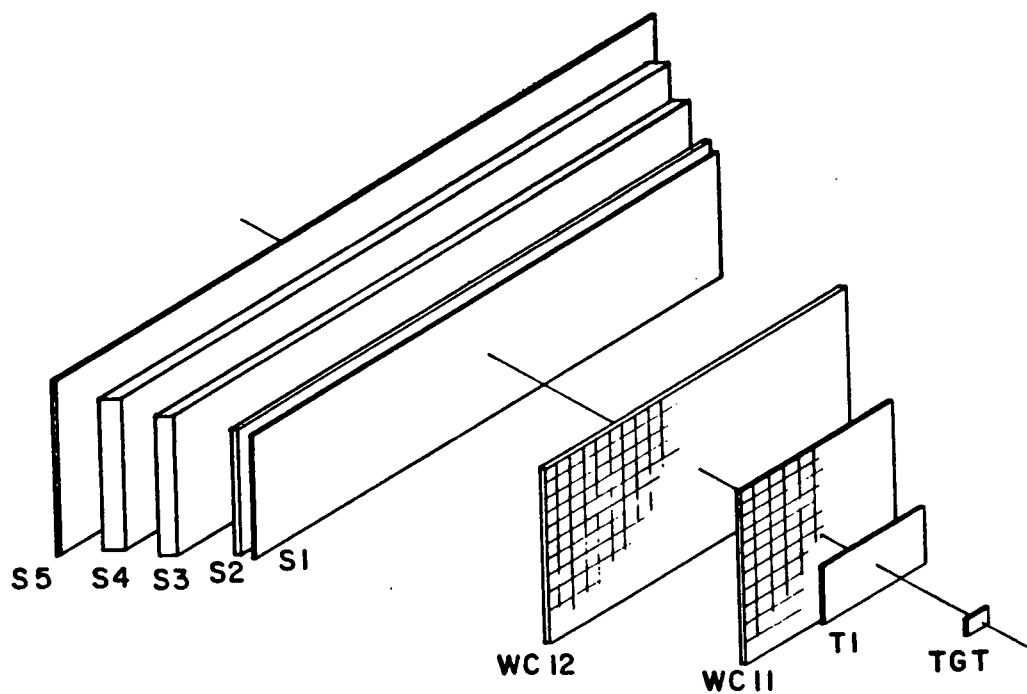


Figure 6: A close view of the CARUZ showing the relative sizes and positions of the components.

Detector	Dimensions $x \times y(\times z)$ (cm^2 or cm^3)	Distance from target to component center (cm)
T1	$20. \times 10. \times 0.08$	20.0
WC11	$30. \times 30.$	31.1
WC12	$60. \times 30.$	54.6
S1	$93. \times 21.5 \times 0.7$	96.9
S2	$95. \times 22. \times 1.3$	99.3
S3	$104. \times 24. \times 3.5$	108.1
S4	$110. \times 26. \times 4.2$	115.5
S5	$120. \times 30. \times 0.5$	122.0

Table I: Table of the dimensions of the CARUZ components and their distances to the scattering target location.

$(\pi, 2\pi)$ reaction. However, the muons may deposit an energy different from the original pion energy, distorting the obtained energy distribution from the actual pion energy distribution.

The first scintillator, T1, is a thin, small area counter read by two Phillips XP2230 phototubes which take off from the scintillator in the vertical direction. This allows the CARUZ to be placed close to an experimental scattering target without obstructing the in-plane space for other detectors or for the incident beam. T1 provides the start for the particle TOF measurement in the CARUZ. The T1 phototubes are suitable for high rate applications. The photomultiplier bases are units designed and built by INFN, Trieste, that have two high voltages supplied, one being the normal scintillator voltage with the second supplying an injection point in the base to prevent signal sagging at high rates. T1 was made thin to reduce effects of multiple coulomb scattering near the target location which would impair the position resolution. A thick T1 counter would also raise the energy detection threshold of the CARUZ as a T1-S1 coincidence is required

for the event definition (see section II.3.3). However, the detector thinness makes the counter not very useful as a good ΔE counter as its output signal height is roughly equal to its output signal resolution.

The main scintillator stack consists of five scintillators (S1 to S5) of total thickness 10.2 cm. S1, S2 and S5 have a phototube-photomultiplier unit on each end of the scintillator while S3 and S4 have two units on each end to facilitate the light collection. The phototubes used were EMI 9815B and the bases were INFN versions with one high voltage supply. The tubes were gain matched in pairs or fours so that the tubes on each scintillator all had approximately the same intrinsic gain. The first scintillator in the stack, S1, provides the TOF stop defined by the mean time of the left and right signals, as well as a ΔE measure for those particles which pass through it. The flight path distance used for TOF determination is 76.8 cm, the distance between T1 and S1. The timing information from S1 also provides a horizontal position measurement through the time difference of the right and mean time signals. This information is useful when the MWPC's are inefficient. For this analysis, the S1 position information was used in place of the wire chamber information.

The counters S1 to S4 measure the energy and the range of the particle (ie. the number of slabs firing). S5 serves as a veto counter to reject particles passing through the stack. The stack scintillators are approximately 1.0 m horizontally by 20 cm vertically, with the dimensions increasing slightly into the stack to keep the device solid angle constant and to reduce effects of multiple scattering losses. The varying scintillator thicknesses serve to have approximately equal pion energy intervals stopping in each slab and the small number of slabs reduces detector complexity while still providing a good ranging capability. The S1 scintillator originally was made to be 95 cm by 26 cm, somewhat larger than the dimensions given in Table I. This was done with the intent of reducing multiple scattering

losses. However, as S1 then subtends a larger solid angle than S2, difficulties are encountered in particle identification when the particles pass through the edge regions of S1. S1 was modified to the present dimensions for the 1987 runs. Although the particle discrimination is performed primarily by a TOF-E- ΔE method (see section III.1.3.2), the ranging capability was desired at the device design stage to clarify the particle discrimination.

The small material thickness in front of the stack gives the detector a low particle energy detection threshold. Pions of 8 MeV at the target location and protons of 16 MeV can be detected by the CARUZ. The S5 veto limits the discrimination to about 60 MeV for pions and to 140 MeV for protons. The stopping thickness of material available to the particle varies with the angle of the particle from the central trajectory in the stack. Thus the upper energy limit depends upon the trajectory through the CARUZ. The energy range accessible for particles that can be stopped in the device could easily be extended by adding another slab to the CARUZ stack. However, the rapid increase in particle range and reaction losses with energy soon makes further expansion of such a device impractical.

II.2.3 Targets

The $(\pi, 2\pi)$ reaction measurement was done using a gelled liquid H_2O target of areal density 611 mg/cm^2 . The frame consists of a piece of perspex with an oval hole in it as shown in Figure 7. The gelled water is kept in place in the target by a kapton window of $50 \text{ }\mu\text{m}$ thickness and is additionally coated with a thin aluminum foil layer of thickness $12 \text{ }\mu\text{m}$ to reduce evaporation losses. The windows are of negligible thickness in comparison to the water in the target, having a total areal density of 17 mg/cm^2 . However, the target frame material could be a substantial background source if the incident beam strikes the frame instead of the

Target	Nucleus	Areal Mass Density (mg/cm^2)	N_{tgt} (cm^{-2})
H_2O	^{16}O	543	$2.04 \cdot 10^{22}$
	1H	68	$4.08 \cdot 10^{22}$
^{12}C	^{12}C	124	$6.22 \cdot 10^{21}$
		378	$1.90 \cdot 10^{22}$

Table II: A table of various targets employed in the $(\pi, 2\pi)$ experiment indicating their thicknesses.

water. An empty target, constructed identically to the water target, including the foils, is then used to look for such background effects.

The calibration work done on the QQD requires the use of several other targets besides the water target. For QQD target traceback checks, two strip targets made of 3 mm wide nichrome strips are used. One has the strips oriented horizontally and one vertically. For the solid angle acceptance scan measurements on the QQD (see section III.1.2.2), two targets were used, a thin ^{12}C and a thick ^{12}C . These had areal densities of $124 \text{ } mg/cm^2$ and $378 \text{ } mg/cm^2$ respectively. The target thicknesses are tabulated in Table II.

II.3 Data Acquisition and Electronics

The $(\pi, 2\pi)$ experiment was somewhat more complex from the experimental point of view than most previous experiments for which the QQD has been used. The presence of a second arm, the CARUZ, increases the amount of electronics required to define events and increases the amount of online calculations that the data acquisition system must handle. The electronics for the experiment can be examined in three parts, that relating specifically to the QQD detectors, that

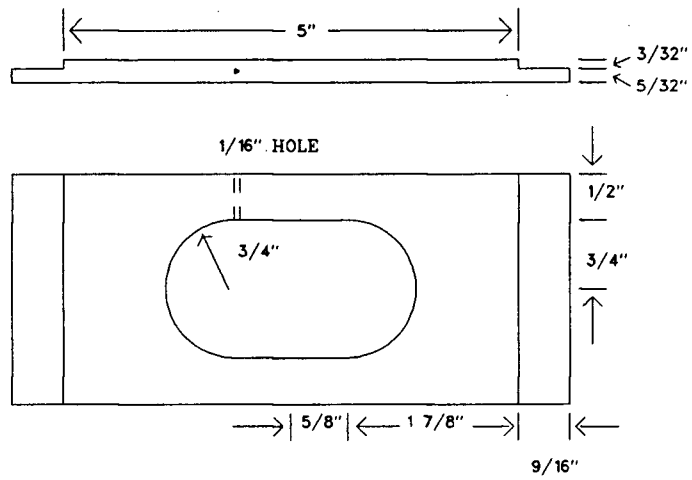


Figure 7: A scale drawing of the gelled water target used for the $(\pi, 2\pi)$ measurement.

relating to the CARUZ detectors, and those components which join the two arms into the overall event logic, handle the computer related functions such as the busy circuitry and reset signals and take care of the beam monitoring.

II.3.1 Data Acquisition

The data acquisition system must be versatile enough to handle the calculation needs of the experiment, but not overreach the limited memory abilities of the computers currently available for data acquisition in the experimental halls. A modified form of the STAR [Smi87] data acquisition system, run on a PDP-11/34 computer using the RSX operating system, was used to collect the QQD and CARUZ data from the CAMAC crates. The STAR system also took care of the online analysis.

The acquisition system responds to LAM's (look-at-me's) generated by feeding the event coincidence (see section II.3.4) into the strobe input of the C212 unit. The system then reads the required CAMAC units to obtain data in the form of TDC, ADC (Analog-to-Digital Converter), scaler and C212 bit pattern values and writes this data to tape if it has acquired a full buffer of events. Any online analysis is then performed before the system will accept a new event.

The STAR system has many advantages over the older MULTI system used before. The online analysis is written in FORTRAN with which most scientists are familiar and so it is easily adaptable to various experiments. Histograms of the data and the effects of cuts to the data can be readily investigated. The STAR system can handle information coming from more than one CAMAC crate. A J11 preprocessor can be employed to reduce the amount of recorded data by reducing the amount of background triggers passed to the main acquisition system. The online software can be used, with some modifications, for offline analysis.

However, the system does not inhibit scalers while an event is being analyzed, so a

dead-time correction must be applied in calculating cross sections. System dead-time is not a problem for this experimental measurement of the $(\pi, 2\pi)$ reaction, where event rates were at most, a few per second.

II.3.2 QQD Electronics

The signals from the QQD detectors consist of eight phototube pulses, four anode pulses and 24 cathode delay line pulses, all of which are timed with respect to the B1 counter during calibration work. The electronics associated with the QQD detectors is shown in Figure 8. The scintillator signals are fanned out through a linear fan-out (model LRS 428A) with one output going to CAMAC ADC's (model LRS 2249A). A second output of the fan-out goes to a constant fraction timing discriminator (CFTD, model Ortec 934) to reduce the timing uncertainty effects associated with pulses of varying heights. The CFTD's supply inputs to TDC's (model LRS 2248A) to provide timing information on the pulses from each side of E1 and E2. E3 timing information is not recorded as having E2 information in addition to E1 provides enough redundancy. The left and right scintillator signals are mean timed (MT, model LRS 624) to produce position independent timing of the scintillator signals. A spectrometer event, SPECT, is then defined by the coincidence $E1 \cdot E2 \cdot E3$ in an model LRS 622 coincidence unit. The signal of the internal scintillator, $B2'$, used in the 1987 run, was discriminated and fed to the C212 unit for use in the software.

The delay line signals from the cathode planes are discriminated (D, model LRS 821Z) and then sent to TDC's. The anode planes provide a fast logic pulse that helps in further refining the definition of a spectrometer event. The anode signals are discriminated to improve the pulse shape and the coincidence $(W1A + W3A) \cdot (W4A + W5A)$ is formed. This coincidence insures that at least one of the front QQD wire chambers and at least one of the rear wire chambers

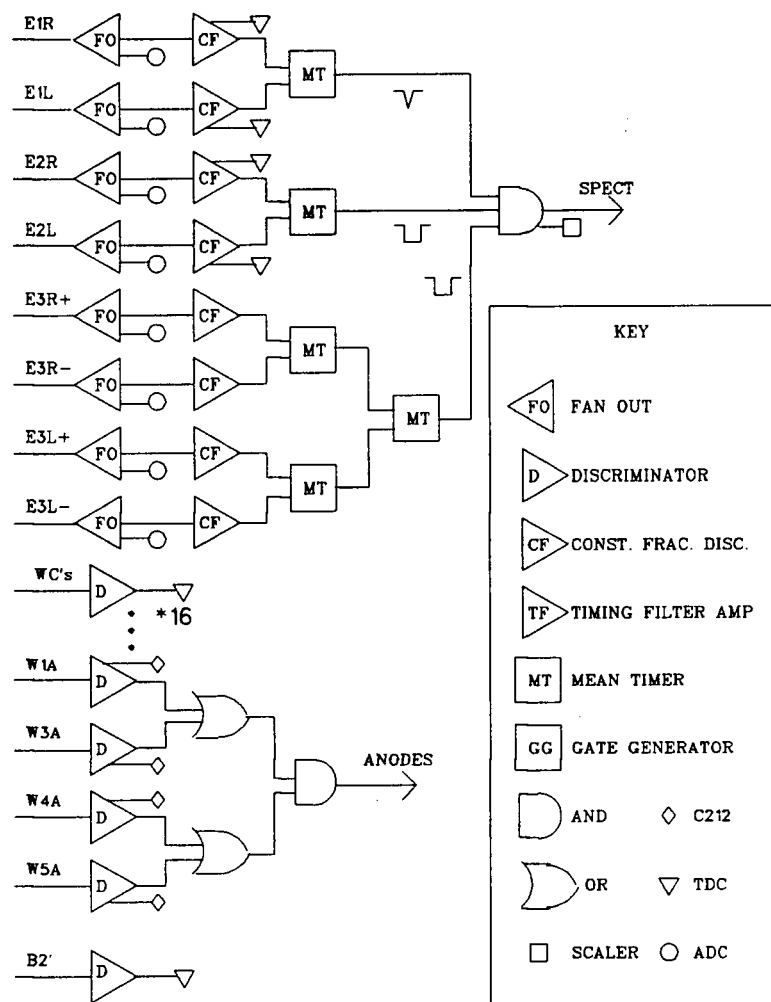


Figure 8: A diagram of the QQD related electronics. The key in the figure defines the symbols used for the CAMAC and NIM components.

fired. The discriminated signals are also fed into the C212 unit to be recorded in the bit pattern. The anodes are very efficient in comparison to the cathode plane, providing a signal better than 99% of the time when a valid cathode signal is present. It is also possible to get TDC values for the anodes. These could be used to improve the delay line sum spectra by removing the ionization drift time and could be used to improve the resolution of the chambers in the y-direction. Unfortunately, these TDC values were not recorded in the data.

II.3.3 CARUZ Electronics

The electronics configuration used for the CARUZ detector components is shown in Figure 9. The signals from T1 and S1 are first passively divided to provide outputs to ADC's (model LRS 2249W) as well as to the timing logic. The T1 pulses are sent into CFTD's (model Ortec 473A) to reduce the timing uncertainty effects. The CFTD outputs are then sent into a mean timer to give timing independent of the particle position in the scintillator. The MT output provides the common TDC starts when in coincidence with the LAM (see section II.3.4) as well as a signal for use in the T1-S1 coincidence which defines an event in the CARUZ. To guarantee a coincidence between the CARUZ and the QQD, all the CARUZ electronics timing is set relative to the timing of the B1 counter during the calibration work.

The large size of the S1 scintillator causes distortions in the light pulse shape (due to dispersion in the scintillator). To compensate for this effect so that the signals are useful for timing applications, the photomultiplier signals are sent through a timing filter amplifier (TFA, model Ortec 474). This standardizes the pulse shapes to a pulse with a constant risetime. T1 does not require this shaping due to its small size. The pulses are then sent through CFTD's and into a MT. One of the mean timer outputs as well as an output from one of the S1 CFTD's

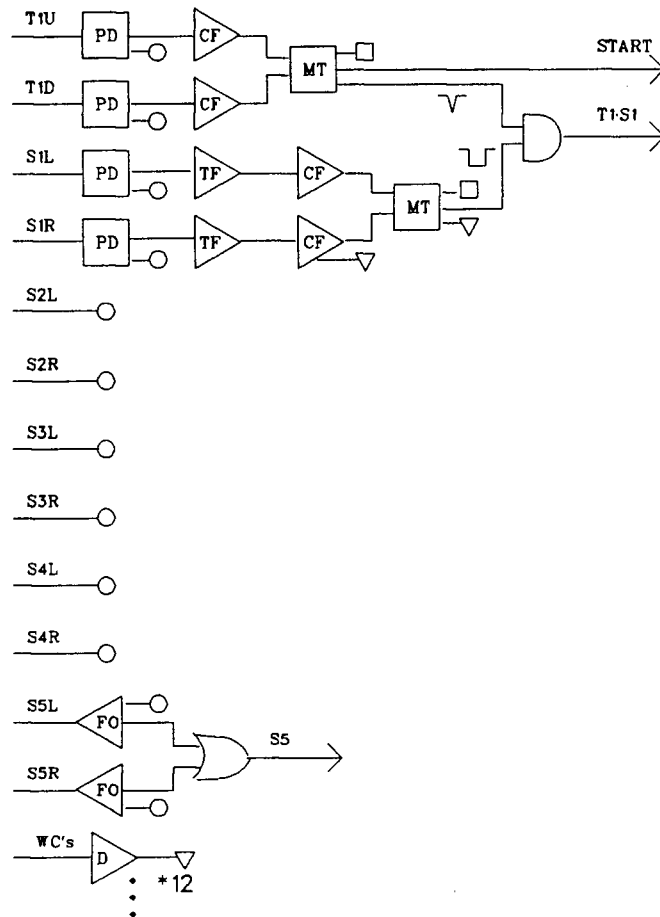


Figure 9: The electronics used for the CARUZ section of the apparatus. The key is the same as for Figure 8. PD denotes a passive divider.

(the right side signal was used here) are fed into TDC's. An S1 MT output goes to a coincidence unit with the T1 output to provide the CARUZ event definition.

As mentioned earlier, S3 and S4 have two photomultipliers on each end of the scintillator. These two signals are passively mixed so that S3 and S4 may then be treated the same as the other scintillators. Signals from each side of the six scintillators are sent to ADC units. As S5 functions primarily as a veto counter, it has some associated electronics to accomplish this. The left and right S5 signals are fanned together and then discriminated to provide a logic pulse. This pulse can be used as a hardware veto on T1·S1 or just as a software veto. To use as a software veto, the discriminated S5 signal is fed to the C212 unit. The MWPC information is obtained by discriminating the pulses obtained from each end of the delay lines and then feeding them to TDC's.

II.3.4 Computer Event Logic and Beam Electronics

The basics of the electronics for the individual arms have been given above. Signals from each arm must be then joined together to form the event definition and logic must be present to handle the computer's response to supplied events as shown in Figure 10. An EVENT is defined by the coincidence

$$\text{CARUZ} \cdot \text{SPECT} \cdot \text{Anodes} \cdot (B1 \cdot B2 \cdot B3)$$

where $B1 \cdot B2 \cdot B3$ is only included for the calibration runs to define a beam particle. The beam coincidence also defines the BEAM SAMPLEs which are used to monitor the beam composition at low channel energies. A gate generator is set to open a gate once a second in coincidence with the beam which generates a SAMPLE event.

A logical OR of the EVENT and SAMPLE then defines the LAM coincidence in conjunction with the computer \overline{BUSY} and the computer "Run in

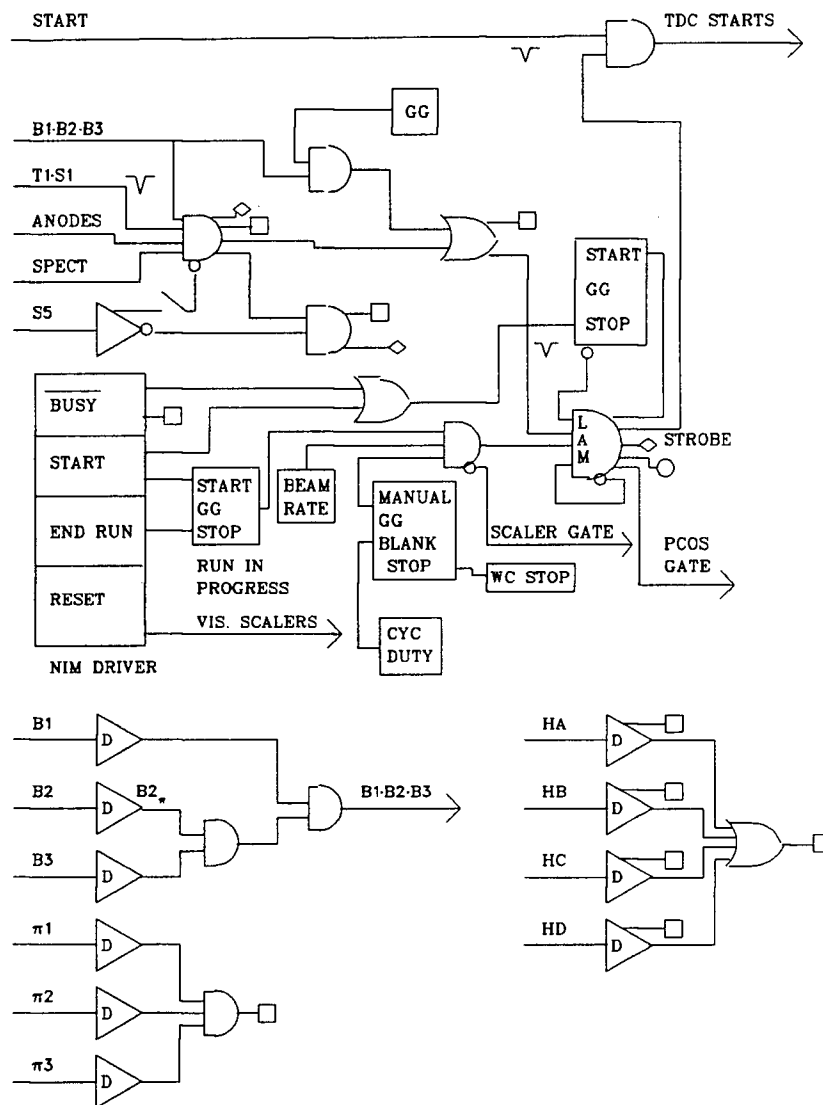


Figure 10: Showing the final LAM definition, computer related electronics, and electronics for the beam monitoring. The key is the same as for Figure 8. Delays are not shown.

Progress" signal. The LAM coincidence starts the BUSY GG which then inhibits further LAMs. The \overline{NIM} output of the LAM is fed to the LAM input to insure that the LAM is disabled until the BUSY signal arrives. The computer provides an output through the NIM driver which starts or stops the "Run in Progress" GG when a run is begun or ended. This GG output, in coincidence with the manual start/stop GG and the beam rate level monitor provides the "Run in Progress" signal to the LAM. The beam rate level is given by the output of a rate meter monitoring the flux in the hodoscope. A level detector monitoring the cyclotron duty factor supplies a signal into the blanking input of the manual start/stop to inhibit data taking when the cyclotron duty factor is too low. The wire chambers supply a high voltage trip monitor signal which stops the manual start/stop GG and thus the data acquisition when a wire chamber trips off. This insures that data is not taken when a wire chamber is not working.

The LAM is used to gate all the ADC's and is used to strobe the C212 unit, making the computer aware of the event. The TDC's are started by a coincidence between the LAM and a time definition counter which is T1 for the experimental data and CARUZ calibration data, but is the $B1 \cdot B2 \cdot B3$ coincidence for the QQD calibration data. Defining the TDC start in this manner forces the timing to always be defined by the same counter, removing the possibility that any coincidence timing uncertainties earlier in the event or LAM structure affect the TDC results. The LAM also provides a gate signal to prompt a readout of the PCOS system for the in-beam chamber used in the 1987 runs.

The hodoscope supplies four signals which are discriminated. The outputs are counted in scalers individually and fanned together for a total count rate. The computer periodically reads the CAMAC scalers and calculates the hodoscope ratios of (up/down) and (left/right). The ratio results are then output through a CAMAC digital-to-analog converter (DAC) which may be read by a multimeter.

For purposes of the hodoscope calibration, the B2 signal is discriminated with a high level threshold to select the protons in the beam. This high level B2 signal is then used to veto the $B2 \cdot B3$ coincidence to provide the quantity $(B2 \cdot B3)_\pi$ which in coincidence with B1 gives also $(B1 \cdot B2 \cdot B3)_\pi$. Lastly, the discriminated signals from the counters $\pi1$, $\pi2$ and $\pi3$ form a coincidence to monitor the scattered particles from the hodoscope and is counted in a scaler.

Chapter III

Data Reduction

The raw experimental data obtained from the experiment must be converted to the desired results of cross sections. This requires that all the apparatus has been calibrated in some form to give units such as degrees, MeV, etc. and that the collected data be analyzed using the obtained calibrations. Data were taken for the purpose of calibrating the apparatus to obtain such units. The calibration data also allows one to determine efficient cuts to apply to the data to obtain clean spectra. Much of the reduction work relating to the QQD calibration has been described before, for example in [Roz85], so some details that have been omitted may be found there. The CARUZ calibration work was described in [RGR88] and this is contained below with some additional comments.

The offline analysis made use of the histogramming analysis package MOLLI [BK85] for most of the work. MOLLI was used as much of the offline analysis program was written before realizing STAR had to be used for the online work. This necessitated the conversion of the data tapes from the format written by STAR to one expected by MOLLI. This was not a major problem considering there were about a dozen tapes in all.

III.1 Calibration

This section describes the calibration work required to analyze the $(\pi, 2\pi)$ data. The optimization of the QQD spectrometer coefficients to calculate the QQD pion energy and the definitions of the cuts applied to the QQD spectra are discussed.

The mass-separation of pions from protons and electrons in the CARUZ and the determination of the pion energy is also described. Also discussed is the calibration of the hodoscope at 280 MeV to determine the incident beam flux for the $(\pi, 2\pi)$ data. For the low channel energy settings used for QQD and CARUZ calibration work, the pion content of the beam is determined from the fraction of pions in the beam as given by the channel TOF spectra of the beam sample events. A typical TOF spectrum for low energy pions is shown in Figure 11 which shows the clear $\pi : \mu : e$ separation possible. The double peaked structure of the TOF results from the structure of the primary proton beam which contains two closely spaced proton bunches in each beam burst. As the channel energy is increased, the electron and muon peaks merge into the pion tail. However, since the fraction of electrons and muons in the beam drops with increasing energy, becoming almost negligible at 280 MeV, the contamination can be ignored at 280 MeV.

III.1.1 Beam Monitor Calibrations

An accurate measure of the beam flux is required to obtain absolute cross sections. For the QQD calibration runs, the flux is defined by the coincidence $B1 \cdot B2 \cdot B3$. Proton contamination is not present in the beam for the low energy used for the QQD calibration work. The actual experimental runs did not have the B counters present so that the hodoscope must be used to provide the measure of the beam flux. The measured hodoscope flux as a function of the horizontal jaw setting in the channel is shown in Figure 12. The hodoscope does not see the entire pion beam, only about one-half of it. The hodoscope can be calibrated against the in-beam B counters for a range of jaw settings as long as the B counters do not saturate. The calibration was carried out twice, with the CARUZ at -50° and at -100° , as the hodoscope could see more of the beam when the CARUZ was at

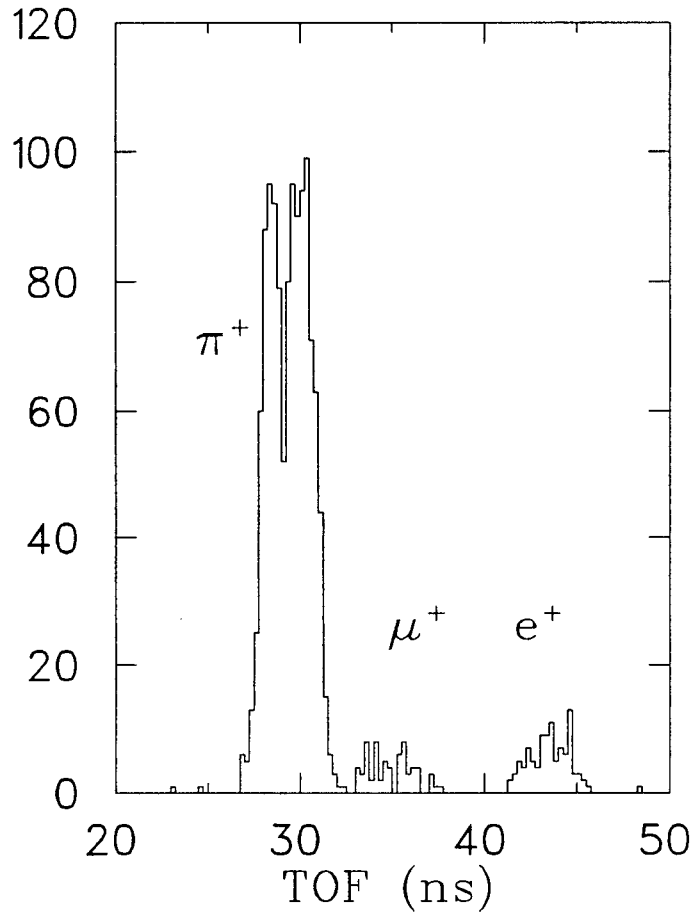


Figure 11: A typical M11 TOF spectra at incident pion kinetic energy of 84 MeV used to separate pions from electrons and muons in the incident beam at low channel energies.

-100° than at -50° due to some of the beam hitting the CARUZ elements.

The obtained low flux behaviour of the calibration data is then scaled to the fully open horizontal jaw condition used in the experiment. The pion flux is obtained from the hodoscope reading by the ratio

$$c_\pi = \frac{\pi - flux}{HODO} = \frac{(B1 \cdot B2 \cdot B3)_\pi}{HODO_{B-IN}} \cdot \frac{HODO_{B-IN}}{HODO_{B-OUT}} \cdot \frac{1}{B_{eff} \cdot TGT}.$$

The two different subscripts on HODO denote the measurement of the hodoscope rate at a common proton beam current with the B counters present or IN and with them not present or OUT to account for reaction and multiple scattering losses of the flux in the counters. The third term gives the total efficiency of detecting pions in the B counters and within the selected target cuts. This term was determined by a REVMOC simulation to be 0.89. The measured beamspot for $(\pi, 2\pi)$ events and beam divergences from [TUH87] are taken to describe the beam and are used as input to the calculation. The B2 proton veto is used to give $(B1 \cdot B2 \cdot B3)_\pi$ for the calibration as one desires the pion flux at the target, not the combined pion and proton flux. The net result of the calibration gives the conversion from the hodoscope to pion flux in the defined active region of the target to be 1.674 when the CARUZ is at -100° and to be 1.898 for the CARUZ at -50° . The error in this determination, arising from the uncertainty involved in extrapolating low flux behaviour, is estimated to be 5%.

The use of the PCOS chamber in the 1987 runs makes the beam flux measurement much easier. The flux reading given by the OR of all the wires needs simply to be corrected for multiple hits and inefficiency. The efficiency can be obtained by checking the coincidence of the PCOS OR with the B counters and is found to be 0.92. This flux determination does not have the target cut fraction built in and so this cut must be separately accounted for. The beam lost in the target cut can be obtained by examining the PCOS chamber position for sample

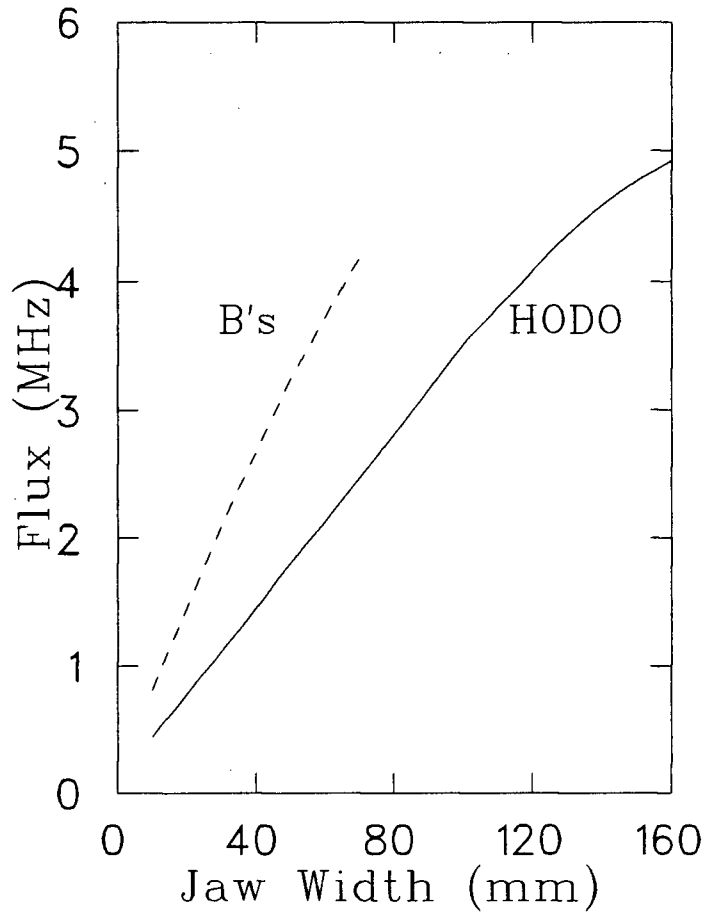


Figure 12: The measured hodoscope and in-beam counter flux corrected for multiple pions per beam burst versus the width of the horizontal jaw in the channel. The shape follows that of the expected flux for the channel settings as given in [TUH87].

events and for events where a valid coincidence in the two arms has occurred (including the target traceback cut). The sample spectrum gives the true beam shape, while the spectrum cut on valid events gives the accepted beam shape. Normalizing the two spectra to the same maximum and taking the ratios of the areas gives the fraction of beam accepted in the target cuts. Since the PCOS chamber counts the full beam directly, the only uncertainty in the flux on the target comes from the uncertainty in the chamber efficiency and the uncertainty of the beam fraction on target. The error in the flux determined by the PCOS chamber is estimated to be 2%.

III.1.2 QQD Calibration

To extract useful information from the QQD once the wire chamber calibrations have been completed, additional calibrations must be carried out. An accurate calculation of the energy of the detected pion is wanted to help in discarding instances of in-flight pion decay in the spectrometer. The momentum acceptance of the QQD, that is, the solid angle of the QQD at various momenta relative to the central momenta, is needed so that obtained energy distributions of the detected pions can be made independent of acceptance changes. The pion needs to be cleanly identified in TOF through the spectrometer to reject electrons and other spurious backgrounds. Finally, the target coordinates for the events are needed. This last need is discussed here while the other requirements are discussed in the following sections.

The QQD target traceback is established by examining data from runs taken with the nichrome slat targets aligned so that the normal to the target points into the QQD. The target coordinates that are desired are the x and y positions at the target (X_0 and Y_0) and the angles to the central QQD trajectory in the horizontal and vertical planes (TH_0 and PH_0) for the pion in the QQD. The X_0 position is

calculated as

$$X0 = a_1 \cdot X1 + a_3 \cdot X3$$

with a similar expression for $Y0$. By looking at a scatterplot of $X1$ versus $X3$, one finds the ratio of a_1 to a_3 from the slopes of the slat loci and adjusts the magnitude of a_1 and a_3 to give the proper slat separation in the traceback. As there is no quadrupole between the first wire chamber and the target, simple geometry gives the angles, $TH0$ and $PH0$, once the target coordinates are known. Although there is a quadrupole before $WC3$, it is assumed that any δ dependence in the traceback is small enough to safely ignore. During normal running of the experiment, the target is not aligned perpendicular to the QQD, so the physical position of the pion event on the target must be corrected for the target alignment. It is also useful to check the appearance of the empty target under experimental conditions. This is useful in determining the part of the beam striking the target frames and what target cuts are necessary to remove these unwanted contributions. A traceback to the empty target is shown in Figure 13.

III.1.2.1 Delta Coefficients

The two rear wire chambers of the QQD do not lie in the focal plane and so by themselves do not give an accurate indication of the detected pion momentum. The position information of the front two chambers is required to calculate the momentum. For each rear wire chamber then, a value for δ , the percent deviation of the measured particle momentum from the central spectrometer momentum, can be calculated in terms of the rear chamber position and the front end coordinates. The set of front end coordinates used can be either the measured positions in $WC1$ and $WC3$ or the target coordinates derived from them.

Use of the target coordinates in the δ calculation follows the conventions of

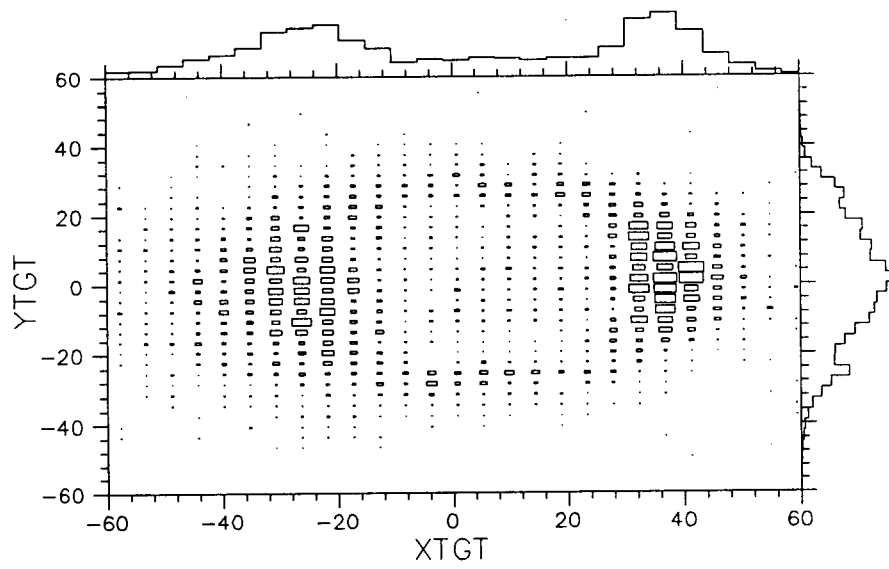


Figure 13: Showing the QQD wire chamber traceback to the empty target to establish cuts for background elimination from the target frame.

the program TRANSPORT [BCIR80] and starting transfer coefficients can be estimated from the program. The direct use of the chamber positions, rather than the target coordinates, avoids relying too heavily on the target traceback and was the approach taken for the offline analysis. The software package QQDMP, developed by a previous student in the group [Bar85b] and slightly modified for use here, is suited to elastic scattering analysis and optimization of magnetic transfer coefficients. The parameterization for the momentum calculation is of the form for WC5 of

$$X5 = A + B \cdot \delta_5 + C \cdot \delta_5^2$$

where A, B, and C are polynomials, usually up to second or third order, of the front chamber coordinates. A similar expression represents δ_4 .

The data used in the optimization process is a set of elastic scattering runs with varying energies. An elastic run is first done with the channel set to provide pions of energy corresponding to the central QQD energy. The QQD is set to some convenient angle such as 50° and a ^{12}C target is used. Additional runs are taken setting the channel to energies spanning the range corresponding to approximately $\pm 20\%$ of the central QQD momentum. One could instead change the QQD setting by corresponding amounts and keep the channel at a fixed setting. This would have the advantage that the beam spot would stay constant from run to run. However, this has the disadvantage that the QQD field shape may change somewhat and the power and water cooling supplies for the QQD would be stressed at the high positive settings.. A changing field shape would make a unique coefficient set difficult to obtain. If, instead, one keeps the QQD setting constant while spanning different channel momenta, the experimental conditions are reproduced.

The scattering events for the set of elastic runs are first screened offline

requiring that all the chambers give valid positions. These events have the wire chamber coordinates written to a file readable by the QQDMP package. With QQDMP and some starting coefficient set, the elastic peak region of each run is selected and any inelastic counts discarded. The desired exact energy location of each peak in the QQD is specified by the channel energy and any energy losses including kinematic losses in the scattering process. QQDMP attempts to modify the coefficients to obtain the desired energies and to minimize the energy width of each peak. For the calibration data used here, the final energy resolution obtained for 82 MeV pions in the QQD is ~ 2.3 MeV (FWHM) which roughly corresponds to the momentum width of the pion beam in the channel. Figure 14 shows a typical energy spectrum for an elastic run.

Some cuts on the data have been imposed in QQDMP to obtain this spectrum to remove in-flight decays of pions to muons. These are the DDIF cut, a cut on the difference of the calculated δ 's, and the ANGL cut, a cut on the polar angle difference between the particle track between WC4 and WC5 as calculated from δ_4 and as calculated from the measured WC5 position. In the offline analysis, the DIFY45 cut, a cut on the difference of the y coordinates in WC4 and 5, replaces the ANGL cut and is essentially equivalent to it. The DIFY45 value is actually calculated as

$$\text{DIFY45} = Y4 - 0.65 \cdot Y5$$

where the 0.65 correction factor compensates for vertical defocussing introduced by the fringe exit fields of the QQD. The optimal value of this correction factor depends upon the calibration obtained for the back wire chamber coordinates.

The intrinsic resolution (that is, ignoring the contributions of the channel and target) of the QQD at 82 MeV is not the 2.3 MeV figure quoted above as this is dominated by the channel momentum width. A better indication of the

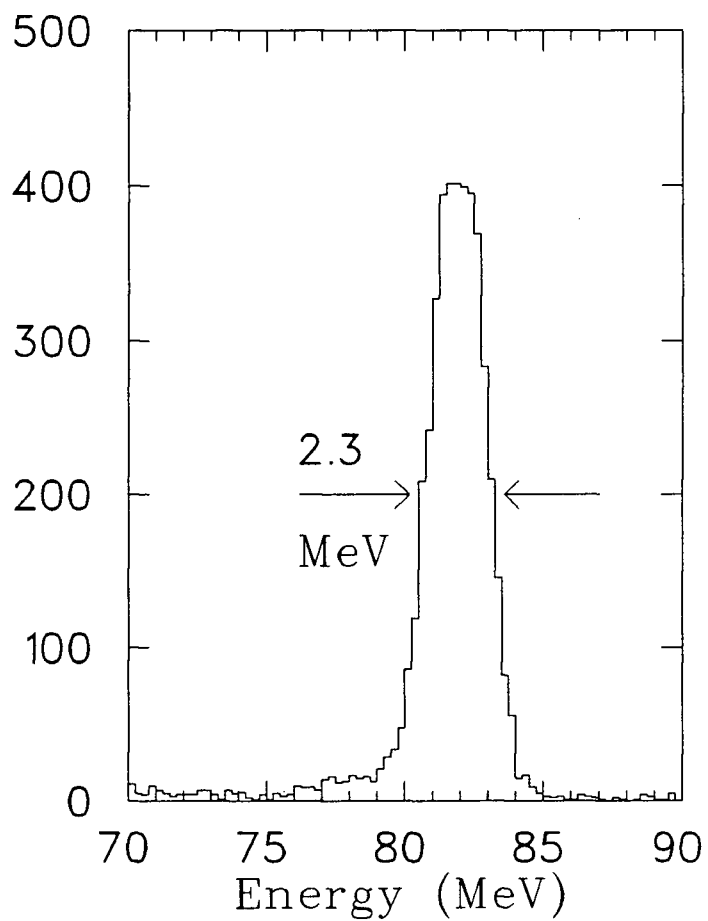


Figure 14: A typical energy spectrum obtained from the calculated δ for the nominal 0% elastic scattering run on ^{12}C .

resolution can be obtained from the DDIF spectrum, whose width should be equal to $\sqrt{2}$ times the intrinsic δ resolution in each chamber. From Figure 15, the obtained resolution is better than 0.9% in DDIF for a momentum (δ) of approximately 0%. This corresponds to an intrinsic QQD energy resolution of 0.9 MeV at a pion energy of 82 MeV.

III.1.2.2 Momentum Acceptance

Once coefficients have been established that give a resolution as good as possible over the desired momentum acceptance range for the QQD, the solid angle as a function of momentum must be determined. The solid angle as a function of momentum from the original commissioning work of the QQD [Sob84,SDB*84] is known. However, this measurement was done by varying the QQD setting and not the channel setting. Also, as the correspondence between a particular QQD magnet setting and central momentum setting is to some extent arbitrary (the central ray is not well established), the 0% setting of the previous work may not necessarily correspond to the defined 0% of the present work.

The literature contains an extensive set of data on $\pi^+ - {}^{12}\text{C}$ elastic scattering reaction over the entire pion energy range used for the QQD calibration work. A sample of these cross sections is shown in Table III where the cross section is given for 50° lab angle. Where this angle was not measured, the cross section was interpolated from given points. The cross sections for the calibration energies were interpolated from the measured energies.

The elastic peaks are fitted with a gaussian shape taking into account the presence of the 2^+ (4.44 MeV) excited state in ${}^{12}\text{C}$. The solid angle at a particular value of δ in the QQD may be calculated by

$$\Delta\Omega = \frac{N_{peak} \cdot 10^{30}}{\phi \cdot N_{tgt}} \cdot J(\theta) \cdot g(\theta) \cdot \sigma_{12C}^{-1}$$

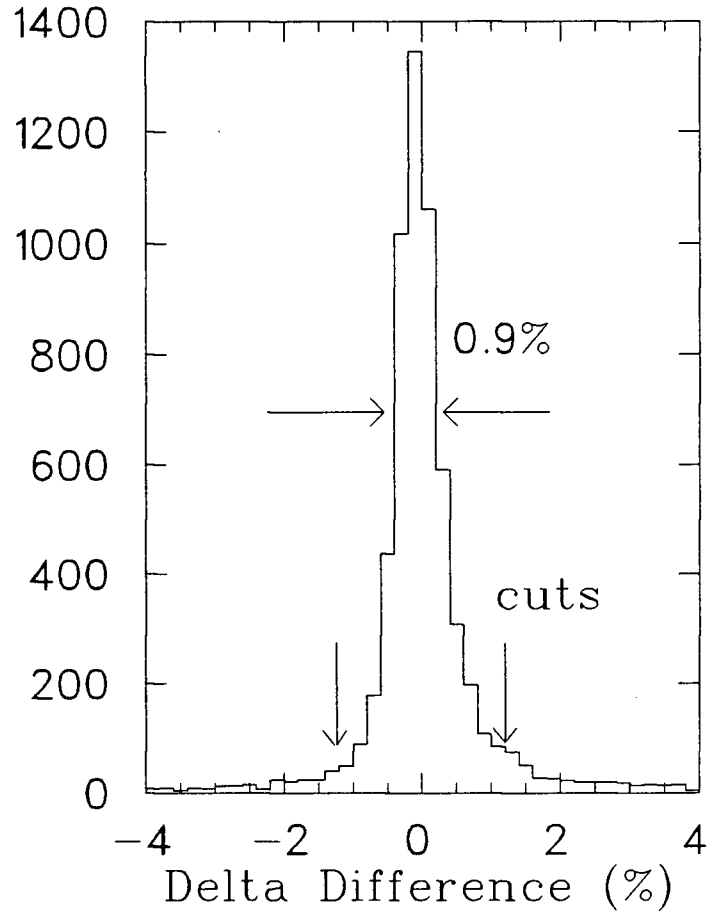


Figure 15: A typical DDIF spectrum, the difference between δ_4 and δ_5 , showing the applied cuts, which is used to aid in removing pions which decay to muons during flight in the QQD. This spectrum also provides a measure of the QQD's intrinsic resolution without the effects of the finite beam energy width.

Energy (MeV)	Cross Section (mb/sr)		Reference
30.3	2.9	± 0.21	[PDD*81]
40.0	3.0	0.17	[BGJ*79]
50.0	4.6	0.28	[PDD*81,SDE*84]
62.8	6.1	0.50	[Bar85b]
65.0	6.08	0.47	[BGB*83]
80.0	9.82	0.84	[BGB*83]
100.0	14.5	1.35	[ABB*84]
148.0	25.0	2.5	[PCE*77]

Table III: Summary of reference ^{12}C elastic scattering cross sections at 50° (lab angle) used to obtain the QGD solid angle as a function of momentum. The errors quoted include normalization errors where given.

where

$\Delta\Omega$ is the derived solid angle in msr,

N_{peak} is the fitted elastic peak area,

ϕ is the beam flux corrected for acquisition dead time,

N_{tgt} is the areal scattering center density of the target,

$J(\theta)$ is the Jacobian converting from lab to c.m. frame,

$\sigma_{^{12}\text{C}}$ is the reference c.m. cross section,

and $g(\theta)$ contains all the efficiency factors in the form

$$g(\theta) = \frac{\cos(\theta_{tgt}) \cdot \text{MHC}}{\text{WC} \cdot \pi\text{-dec} \cdot \pi\mu\epsilon}$$

where

θ_{tgt} is the target angle defined as the angle between the beam direction and the normal to the target,

MHC is the multiple pions per burst correction,

WC is the wire chamber efficiency,

π -dec is the pion decay correction over the length of the QQD,

and $\pi\mu e$ is the pion beam fraction from the channel TOF.

The dead time correction is calculated from the ratio of the number of QQD events written to tape to the number of events recorded in the scalers. The calculated solid angle has the effects of the applied cuts folded into it. The obtained solid angle as a function of δ in the incident momentum is shown in Figure 16. The error is obtained by adding in quadrature all errors of the terms in the solid angle calculation. The largest contribution to the error comes from the uncertainty in the ^{12}C cross sections. The errors used for the cross sections included the normalization errors as the cross sections come from many independent experiments. The shape of the obtained acceptance is somewhat different from that given in [Sob84,SDB*84]. Much of the difference likely arises from a different definition of the central momentum and the different procedure used in the measurement. The solid line in figure 16 results from a fifth order polynomial fit to the data points in the form

$$f(\delta) = \sum_{i=1}^6 a_i \delta_5^{i-1}$$

with the coefficient values given in Table IV

III.1.2.3 Removal of QQD Backgrounds

In previous experiments using the QQD for measurement of low cross section reactions, namely double charge exchange (DCX), a crucial part of obtaining a clean pion spectrum has been the removal of electrons detected with the QQD (see for example [Hes85,AJW*84]). The electrons arise primarily from single charge

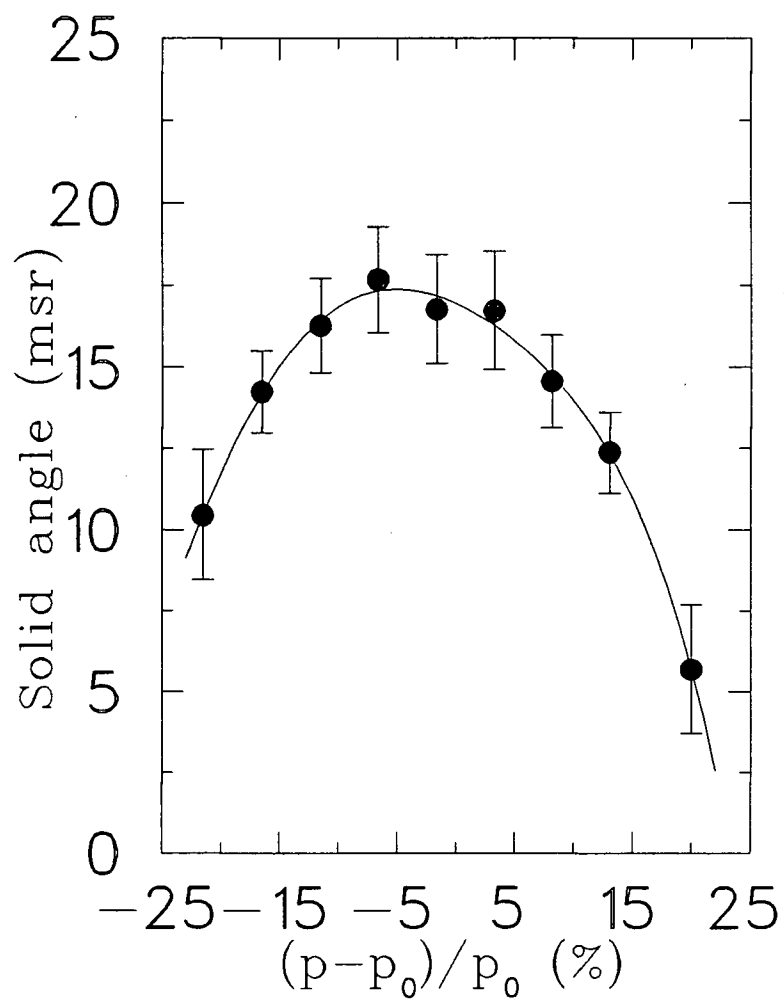


Figure 16: The measured momentum acceptance of the QQD spectrometer showing the solid angle as a function of the percentage change in the scattered pion momentum from the nominal central value.

i	a_i
1	$.16961 \cdot 10^2$
2	$-.16444 \cdot 10^0$
3	$-.13701 \cdot 10^{-1}$
4	$.26452 \cdot 10^{-3}$
5	$-.17271 \cdot 10^{-4}$
6	$-.57245 \cdot 10^{-6}$

Table IV: Table of the coefficients used to describe the QQD momentum acceptance.

exchange in the target or surrounding material. The produced π^0 rapidly decays to two γ 's (in $\sim 10^{-16}$ sec) and one of the γ rays produces an $e^+ - e^-$ pair. The QQD has a long enough flight path to provide a good TOF separation between the electrons and pions provided the pions are not too energetic.

The QQD TOF is provided by the sum of the TDC's for the E1 scintillator. One must keep in mind that the TDC start is defined by the timing of the T1 scintillator in the CARUZ (see section II.3.4). Thus the QQD TOF given by E1 must be corrected by the CARUZ TOF, or more exactly by the flight time from the target to T1 which is given by

$$\text{Correction} = \frac{\text{T1-target distance}}{\text{T1-S1 distance}} \cdot (\text{CARUZ TOF}).$$

The TOF separation in the QQD is demonstrated in Figure 17 where the corrected TOF is shown against the quantity δ_5 for a central QQD energy of 84 MeV. The electrons have a flight time independent of their momentum as their velocity is essentially c . A cut requiring $\text{TOF} > 600$ (units of TDC channels) removes almost all the electrons and few pions. The TOF separation is adequate for almost the entire range of the measured energies, becoming only doubtful at the extreme upper range of the detected π^- energies. There are however, few pions left at high

energy and even fewer electrons so that the separation becomes less important.

Figure 17 also shows that electrons are apparently not the only contaminant in the QQD. From runs with the CARUZ set at 100° , the pion band is quite well defined with none of the background that obscures the data with the CARUZ at forward angles. The additional background arises from $\pi^+ - p$ quasi-elastic scattering off the oxygen or elastic scattering from the protons in the target. The scattered π^+ enter the front end of the QQD and are bent away from the back end by the dipole. The recoil proton strikes the CARUZ and is identified as such (see section III.1.3.2) and has the correct energy for a recoil proton from quasi-elastic scattering. A plot of the opening angle between the two detected particles exhibits a sharp peaking characteristic of a two body event. There exists a high rate of coincidences in the back scintillators of the QQD and the rear chambers, possibly caused by residual protons delivered near the target location by the beam line. The timing of these coincidences does not appear to be strongly correlated to the pions in the beam. Occasionally, these randoms will come into coincidence with a quasi-elastic π^+ front end event. To eliminate these spurious events, which will mostly effect the $\pi^- - p$ coincidence spectra, reasonably tight cuts in the DDIF and DIFY45 spectra must be made. Also, a cut must be applied to the pion band in Figure 17, where the cut has been established from an experimental setting where there is not a quasi-elastic background present. The expected flight time can be calculated from the momentum or energy of the pion and the limits shown in Figure 17 can be established to remove as much as possible of the background.

III.1.3 CARUZ Calibration

There are many factors to be properly taken into account to obtain the optimal resolution from the CARUZ. The pedestal values and integrated charge per

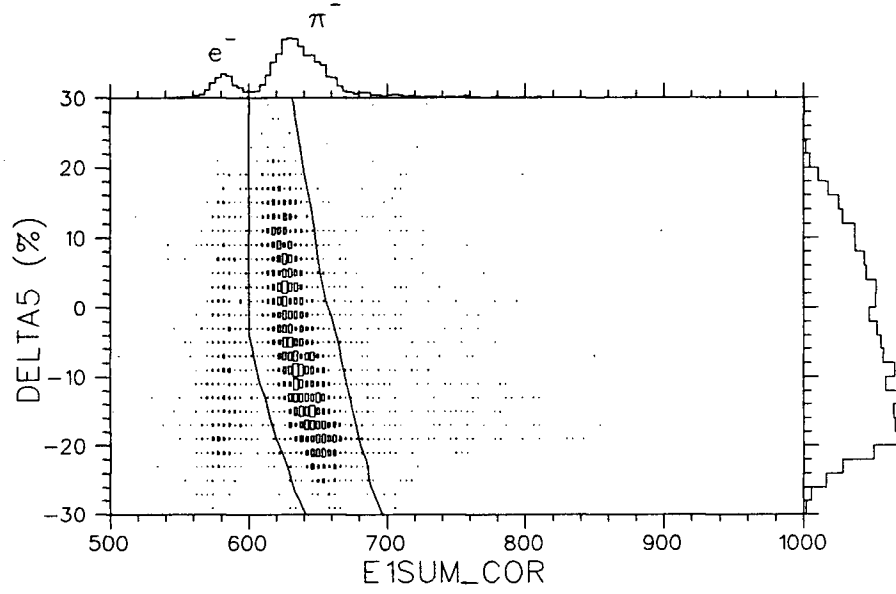


Figure 17: Scatterplot of δ_5 against the timing in E1 corrected for the particle flight time in the CARUZ. The central energy of the QGD is 84 MeV. The $e - \pi$ separation is clear. The pion definition band shown is the intersection of the electron removal and pion TOF band cuts for this setting.

channel for the CAMAC ADC need to be known for pulse response conversions. The time to channel conversion for the TDC is needed to obtain accurate time scales. The ADC is calibrated by feeding a logic signal into the ADC which produces a near full-scale value and then giving a range of attenuations to the input logic signal. The ADC output is fitted to a linear function of the relative pulse height. It is not important to establish an absolute charge calibration, but a relative calibration for all the CARUZ ADC's is important. The TDC is nominally on a 50 ps per channel scale. A stop signal to the TDC is provided with a variable delay relative to the start and the TDC output is found as a linear function of the delay.

The two wire chambers in the CARUZ are calibrated as detailed earlier except that the offsets are determined by requiring that the position is zero when the CARUZ sits at 0° in the beam. The particle tracing with the wire chambers back to the target and forward to the scintillator is simply determined by the geometry of the CARUZ. The traceback to the target is initially done to a plane whose normal points directly into the CARUZ which does not necessarily correspond to the physical target position. In comparing the CARUZ and QQD target tracebacks, the true target orientation must be accounted for as must the fact that the each device views opposite sides of the target. The CARUZ wire chambers are inefficient due to the high particle flux they encounter close to the target. However, the CARUZ traceback is not crucial to the analysis as the QQD traceback gives a clean picture of the scattering target and the S1 timing discussed below gives a good measure of the position in the stack.

III.1.3.1 Pulse Response and TOF

The CARUZ was originally built with the intention of detecting pions. As an accurate determination of the kinetic energy is desired in addition to simply

discriminating the pions from electron and proton backgrounds, the scintillators must all be calibrated with some common pulse characteristic. The M13 channel was used for the initial calibrations to provide pion beams of variable energy with electron and muon contaminations that could be easily separated by TOF down the channel. Electrons with energy greater than 20 MeV pass completely through the stack with a virtually constant dE/dx over their energy range. The response of NE102A scintillator material to electrons is linear, that is, a given ΔE of the electron in the material produces the same light output independent of the electron energy (this is true down to electron energies less than 1 MeV [CS70]). This is not the case for heavier particles such as protons. Thus, as long as the electron energy is not so large as to produce extensive electromagnetic showers in the stack, the electrons should produce pulses in the scintillators simply proportional to the scintillator thickness.

Electrons of 150 MeV were chosen (corresponding to 65 MeV pions) for the response bench mark. The electrons were initially fired through the center of the CARUZ. The scintillator pulses were read into the calibrated ADC's. The ADC outputs were then corrected for the slopes and pedestals and scaled so that the mean of the electron ADC distribution corresponded to a value equal to one-half of the respective scintillator thickness in millimetres. Thus, summing the ADC outputs for passing electrons from each end of a scintillator gave the thickness of that scintillator.

The light produced by ionization in the scintillator must traverse a length of scintillator material before reaching the light guide to the phototube. The light will then be attenuated by its passage by an amount dependent upon the distance from the light guide. This attenuation is approximately exponential. To correct for this attenuation, the 150 MeV electrons were also fired through the stack at varying angles to span the horizontal dimensions of each scintillator. The summed

(left plus right) response of each scintillator as a function of horizontal position can then be found, allowing one to correct the response to that of the central region of the CARUZ. The individual responses (left or right) were fitted with an exponential curve to determine the effective attenuation lengths, λ_{eff} , of each scintillator. The values found are 1.2 m, 1.8 m, 2.0 m and 1.6 m for S1 to S4 respectively. These values are all less than the nominal value of 2.5 m [NE86] and reflect effects of varying geometry and light collection efficiencies of the components in the CARUZ.

The TOF scale is calibrated by looking at the mean time results for the electrons (with velocity $\simeq c$) and determining the TDC channel which corresponds to zero flight time. The mean time of the particular event can then be converted to a TOF by the TDC calibration performed earlier and to a velocity if desired. The S1 position is determined by the difference of the mean timing and right timing of the event in an analogous fashion to the wire chamber position determination. The calibration is done by relating the time difference to a known position for the series of varying angle runs used for the attenuation correction data. A measure of the resolution can be inferred from a comparison of the position given by the wire chamber tracing and that from the S1 TDC values. A combined resolution of better than 3 cm is obtained, which corresponds to a timing resolution of the S1 stop of approximately 250 psec given the transit speed of light in the scintillator material.

With the calibration resulting from the electron data, the response of the CARUZ to pions can now be examined. The M13 channel was set to provide pions at various energies in the range of 10-65 MeV. Pions were stopped in the centre of the CARUZ in the S1 to S4 scintillators (for $T_{\pi^+} < 60$ MeV) and the light outputs measured. A stopping pion spectrum for 50 MeV pions is shown in Figure 18. It displays several characteristic features of the stopped pion results. The FWHM

resolution of the peak corresponds to an energy width of 2.0 MeV. The CARUZ resolution as a function of incident energy is summarized in Table V. The peak shape is gaussian with a small low energy tail. The main peak results from the response of the CARUZ to the stopping pion plus the energy of the decay muon (4.11 MeV) while the smaller side peak is that of stopped pions that have not decayed into muons in the time span of the electronics gate width (~ 40 nsec). Approximately 80% of the stopping pions decay into muons for the electronics configuration used in the calibration and slightly less for the actual experiment where a tighter trigger was used. The separation between the two peaks corresponds to only a 2.5 MeV difference when the linear conversion of response to energy is used (discussed in section III.1.3.2). This corresponds to the response of the material to a 4.11 MeV muon which, due to the closeness of its mass to that of the pion, could also be used as a measure of the response of the material to a 4.11 MeV pion. Other backgrounds in the figure correspond to muons from pion in-flight decay and pions (or muons) that escape the CARUZ before stopping through scattering or other reaction loss mechanisms.

In addition to the stopped pion data points, a few measurements with stopping particles other than pions were done. With the M13 channel, 20 MeV/c positrons were selected as this is essentially the highest energy for positrons that will stop in S4. Any residual muons or pions in the beam could be safely ignored as they had insufficient energy to pass the T1-S1 event definition. With the TRIUMF M11 channel, protons with momenta corresponding to the pion energies used in the $^{16}\text{O}(\pi^+, \pi^+\pi^-)$ experiment were fired into the CARUZ. The two proton energies used were 62.7 and 69.0 MeV, the energy difference given by the proton energy loss in the water target which was present for the lower energy run. The resolution obtained for the 69.0 MeV protons was 2.1 MeV. The response of

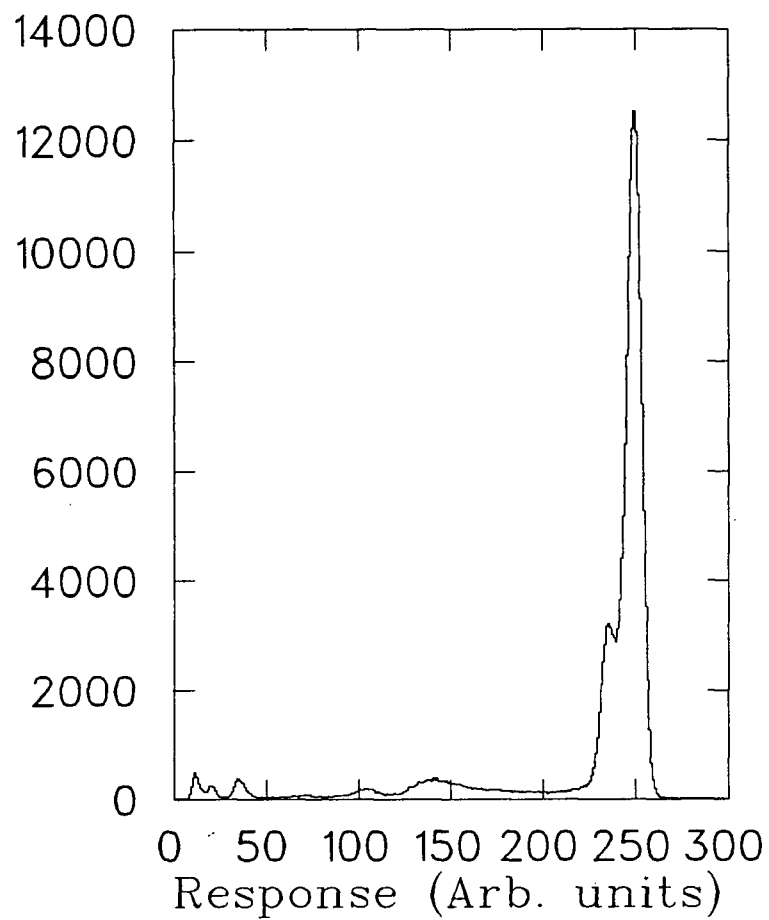


Figure 18: The response spectrum produced by 50 MeV stopping pions.
The features of the spectrum are discussed in the text.

Stopped Particle	Response (A.U.)	Kinetic Energy (MeV)	Resolution FWHM (MeV)
e^+	100.4	18.8	1.5
μ^+	14.0	4.1	0.4
proton	232.5	62.7	2.3
	257.6	69.0	2.1
π^+	38.1 (53.9)	9.6	1.7
	77.7 (91.8)	17.9	1.7
	102.8 (116.5)	23.5	1.7
	116.9 (130.6)	26.3	1.6
	129.9 (143.6)	28.8	1.6
	154.4 (167.7)	34.1	1.6
	179.0 (193.0)	39.4	2.1
	206.3 (220.3)	44.3	2.0
	233.6 (249.4)	49.2	2.0

Table V: Response data for the CARUZ. The values in parentheses include the response of the CARUZ to decay muons from the stopped pions. The response is given in arbitrary units as determined by the electron calibration discussed in the text.

the CARUZ to the positron and proton energies tested is summarized in Table V.

III.1.3.2 Energy Calibration and Mass Separation

The procedure used for discriminating pions from positrons and protons is similar to that employed for mass-separation of protons, deuterons and tritons in an earlier device used by [CGP*83]. Discrimination of the pions from positrons is clearly evident in Figure 19. Positrons can deposit a maximum of 20 MeV in the CARUZ (excluding showers) and are essentially all travelling the same velocity. The $E \cdot \Delta E$ quantity is simply the total response in S1 to S4 (E) multiplied by the response in S1 (ΔE) and Beta is the particle velocity, in units of the velocity of light, calculated from TOF in the CARUZ. The $\pi^+ - e^+$ discrimination is good throughout the range of energies of the stopping pions.

A plot of TOF versus $E \cdot \Delta E$ is used to discriminate the pions from heavier particles such as protons and deuterons. The discrimination achieved is shown in Figure 20. The tail to the left of the proton group is likely a result of reaction losses for the stopping protons. The TOF- $E \cdot \Delta E$ discrimination between pions and protons (and deuterons) results in the TOF- E spectrum of Figure 21. Note that the electrons have already been suppressed from both of Figures 20 and 21 and would appear in the lower left corner in each. These spectra were obtained from experimental data from the 1986 runs [GRR*87]. Note that the TOF, BETA and ΔE quantities have been corrected for the deviation of the particle flight path from the central trajectory through the CARUZ.

As most of the stopping pions will decay into muons, which also stop in the CARUZ during the width of the electronic gate, the corresponding total light output of the stopped pion and decay muon is the quantity that will be related to the incident pion energy. The response of the scintillator stack to the stopping

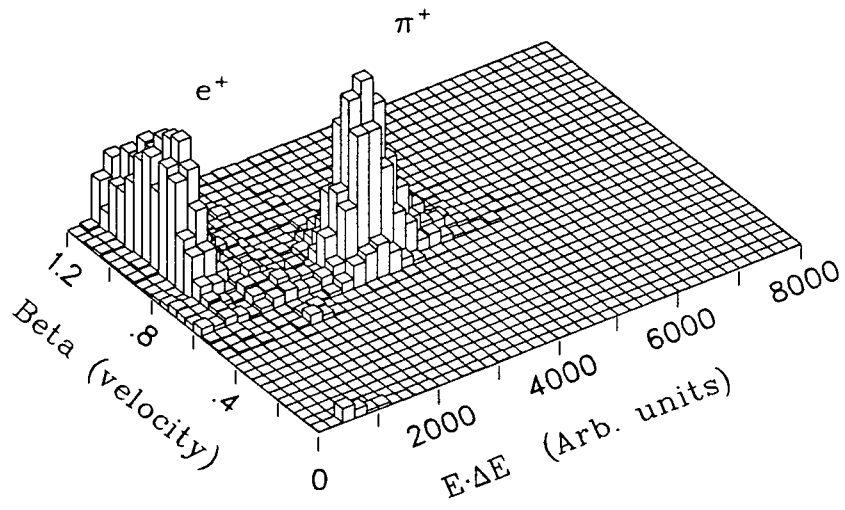


Figure 19: Showing the $\pi^+ - e^+$ mass separation in a velocity versus $E \cdot \Delta E$ plot for 128 MeV/c particles (50 MeV pions).

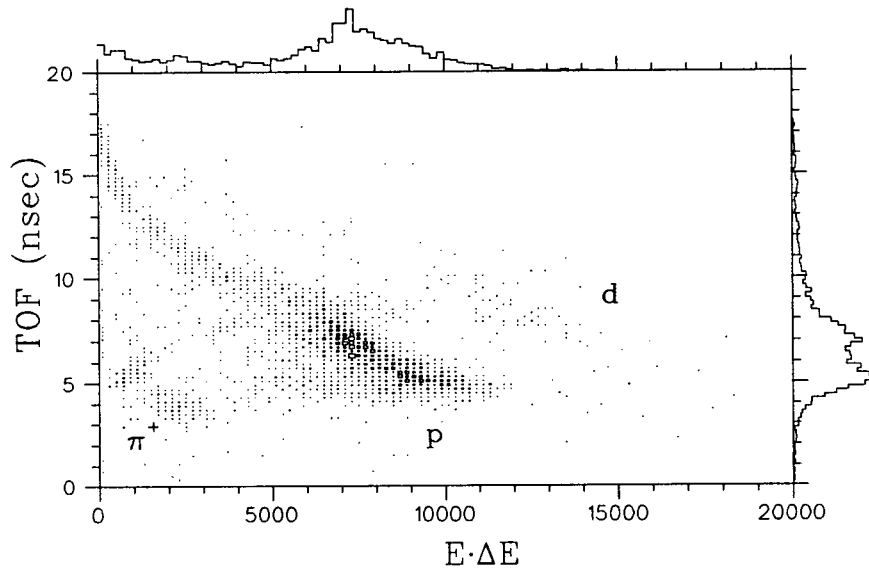


Figure 20: A TOF- $E \cdot \Delta E$ plot showing the separation of the pion and protons in the CARUZ. Some deuterons are also visible.

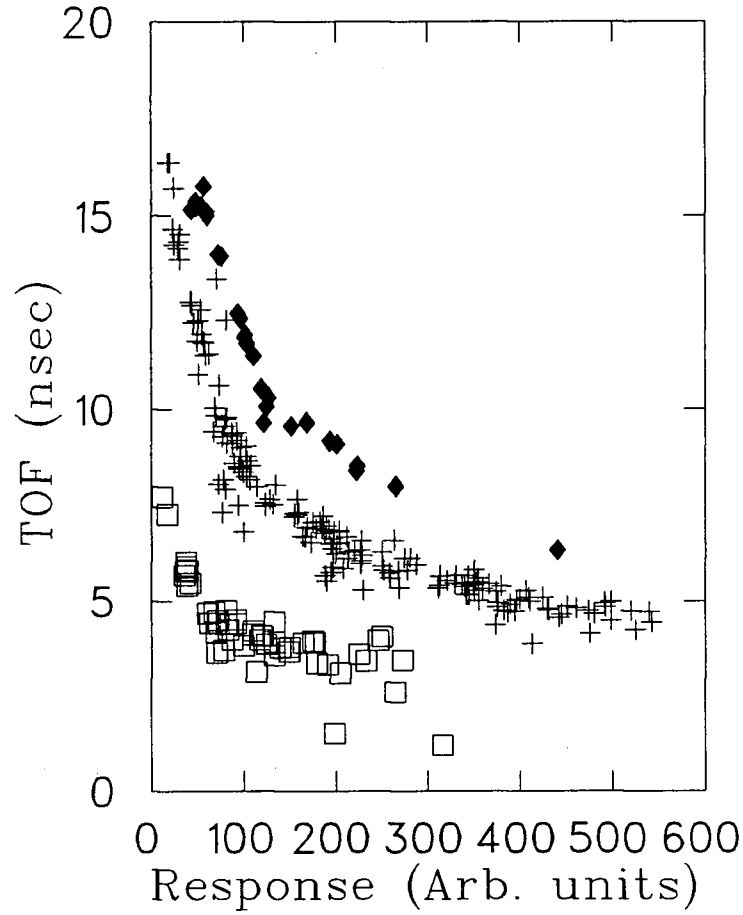


Figure 21: A TOF-E plot showing the $\pi^+ - p$ (and deuteron, d) separation where π^+ , p and d are denoted by squares, pluses and diamonds respectively. The particles were mass-identified from the $E \cdot \Delta E$ plot.

pions and the associated decay muon is very nearly linear. This can be seen in Figure 22 which shows the light output plotted against the pion incident energy at the front of the stack for the cases of the stopped pion alone and the pion plus decay muon. A curve of the form

$$L(E) = S \cdot E + E_0$$

has been fitted to the pion plus decay muon points yielding $S = 4.86 \text{ MeV}^{-1}$ and $E_0 = 4.26$. The deviations from linearity are small, being less than the intrinsic CARUZ resolution. The largest deviations occur at low pion energies where other uncertainties in determining the actual energy dominate (for example, the uncertainty in particle energy due to unknown losses in the scattering target). This simple linear conversion of the response gives the energy of the incident pion at the front of the stack. The actual particle energy at the target must be obtained by accounting for the known average energy losses in the material in front of the stack (MWPC's, T1, air, etc.).

It is also important to examine the response of the CARUZ to the stopping pions alone. The information from the stopped pions can be examined in the context of Birk's formula [CS70] which relates the light output to the energy of the particle by

$$L(E) = S \int_0^E d\varepsilon [1 + kB(d\varepsilon/dx) + c(d\varepsilon/dx)^2]^{-1}.$$

The stopping powers are calculated using the NE102A characteristics given in [AEK71]. For simplicity, $c = 0$ is taken. Birk's formula is fit to the stopped pion points with the result for the product

$$kB = .0114 \pm .0017 \text{ (cm/MeV)}$$

and for the normalizing factor

$$S = 5.11 \pm .09 \text{ (MeV}^{-1}\text{)}.$$

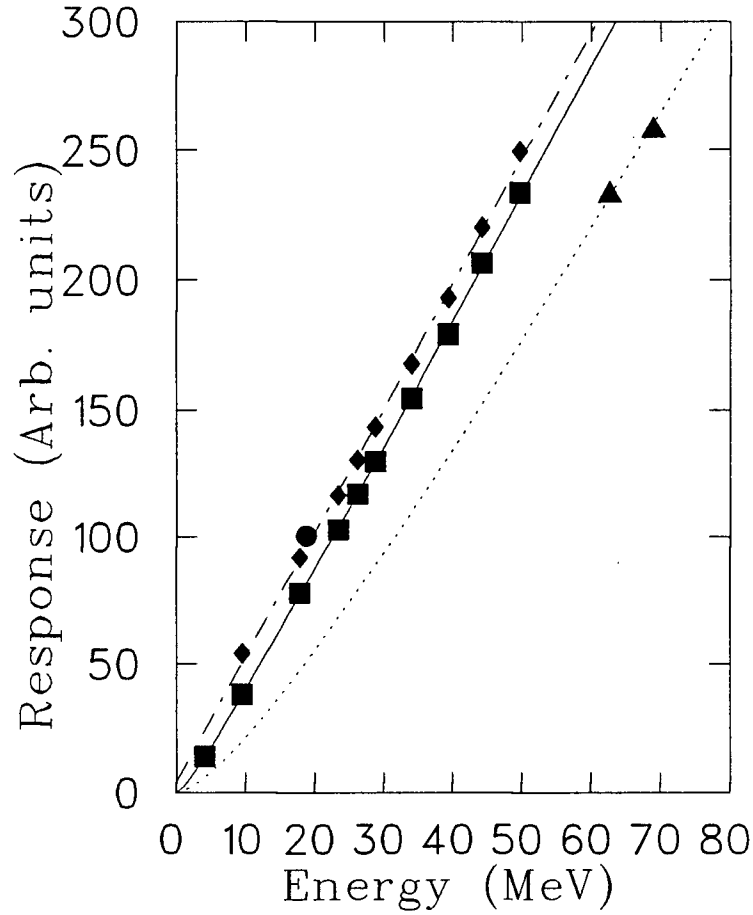


Figure 22: Response of the CARUZ to positrons (circles), stopping pions with decay muon (diamond) and linear fit (dash-dot line), stopping pions alone (squares) and Birk's formula fit (solid line), stopping protons (triangles) and Birk's formula fit (dotted line). Error bars are smaller than the drawn points. See text for more details.

The fit to the data is shown in Figure 22. The errors used in the fit are the standard deviations of the energy peak, not the standard errors of the means and thus are certainly an over estimate of the errors as indicated by the reduced chi-squared of the fit ($\chi^2/\nu = 0.1$). However, there are other small systematic errors that are likely to be larger than the standard error but are difficult to accurately estimate (such as uncertainties in the actual energy scale, calibration errors, etc.). In addition to the error quoted above for kB , there is an additional uncertainty, estimated to be approximately 5%, due to the uncertainty in calculating the stopping powers for NE102A.

The data resulting from the stopped positrons and protons can be compared to the pion data. As stated earlier, the response to electrons is expected to be linear. Thus, one should be able to draw through the origin a straight line with slope equal to the S obtained in the fit of Birk's formula to the pion data. From the 20 MeV/c positron results given in Table V and shown in Figure 22, we see that this is true to better than five percent. The proton data can also be fit by Birk's formula using the same value of S but allowing kB to vary. With this constraint, a value of $kB = .015 (cm/MeV)$ fits the two proton data points as shown in Figure 22. While these few additional points are insufficient to allow an exacting comparison of the response of the CARUZ protons and positrons, they do allow one to check the consistency of the pion results with previously known characteristics of stopping protons and positrons (electrons) [CS70].

The ADC's were initially set up with attenuators on the inputs so that pions would not cause overflows in the units. Stopping protons can release much more energy than stopping pions and caused the ADC's to overflow on occasion. The ADC values were recovered in most cases as the overflow usually occurred when then proton stopped on one side of the CARUZ, overflowing that ADC channel but still providing a proper signal in the opposite end. The expected ratio of left

to right pulse height is known from the attenuation correction described above enabling the overflow value to be predicted. This will of course result in a minor loss in resolution for the proton energy determined.

Another problem in the phototube outputs occurred which necessitated a similar correction to the overflow recovery. For some runs where the CARUZ was at -50° , the S1L base signal sagged by a non constant amount. The sagging was beam related (ie. it did not occur for runs with the CARUZ at -100° done immediately before and after). The proper S1L was recalculated from the calculated position in S1 and the value in S2L. Again a small energy resolution loss is likely to result, but no mass-separation difficulty was found.

A final comment on the CARUZ calibration can be made concerning reaction losses in the stopping of the pions. One method of estimating losses is to use the empirical form from [RSM68] for the inelastic cross section

$$\sigma_{inel}(E) = \frac{70}{32} A^{\frac{2}{3}} \{E^3 - 12E^2 + 36E\}$$

where E is given in units of hundreds of MeV, the inelastic cross section in units of mb and A is the atomic number of the components of the scintillator material. The reaction loss can then be obtained by numerically integrating the intensity loss

$$d\left(\frac{I(x)}{I_o}\right) = - \sum_A (N_A \cdot \sigma_A(E(x))) \cdot \exp\left\{- \sum_A N_A \sigma_A(E(x))\right\} \cdot dx$$

as the pion comes to rest in the scintillator material. Here, N_A is the scattering center density in the scintillator material of nucleus A , A being either ^{12}C or ^1H . For 50 MeV pions stopping in NE102 the loss amounts to 6.5%. These losses would be important for a measurement such as an elastic cross section where a specific energy peak region is of interest. Many of these "reaction loss" pions would still be identifiable as pions in a TOF versus $E \cdot \Delta E$ test as they would have a good TOF and ΔE although the energy determination would be incorrect. In

the $(\pi, 2\pi)$ experiment then, many of these reaction loss pions will not be lost from the measurement of the total cross section but would however result in a slight distortion of the measured energy spectrum in the CARUZ. We thus ignore the effects of reaction losses.

III.2 Cross Sections

During the analysis of the data, weight factors are computed for each event which depend upon the energies and angles of the detected pions. These weights are then used in the histogramming of the events. Inclusion of the weight here means that the applied corrections can be later ignored in calculating the differential cross sections. The statistical accuracy of the data is determined from histograms of the unweighted counts. The numerical factors for the corrections are discussed below.

The momentum acceptance function for the QQD spectrometer was determined earlier. The solid angle of the central part of the QQD, that is, at $\delta = 0^\circ$, is taken to be 17 msr. Each π^- detected is then weighted according to the solid angle corresponding to its calculated momentum so as to make the QQD solid angle independent of δ . That is, a weight is applied given by

$$\frac{17.}{f(\delta)}$$

where $f(\delta)$ is the solid angle calculated from the polynomial fit discussed earlier.

The S2 scintillator is the scintillator used to define the CARUZ solid angle. The S1 scintillator of the CARUZ, as used for the 1986 data taking, subtended a larger solid angle than did S2 and thus could accept more particles. This was corrected by weighting those events that only struck S1 by the ratio

$$\frac{\Omega_{S2}}{\Omega_{S1}} = .8106.$$

The S1 scintillator was cut down to the same solid angle as S2 for the 1987 data so that for that data, this weight is not necessary. As the S2 scintillator has a

constant vertical size, the solid angle subtended by each angular division is not constant and depends upon the distance from the center of the scintillator. A weight is applied to correct the solid angle to the value for the central portion of the CARUZ. It is calculated from the ratio of the vertical angle subtended by the center of the CARUZ to the subtended angle at the point the π^+ strikes the CARUZ, given by

$$\arctan\left(\frac{110}{993}\right) / \arctan\left(\frac{110 \cdot \cos(\theta_{CARUZ})}{993}\right)$$

where θ_{CARUZ} is the angle of the π^+ relative to the center of the CARUZ, 110 mm is one-half of the height of S2 and 993 mm is the distance from the target center to the center of S2.

The π^- can decay into μ^- as they traverse the QQD. Most of the decay muons will exit the QQD as most are emitted close to the characteristic muon decay cone angle for the original π^- energy. The muons that do not escape the QQD will mostly be removed by the track consistency cuts DDIF and DIFY45 discussed earlier. The survival fraction, N_{π^-surv} , can be calculated from

$$N_{\pi^-surv} = \exp\left(\frac{-m_{\pi}d}{p_{\pi}c\tau_0}\right)$$

where d is the distance from the target to the last wire chamber, 2.38 m, τ_0 is the pion lifetime in the lab frame, 26.3 ns, and c is the speed of light. The weight then applied to the data is $N_{\pi^-surv}^{-1}$. The π^+ can also decay before reaching the CARUZ, but as no muon cuts are made, the fraction of pions surviving to strike the CARUZ was estimated from REVMOC and a weight equal to $N_{\pi^+surv}^{-1}$ is applied to the data.

The ^{16}O target has a finite width, thus the produced pions will lose a fraction of their energy traversing the target material before exiting into air towards the detection apparatus. Some of the produced pions may even stop in

the target if their energy is small. As the CARUZ usually detects the lower energy pions, any losses will be more severe for the π^+ . It is possible, however, to extract the true energy distribution of the π^+ from the measured energy distribution (energy distortions due to pion decay and reaction losses in the CARUZ are ignored in this part of the discussion) as shown in [CSZ76].

If the pion source is taken to be evenly distributed throughout the target and defining the following quantities;

$P(E_p)$ is the true probability that a particle is produced in the energy interval $(E_p, E_p + dE_p)$,

$R(E)$ is the range of the pion as a function of its energy

L is the target thickness in the direction of the CARUZ

N_0 is the total number of particles produced

$\nu(E_m)$ is the measured energy distribution

one then has, from [CSZ76],

$$P(E_p) = \frac{L}{N_0} \left(\nu(E_p) \frac{R''(E_p)}{R'^2(E_p)} - \frac{\nu'(E_p)}{R'(E_p)} \right)$$

where the derivatives are with respect to E_m and evaluated at E_p . The unfolded distribution is then $N_0 P(E_p)/L$.

For the purposes of this analysis, the expression for $\nu(E_m)$ was determined from a polynomial fit to the energy spectrum of the π^+ in the CARUZ for the data subset of the CARUZ at -50° and the QQD at 50° . This energy spectrum is typical of much of the measured data set. The quantity in parentheses above then becomes another weight to be applied to the data on an event by event basis. The weights are generally close to one (within 10%) except for pions below ~ 15 MeV. The target loss weight is shown as a function of pion energy in Figure 23.

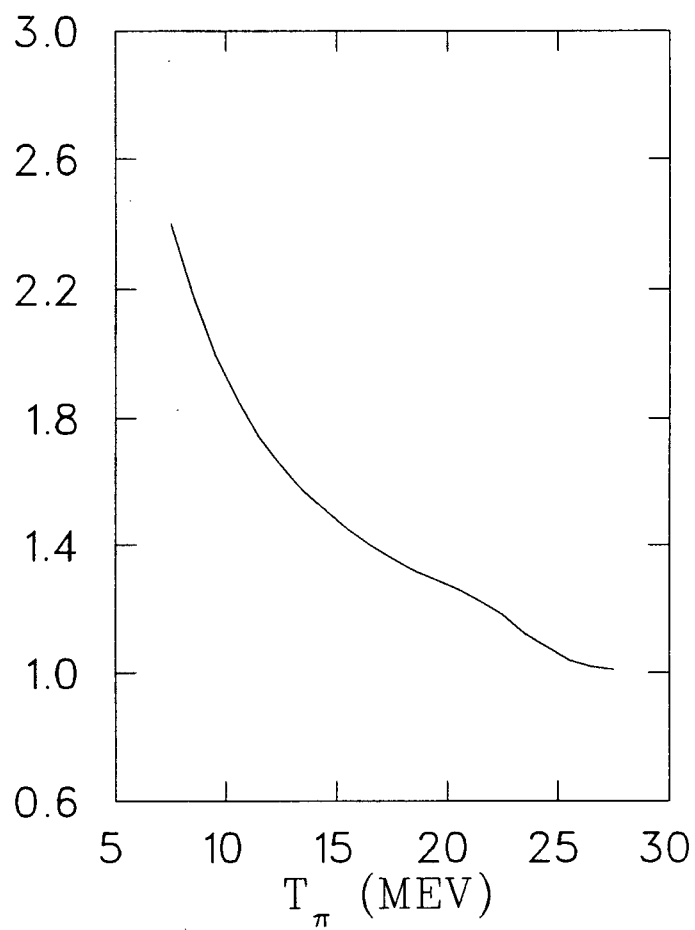


Figure 23: The target loss correction as calculated by the method from [CSZ76]

III.2.1 Calculating Four-Fold Differential Cross Sections

The four-fold differential cross section may be written in the lab frame as

$$\frac{d^4\sigma}{d\Omega_{\pi^-}d\Omega_{\pi^+}dT_{\pi^-}dT_{\pi^+}} = \frac{\cos(\theta_{tgt})}{\phi \cdot N_{tgt} \cdot WC} \cdot \frac{dN_c}{\Delta\Omega_{\pi^-} \cdot \Delta\Omega_{\pi^+} \cdot \Delta T_{\pi^-} \cdot \Delta T_{\pi^+}}.$$

dN_c is the number of counts in a bin with energies in the interval

$$T_{\pi^-} - \frac{1}{2}\Delta T_{\pi^-} \rightarrow T_{\pi^-} + \frac{1}{2}\Delta T_{\pi^-}$$

and

$$T_{\pi^+} - \frac{1}{2}\Delta T_{\pi^+} \rightarrow T_{\pi^+} + \frac{1}{2}\Delta T_{\pi^+}$$

in the solid angle windows $\Delta\Omega_{\pi^-}$ and $\Delta\Omega_{\pi^+}$. The factor WC is the QQD wire chamber efficiency, which for the $(\pi, 2\pi)$ data averaged about 0.60. The beam flux, ϕ , is given by one of two expressions, depending upon the configuration used to measure the beam. In terms of the hodoscope flux, one has

$$\phi = \text{HODO} \cdot c_{\pi} \cdot \text{DT}$$

or for the PCOS case,

$$\phi = \frac{\text{PCOS}}{\text{eff}} \cdot \text{MHC} \cdot \text{DT}.$$

The c_{π} is the hodoscope calibration factor determined earlier, DT is the acquisition system dead time correction, and *eff* and MHC are the PCOS efficiency and multiple hits corrections respectively. The event rates for the $(\pi, 2\pi)$ runs were typically less than one per second, so that the system dead time was essentially negligible. The areal scattering center density, N_{tgt} , is given in Table II.

The cross sections are all evaluated in the laboratory frame. Evaluation in the center of mass frame would not allow the data to be presented in as clear a fashion as will be presented here due to the configuration of the apparatus. For example, the QQD momentum acceptance allowed is 33% (-18% to +15%). To

present results in the center of mass frame would require that one find an average momentum representing the entire setting and then transform all the data as one point into the center of mass frame. Alternatively, the QQD acceptance could be divided into sections, an average energy found for each and then each segment transformed into the center of mass frame. Each segment will then appear at a different center of mass angle. Additionally, one would have to decide whether to use the $\pi - N$ or $\pi - A$ center of mass frame. The only detailed differential cross section predictions available are from [OV87] and are available in the lab frame. The total cross section can be evaluated independent of frame of reference. Thus, for coherence of presentation, the data will be analyzed and presented in the lab frame.

III.2.2 Integrated Cross Sections

The measured four-fold differential cross sections can be partially integrated to yield lower order differential cross sections or fully integrated to yield a total cross section. For either choice, the unmeasured portions of the energy and angular spectra, that is, the missing phase-space, must be accounted for. The errors involved in the extrapolations must be carefully considered and included in the overall estimation of the accuracy of the experiment. The procedure used to perform the integrations shall be outlined here.

The first step taken is the consideration of the four-fold differential cross section as a function of the π^+ energy in the CARUZ. These spectra are typically peaked at low energies as shown in Figure 24. The missing parts of the spectrum are the part from 0-8 MeV and above the high end energy cutoff of 55-60 MeV. The QQD was set to accept π^- from 35-110 MeV (except for the 115° data where only the range 65-110 MeV was measured). The energy available to the pions is approximately 120 MeV, (280 MeV minus the pion mass, centre of mass energy

and binding energy for the struck nucleon) which generally forces the π^+ to be of lower energy than the π^- . In Figure 24 the measured π^+ energy distribution at 50° is shown. The errors shown indicate the statistical accuracy of the data. The spectrum should decline to zero at 0 MeV from phase-space considerations. This constrains the possible spectrum shape below 8 MeV. Above the CARUZ energy cutoff, the spectrum must also decline to zero. An exponential power series in the π^+ kinetic energy of the form

$$F(T_{\pi^+}) = \exp\left(\sum_{i=0}^n a_i x^i\right)$$

is fit to the measured energy spectra forcing the fit to go through the origin and to go to zero above the cutoff. A fourth order polynomial was found to be sufficient to describe the spectrum. The weight applied in the fit for the first data point at 10 MeV, containing the data down the the lower energy threshold of the CARUZ, 8 MeV, is artificially reduced to allow for some uncertainty in the pion source loss correction described above. The data points above 50 MeV are not included in the fit as some of the high energy pions do not stop in the CARUZ if they pass close to the stack center. The area under the fit is then compared to the area under the measured data. This ratio provides the factor to correct for the missing part of the T_{π^+} spectra. The error in the extrapolation is estimated by performing the fit with relaxed constraints on the origin and high end cutoff points to see how the fitted area changes and also by comparing the areas of fits of different polynomial degrees. The resulting power fit to the energy spectra for the data with the QQD at 50° is shown in Figure 24. The obtained correction factors for the π^+ energy spectra for the three QQD angles are given in Table VI.

The next integration is carried out on the energy of the π^- in the QQD. The correction factor from the integration on the π^+ energy is used to give a triple differential cross section as a function of the π^- energy. It is assumed here that

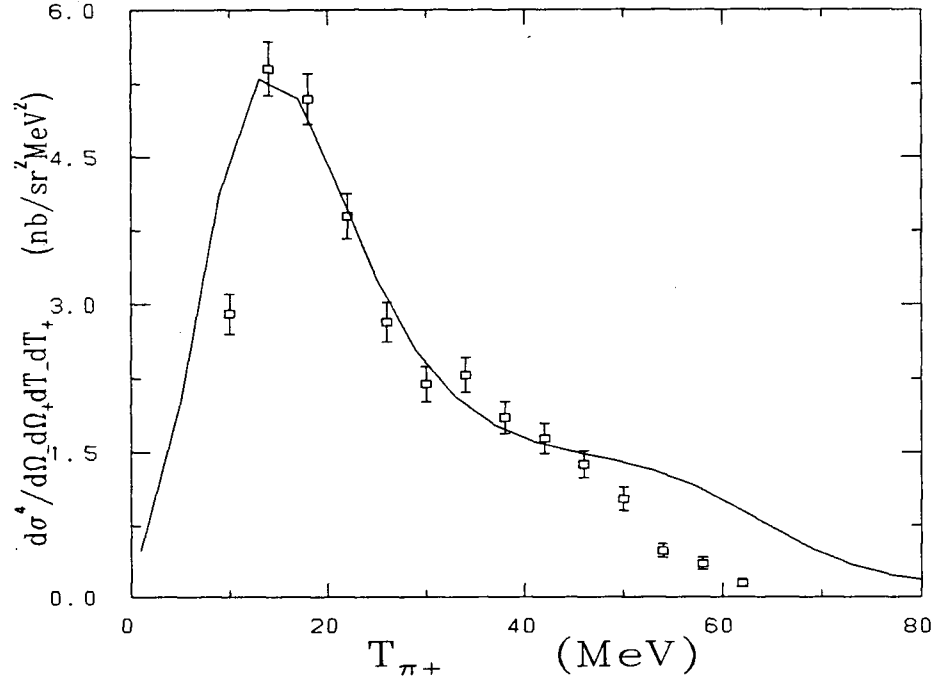


Figure 24: The measured energy distribution of π^+ in the CARUZ with the full data set with the QQD at 50° and the fitted polynomial. The fitting constraints are discussed in the text.

QQD Angle	T_{π^+} Factor	Error	T_{π^-} Factor	Error
50	1.45	.05	1.55	.08
80	1.43	.06	1.67	.08
115	1.35	.06	6.5	1.5

Table VI: Correction factors for extrapolating the π^+ energy spectra in the CARUZ and the π^- spectra in the QQD.

any change in the shape of the π^- energy spectrum that would result from detecting the whole π^+ energy spectrum is small. The energy range covered in the QQD required two momentum settings, one centred at 55 MeV and one centred at 84 MeV. A typical π^- energy spectrum is shown in Figure 25. The correction factor for the π^- spectrum is obtained in the same manner as for the π^+ . A exponential polynomial of second order is found to be sufficient to describe the π^- distribution. The QQD measured up to 110 MeV, near the end point for the spectra, so that few high energy pions are lost. The measured π^- energy distributions resemble the phase-space predictions (discussed in Chapters 4 and 5) which again constrains the spectrum to pass through the origin. The error estimation in the extrapolation is carried out similar to the π^+ . The extrapolation results are shown in Figure 25 and are summarized in Table VI.

The 115° data presents a problem here due to only having the upper end of the π^- energy spectra measured. The predictions of the model of [OV87] will be shown to reasonably describe the π^- energy spectrum. Thus we take the shape of the model distribution and normalize it to the measured section of the 115° data. The ratio of the model distribution area to the measured area provides the necessary correction. Unfortunately, the lack of a full energy spectrum here necessitates a large error estimate for this correction.

The angular distribution of the π^+ is the next variable integrated. Having

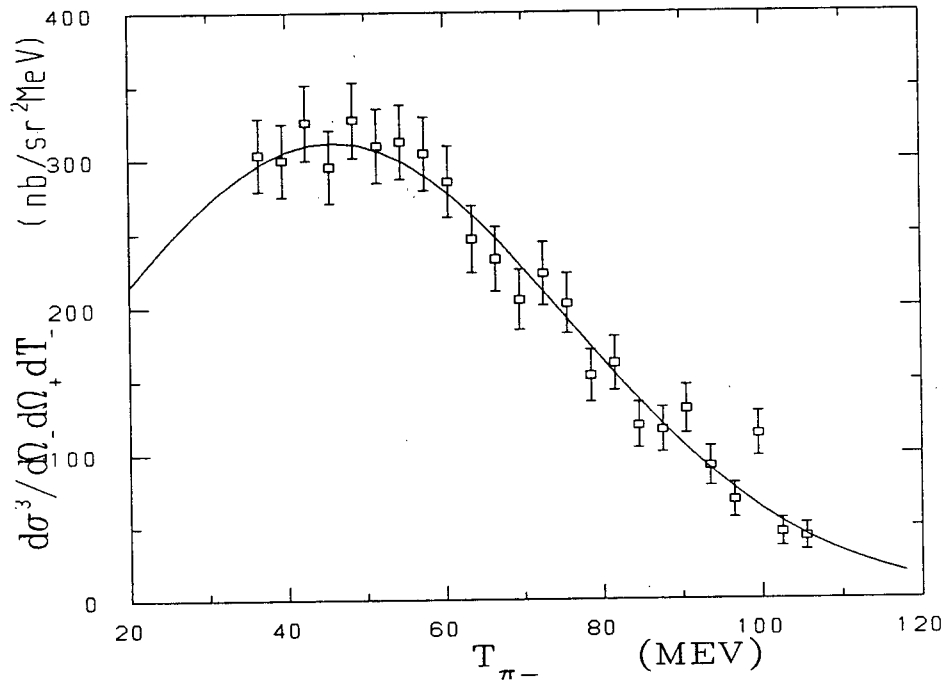


Figure 25: The measured energy distribution of π^- in the QCD at 50° . The curve represents the fitted polynomial. Data point errors are statistical.

completed the energy integrations, the angular distribution is a double differential cross section. As done for the case of the π^- energy fitting, it is assumed here that the shape of the angular distribution is not appreciably affected by the missing portions of the energy phase-space. The CARUZ covered the angular range of $22.5^\circ - 127.5^\circ$ in two steps as shown by the distributions in Figure 26. As the angular integration has a $\sin \theta$ behaviour, the CARUZ has covered the most important part of the in-plane angular distribution of the π^+ . This results in a relatively small uncertainty in the angular integration. For the out-of-plane contribution, it is assumed that pion pairs are isotropically distributed, contributing a factor of 2π , an assumption supported by the model of [OV86]. The double differential cross section is fit using a Legendre polynomial in the form

$$\frac{d^2\sigma}{d\Omega_{\pi^-}d\Omega_{\pi^+}}(\theta_{\pi^+}) = \left\{ \sum_{i=0}^n a_i P_i(\cos \theta_{\pi^+}) \right\}^2.$$

The order of the polynomials taken was allowed to vary to obtain the best fit and $n = 2$ was found to be sufficient to describe the data. The fitted distribution is integrated numerically. For the $\theta_{\pi^-} = 115^\circ$ data, the integration is halted at 120° as the spectrum has fallen to zero. The error contribution of the angular fit is estimated to be 3% from the variation in integrated area for different orders of polynomial.

The data is now reduced to the single differential cross sections in the π^- angle at three different angle settings, as listed in Table VII, which limits a Legendre polynomial fit to $n = 1$. The differential cross sections and fit are shown in Figure 27. The total cross section is then found from the numerical integration of the fitted curve and is found to be, including all errors,

$$\sigma_{TOT} = 2.25 \pm 0.35 \text{ mb}.$$

The contributions to the error can be separated into factors contributing to the overall uncertainty of the measurement, such as solid angle uncertainty, and

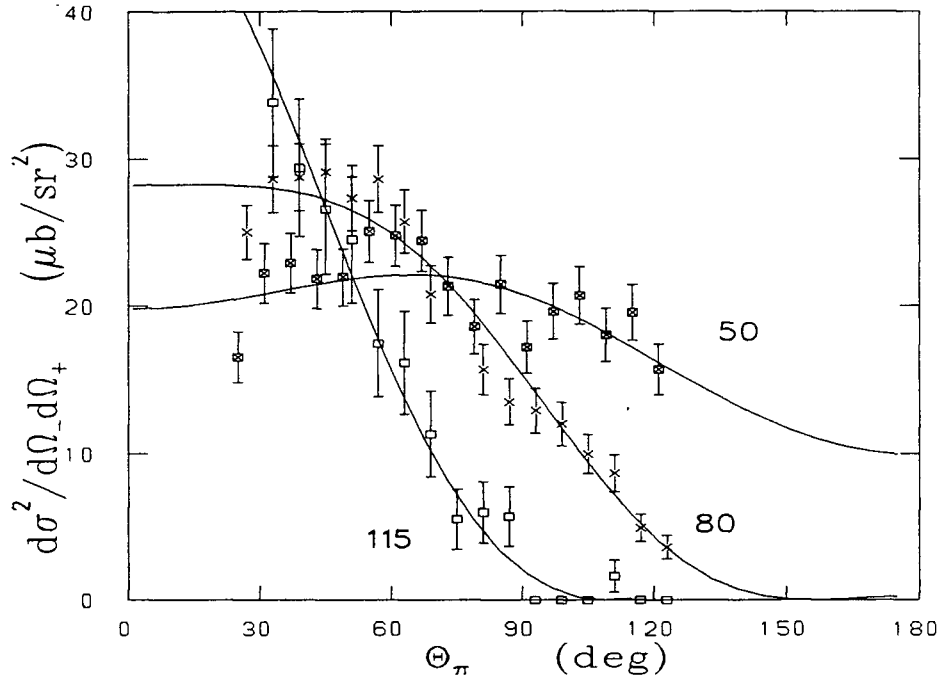


Figure 26: The angular distribution of π^+ in the CARUZ for the QCD at each of the three settings with the fitted Legendre polynomial series to extrapolate to undetected portions of the angular phase space.

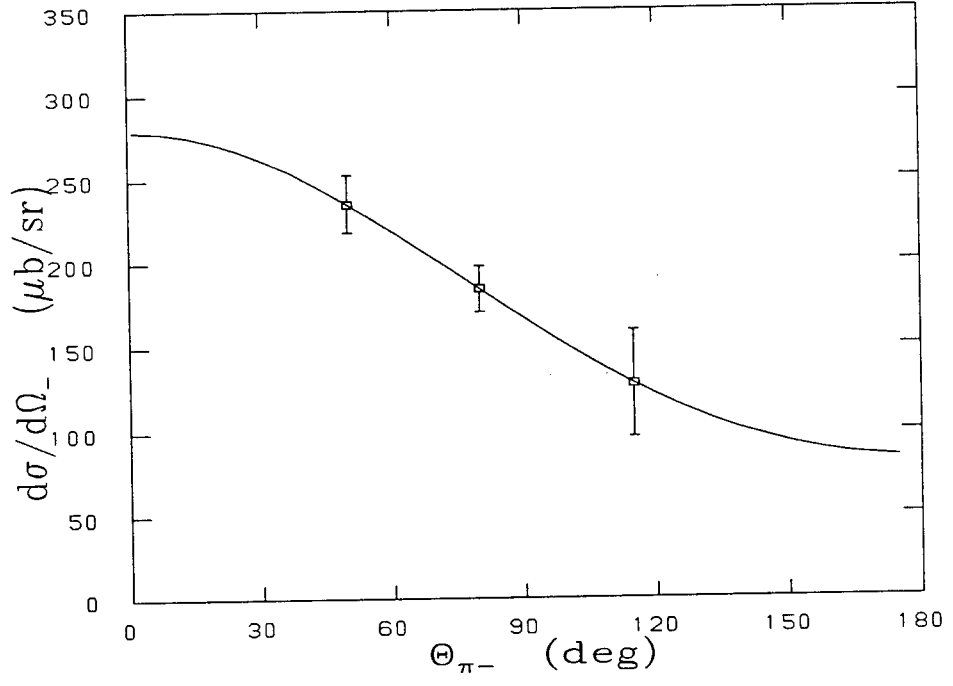


Figure 27: The angular distribution of π^- for the different QCD angular settings used in the experiment with the fitted Legendre polynomial series.

QQD Angle	$\frac{d\sigma}{d\Omega_{\pi^-}}$ ($\mu b/sr$)	Error ($\mu b/sr$)
50	235.4	17.1
80	184.3	13.7
115	125.3	31.1

Table VII: The single differential cross sections as a function of the angle of the π^- and the corresponding error. The error includes statistical errors as well as errors from the previous extrapolations.

errors specific to each measured configuration, such as the extrapolation errors. For purposes of the extrapolations, it is unnecessary to consider the normalization errors as they will not affect the accuracy of the extrapolation. The errors associated with the energy integrations are given in Table VI while all other errors are summarized in Table VIII

The main contributions to the experimental error comes from the error of the QQD solid angle, $\Delta\Omega_{\pi^+}$. The accuracy of the solid angle determination (see section III.1.2.2) is approximately 9% simply due to the error present in the literature cross sections. An additional contribution to the solid angle error of 7% is added to take into account the differences in the determination of the momentum acceptance from the 1986 QQD calibration data and the 1987 QQD calibration data taken as part of each experimental run.

The error quoted for the uncertainty in CARUZ solid angle arises from estimates of effective distance from the target to S2. The π decay error results from the uncertainty in modelling the π^+ decay detection efficiency. Any uncertainty in the decay fraction of the π^- is effectively absorbed into the QQD momentum acceptance determination. The N_{tgt} error accounts for the uncertainty in the target area and errors in target alignment with respect to the beam. The PCOS and hodoscope flux errors have been discussed before. The hodoscope error

Quantity	Percentage Error
Flux:	
Hodoscope	5.
PCOS	2.
N_{tgt}	4.
WC efficiency	2.
π decay	2.5
$\Delta\Omega_{\pi+}$	2.
$\Delta\Omega_{\pi-}$	11.5
Integrated statistics	
50°	2.6
80°	3.2
115°	6.7
Normalization errors	
50°	13.6
80°	12.8
115°	12.8

Table VIII: Errors present in the $(\pi, 2\pi)$ experiment, given in percentages.

applies to the data with the QQD at 50° and one of the 80° settings (high QQD momenta, low CARUZ angles). The PCOS error applies to all other data.

The error on the total cross section is determined in the following manner. The single differential cross section errors are taken to be the sum in quadrature of the statistical errors and the errors of the three extrapolations performed to reach the single differential cross sections. The weighted average of the errors for the three θ_{π^-} points is then summed, again in quadrature, with all the remaining errors to yield the relative error of the total cross section. As already mentioned, the QQD momentum acceptance error dominates all other errors in the final calculation. The large uncertainty in the 115° data has only a small effect on the determined cross section and error.

III.2.3 Contribution of Backgrounds

The discussion of errors in the previous section has not taken into account the possible contribution to the cross section from unwanted backgrounds. Any such contributions are believed to be small and are thus not considered in the error. To demonstrate this assumption, several possible background sources are considered here.

The removal of electrons in the QQD spectrum was accomplished through the cut in the TOF spectra shown in Figure 17. It is seen that the $e^- - \pi^-$ separation is very good, even in the “worst” case shown, although not complete. It is possible that a fraction of the electrons will contaminate the selected π^- ’s and that some π^- ’s leak out of the cut. However, from Figure 17, this fraction can be seen to be quite small. Note that most of the background in Figure 17 arises from random π -p coincidences and thus are not accepted as $(\pi, 2\pi)$ events and that this background only occurs in the data with the QQD at 50° and the CARUZ at -50° . Where this background is not present, the $e^- - \pi^-$ separation is

better than shown so that any possible electron contamination is further reduced.

The CARUZ accomplished the removal of e^+ 's and protons through the use of the measured CARUZ TOF, E and ΔE . The $e^+ - \pi^+$ separation was shown in Figure 19 to be very clear with little ambiguity. Experimentally, the number of detected e^+ 's was found to be small in comparison to the number of pions present, so that contamination from them could be ignored. The detected protons outnumbered the detected pions. However, the spectrum of Figure 21 shows that the protons are clearly separated from the pions and pose little background threat when proper cuts are applied.

The ^{16}O was used in the form of a gelled water target with some thin capton and aluminum foil windows. The hydrogen present can not contribute to the $(\pi^+, \pi^+\pi^-)$ reaction. The carbon and aluminum in the windows can, however. The empty target data taken was not of sufficient statistics to allow a reliable subtraction of their contributions. The window thickness amounts to 17 mg/cm^2 compared to 541 mg/cm^2 for the ^{16}O , about 3% of the thickness. Even if we take the $(\pi^+, \pi^+\pi^-)$ cross sections to be of the same magnitude on carbon and aluminum as on the oxygen, the net effect on the cross section will be at most of order 3%, small compared to the overall error.

The last possibility considered here is the possibility of random coincidences from multiple pions in a beam burst, where one pion has undergone a DCX reaction and the other a inelastic collision with substantial energy loss. The probability of a pion undergoing a reaction, R , while it traverses the target is

$$P_R = N_{tgt} \cdot \sigma_R.$$

For the $(\pi^+, \pi^+\pi^-)$ reaction, $P \simeq 4.6 \cdot 10^{-5}$. For the random coincidence, the DCX cross section (at 80° at 270 MeV) is taken from [Woo84] to be

$$\frac{d^2\sigma}{d\Omega_{\pi^-} dT_{\pi^-}} \simeq 3.0 \mu\text{b/sr}$$

and the inelastic cross section is taken from [MBG*80] as (at 35° and 240 MeV)

$$\frac{d^2\sigma}{d\Omega_{\pi^+}dT_{\pi^+}} \simeq 50.0\mu b/sr.$$

The cross sections for the DCX and inelastic reactions are fairly flat for $T_\pi < 100$ MeV. Taking $\Delta E_{\pi^+} = 60$ MeV and $\Delta E_{\pi^-} = 110$ MeV and using 4π for the angular integral, the two resulting probabilities are multiplied together to give a probability of $P \simeq 0.65 \cdot 10^{-7}$ for the random coincidence, much less than 1% of the measured probability, and is thus ignored.

Chapter IV

Theoretical Approaches and Simulations

In Chapter 1, an introduction to the $(\pi, 2\pi)$ process was given with an emphasis placed on the theoretical modelling of the free reaction. The importance of the PCAC hypothesis in modelling the free reaction was mentioned as well as the contribution of the symmetry breaking term, ξ . In this chapter, the details of the approaches used to calculate the $A(\pi, 2\pi)$ reaction will be examined.

Approximations, where made, in the form of the free reaction mechanism description chosen for each approach, are covered in section IV.1. The formalisms for the extension of the calculation to the nuclear reaction also contain approximations and are covered in section IV.2. The validity of the approximations at the different levels in the calculation will be examined.

Available theoretical results for the total cross section calculations will be compared to each other and to the result from section III.2.2. The results of Oset and Vicente-Vacas [OV85,OV86,OV87] will be examined in the most detail.

Lastly, in section IV.3, some details of the Monte Carlo simulations used to attempt to describe some of the features of the experimental data will be discussed. Note that the theoretical formalisms presented here are taken from the cited publications and are not the work of the author.

IV.1 The Free $(\pi, 2\pi)$ Reaction

If the free pion production mechanism is assumed to dominate the $(\pi, 2\pi)$ reaction in nuclei then, obviously, any calculation of the $A(\pi, 2\pi)$ reaction must contain a

reasonable description of the free process. The model implied by the \mathcal{L}_{eff} of Chapter 1 and the one-, two- and three-point diagrams of Figure 1 should be the essential starting point for a calculation. It is quite common to neglect some terms in the calculation and assume dominance of say, the pion pole term alone, or the pion pole plus contact term as these are the only terms of Figure 1 which have surviving contributions at threshold. In addition, most authors make some sort of threshold approximation in calculating the cross section. That is, in the formula for the cross section, some of the kinematical quantities, such as particle momenta and energies, are approximated by their values at the reaction threshold. Bhaleroa and Liu [BL84] have pointed out however, that once such approximations are made, most of the dynamical content of the calculation is lost and the results simply become proportional to the phase space governing the reaction. Thus one loses, for example, information regarding angular correlations between final state particles. In most cases where a threshold approximation was made, the authors were primarily interested in calculating the total cross section, so that dynamical content was of little importance. It is also noted in [BL84] that even if all the diagrams of Figure 1 are used to calculate the $p(\pi^-, \pi^+\pi^-)$ reaction, the results are more than a factor of two below the data, even close to threshold. It is then apparent that, by itself, the standard Weinberg effective Lagrangian is not adequate to describe the free process. This fact must be kept in mind when one considers the reaction in the nucleus. For the following discussion, the momenta labelling for the particles in the reaction is shown in Figure 28.

The model of Cohen and Eisenberg [CE83] uses the one- and two-point diagrams of the effective Lagrangian, leaving out the magnetic moment term (which is small). For the numerical constants f_π and g_A/g_V , the values 82 MeV and 1.25 are used. The T-matrix amplitude is written in a non-relativistic form

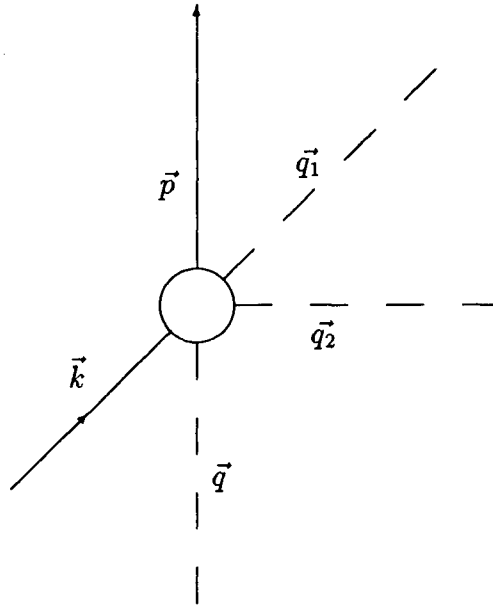


Figure 28: Schematic representation of the $(\pi, 2\pi)$ reaction indicating the labelling for the particle momenta. The circular region contains the mechanisms described by the various forms of effective Lagrangians. The pions are shown as dashed lines, while the nucleons are shown as full lines.

for use in a nuclear calculation, that is, a term such as

$$\gamma_\mu \gamma_5 \vec{\tau} \cdot (\partial^\mu \vec{\phi})$$

becomes

$$\sigma_i (\partial^i \vec{\phi}) \vec{\tau}.$$

Such terms are referred to as $\vec{\sigma} \cdot \vec{q}$ terms, the \vec{q} arising from the derivative of the pion field (often this term is called $\vec{\sigma} \cdot \vec{k}$ in literature with the \vec{k} referring to the pion, not the nucleon). In the evaluation of the T-matrix describing these diagrams, the threshold form of the center of mass amplitude is evaluated in the laboratory frame. As a results of these approximations, the calculated cross sections for the $p(\pi^-, \pi^+ \pi^-)$ reaction are as much as a factor of 10 low in the energy region of interest [BL84].

The calculation of Rockmore [Roc83], for the $(\pi^+, 2\pi^+)$ reaction, or equivalently, the $(\pi^-, 2\pi^-)$ reaction, employs the one-point pion pole term alone. A threshold approximation is used to simplify the form of the amplitude. The form of the approximation used will be discussed below in section IV.2 in relation to the cross section formula. The approximations made are consistent with the object of calculating the cross section near threshold for the $A(\pi^+, 2\pi^+)$ reaction. The pion pole term by itself predicts the free $p(\pi^+, 2\pi^+)$ reaction reasonably well, but underpredicts the free $p(\pi^-, \pi^+ \pi^-)$ reaction by a factor of two to three at 280 MeV [BL84]. Inclusion of the pion contact term tends to cancel the pole term, reducing the cross section by roughly a factor of two. Rockmore published an earlier paper examining the $A(\pi, 2\pi)$ process [Roc75] using the pion pole and contact terms in the elementary description. These earlier results will not be examined in detail, except to note that in this paper, an estimate is made for the contribution of one diagram containing the N^* isobar in the intermediate state. The contribution is estimated for this N^* diagram to be less than 10% of the size

of the pole term. Rockmore [Roc84] has also made an estimate of the direct two nucleon contribution to the $(\pi, 2\pi)$ reaction on the deuteron and found such effects to be very small.

As mentioned earlier, the full Weinberg Lagrangian is incapable of reproducing the measured $p(\pi^-, \pi^+\pi^-)$ cross section. With this in mind, Oset and Vicente-Vacas [OV85] modified the form of \mathcal{L}_{eff} to make it more consistent with the known phenomenology of the πN interaction. This was done by introducing terms that describe the presence of isobars in the intermediate state. Some of the additional diagrams used in [OV85] are illustrated in Figure 29, from the total of 32 diagrams used in this calculation.

The model used to describe the free $(\pi, 2\pi)$ process developed in [OV85] still has difficulties describing the cross section above threshold, supplying about 60% of the measured cross section at 280 MeV. To ensure that the free process is properly described as far as the cross section magnitude, a more phenomenological approach to describing the free reaction is taken in [OV86], avoiding the need to evaluate a large number of diagrams. Since all the surviving threshold terms have a $\vec{\sigma} \cdot \vec{q}$ dependence, and are generally the more important terms at higher energies, the free amplitude is scaled according to

$$T^{free} = iB \left[1 + a \frac{T_\pi - T_\pi^{th}}{T_\pi^{th}} \right] \vec{\sigma} \cdot \vec{q}$$

where \vec{q} is evaluated at the lab momenta, T_π^{th} is the threshold production energy in the πN lab system and T_π is the lab kinetic energy. The parameters a and B are fit to experimental data [Man81] to reproduce the measured total cross section.

IV.2 $(\pi, 2\pi)$ as a Nuclear Probe

The $(\pi, 2\pi)$ reaction has been proposed as a possible reaction to probe the spin-isospin strength distribution in nuclei, or the pion condensation precursor

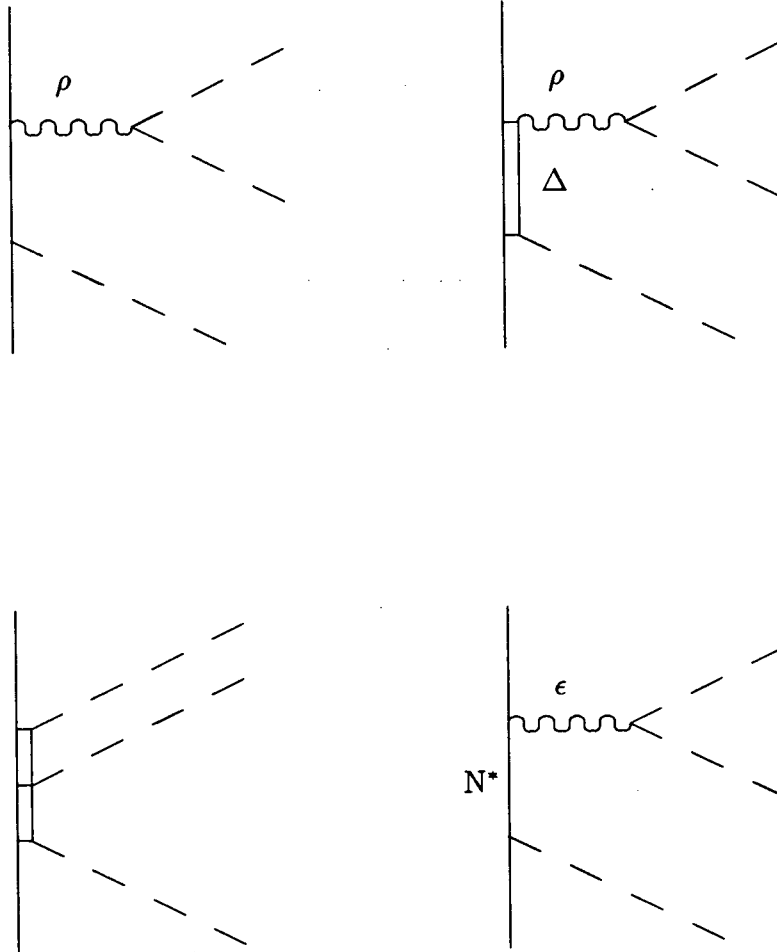


Figure 29: Some of the 32 additional diagrams used in the model of [OV85] showing contributions due to the Δ , ρ , ϵ and N^* intermediate states.

phenomena, and also as a means of selectively exciting nuclear levels with pion-like quantum numbers ($J^\pi = 0^-, 1^+, 2^-, \dots; T = 1$) [Eis80,CE83]. The exclusive measurement of selected levels would require a combined resolution of better than 1 MeV and the predicted cross sections are so small as to make the reaction unmeasurable. If precursor phenomena exist, they could produce observable effects in the inclusive measurement of the total cross section for the $(\pi, 2\pi)$ reaction in the energy region close to threshold, precisely the region investigated here, where the momentum transfer is in the range $2-3 m_\pi$.

The pionic field of frequency ω and momentum \vec{q} can polarize the nuclear medium through nucleon-hole and Δ -hole excitations as depicted in Figure 30. These contributions to the pion self-energy, through iterations of the particle-hole excitations to all orders, are treated by Cohen and Eisenberg [CE83] by renormalizing the entire production amplitude in the manner

$$[\vec{\sigma} \cdot \vec{q} \tau_\mu]_{renormalized} = \varepsilon^{-1}(q, \omega) \vec{\sigma} \cdot \vec{q} \tau_\mu.$$

The diamagnetic function, $\varepsilon(q, \omega)$, can be expressed in terms of Lindhard functions [FW71], the one pion propagator and the Migdal parameter g' . A value of g' of 0.4 corresponds to the case where pion condensation exists in the nucleus, while $g' = 0.7$ corresponds to a minimal condensation effect. The Migdal parameter is equivalent to the Lorentz-Lorenz parameter, λ , used to describe nuclear correlation effects in low energy pion elastic scattering. Numerically, the equivalence is given by $g' = \lambda/3$. The currently accepted range for g' is 0.6-0.7.

For high momentum transfer, but low energy transfer, the diamagnetic function can be written as

$$\varepsilon(q, 0) = 1 + W(q, 0)U(q, 0)$$

where

$$W(q, \omega) = \frac{q^2}{\omega^2 - q^2 - m_\pi^2} + g'$$

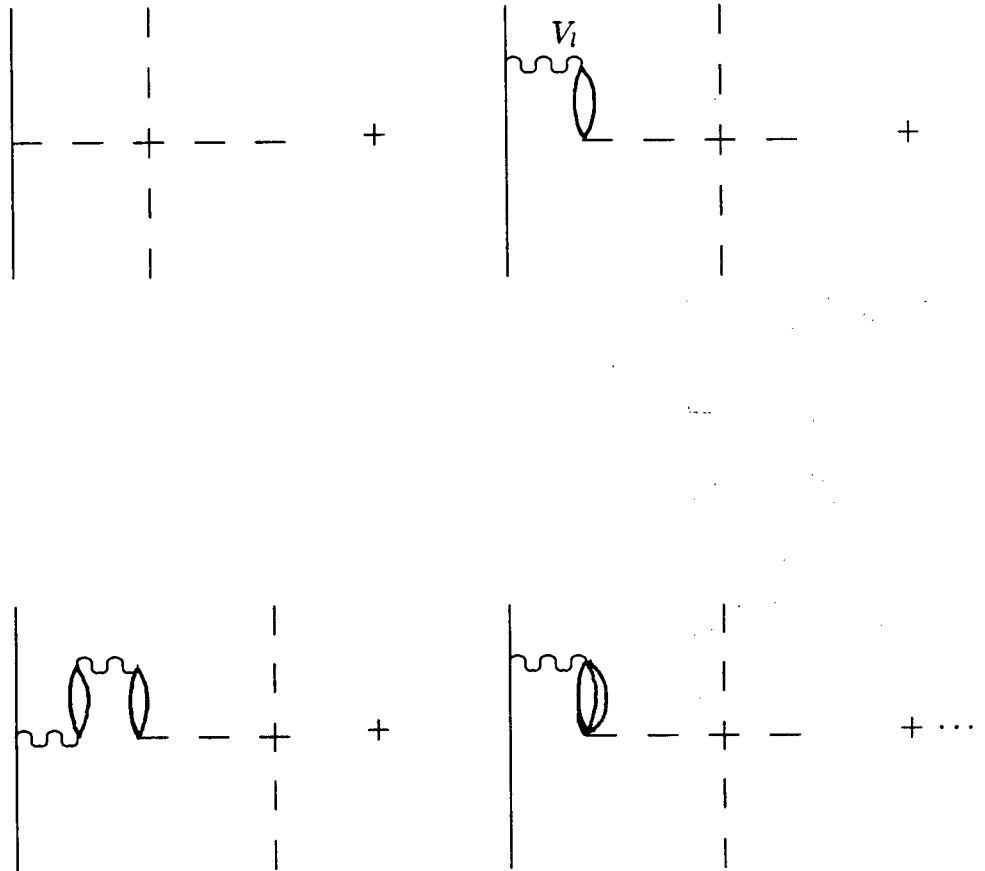


Figure 30: A diagrammatic representation of nucleon-hole and Δ -hole excitations in the nuclear medium contributing to the pion self-energy.

is the pion polarization propagator describing the longitudinal part of the spin-isospin nuclear interaction. The Lindhard function is written as

$$U(q, \omega) = \frac{f^2(q^2)}{m_\pi^2} [U_N(q, \omega) + 4U_\Delta(q, \omega)]$$

where $f^2(q^2)$ is the monopole form factor multiplied by the coupling $f^2/4\pi = 0.08$ given by

$$f^2(q^2) = \left(\frac{\Lambda^2 - m_\pi^2}{\Lambda^2 + q^2} \right)^2 f^2.$$

The cutoff Λ is taken to be 1000 MeV/c. The factor of 4 multiplying the Δ Lindhard function is the square of the ratio of nucleon to Δ coupling constants as given by Chew-Low theory. The nucleon Lindhard function can be written as

$$U_N(q, \omega) = \frac{m^* p_F}{\pi^2} \left\{ 1 + \frac{p_F}{2q} (1 - y_+^2) \ln \left| \frac{1 + y_+}{1 - y_+} \right| - \frac{p_F}{2q} (1 - y_-^2) \ln \left| \frac{1 + y_-}{1 - y_-} \right| \right\}$$

and the Δ Lindhard function as

$$U_\Delta(q, \omega) = \frac{8}{9} \frac{\omega_\Delta}{\omega_\Delta^2 - \omega^2} A \rho.$$

The arguments in the functions are

$$y_\pm = \frac{m^*}{p_F} \frac{\omega \pm \frac{q^2}{2m^*}}{q},$$

$$\omega_\Delta = m_\Delta - m_N = 2.2m_\pi.$$

The effective nucleon mass, m^* , is taken as $0.8m_N$, p_F is the Fermi momentum, ρ is the matter density normalized to one and A is the atomic weight of the nucleus under consideration. The local Fermi momentum is determined by

$$p_F = \left(\frac{3}{2} \pi^2 A \rho(r) \right)^{1/3}$$

where the nuclear density form taken is the two parameter Fermi form

$$\rho(r) = \frac{3}{4\pi c^3} \left\{ \left(1 + \frac{\pi^2 t^2}{c^2} \right) \left[1 + \exp \left(\frac{r - c}{t} \right) \right] \right\}^{-1}$$

with c the half density radius and $4t \ln 3$ is the 10% to 90% density distance.

The $(\pi, 2\pi)$ reaction will produce a wide range of excited states in the residual nucleus. To reduce the calculational difficulty, a closure approximation is used by [CE83] to truncate the possible Fermi gas states of the residual nucleus. To do this, a mean nuclear excitation must be chosen and this energy can then be taken outside of the integrals required to evaluate the cross section. Assuming a quasi-free peak contribution dominates the cross section, the closure energy is taken to be

$$\bar{\epsilon} = \frac{Q^2}{2m_N}$$

where $Q \sim q$ is taken as the average momentum transfer. A correction term measuring the error of the closure approximation was estimated and found to be small above 500 MeV/c but at 400 MeV/c (284 MeV), the calculated sample values of [CE83] indicate that it is roughly 50% of the size of the closure term. The correction term becomes even larger for lower momenta.

The cross section calculation is expanded into partial waves for the three pions. A form of the local density approximation (LDA) is used to evaluate the diamesic function through the nuclear volume. That is, it is evaluated for the local Fermi momentum calculated from the local density. This assumes that the nuclear density is varying slowly enough so that it is meaningful to assign a local Fermi momentum.

The pion waves are distorted in the calculation of [CE83] using the computer code DWPI [EM76] to calculate the distorted partial waves. For the incoming wave, optical distortion (quasi-elastic scattering) as well as true absorption (proportional to ρ^2) are used. For the outgoing channel, Coulomb distortion and true absorption are used. The optical distortion in the final state reduces the pion energy but does not eliminate it, so it is not included in the final state. The

optical potential parameters used to evaluate the distortions are taken from [SMC79]. For pion momenta less than 50 MeV/c, the pionic atom parameters are used while for momenta from 50-130 MeV/c, the Set 1 parameters are used. For higher momenta, the optical potential parameters are extrapolated from the Set 1 values following a prescription from [SMC79].

The cross section is obtained after numerically integrating over the partial waves for all three pions. In order to reduce the computation time, some approximations are made in the integration by estimated average values for some variables for which the matrix element depends only weakly upon. Results from the calculation for the $^{16}\text{O}(\pi^+, \pi^+ \pi^-)$ reaction are shown in Figure 31, as x's, for the values of g' of 0.40, 0.55 and 0.70, where the larger cross sections correspond to smaller g' values. The results for $^{16}\text{O}(\pi^+, 2\pi^+)$ reaction are found to be about 20% larger than the values for $^{16}\text{O}(\pi^+, \pi^+ \pi^-)$. However, a factor of $\frac{1}{2}$ has been omitted in the calculation that accounts for the identity of the π^+ 's in the final state so that the $(\pi^+, 2\pi^+)$ cross sections quoted are a factor of two too large. It should be noted that the cross sections calculated for low g' already exceed the inclusive DCX cross section measured at 270 MeV [Woo84] and can thus be ruled out.

Several comments can be made concerning calculations of [CE83]. Cohen and Eisenberg point out that the closure approximation introduces into the cross section calculation terms corresponding to the single nucleon contribution and to a two nucleon spin-isospin correlation contribution, the latter of which is left out of the calculation. This two nucleon term is distinct from direct two nucleon mechanisms which would have their own T-matrix contributions in the calculation. The correlation term is examined by [CE83] and estimated to be roughly 10% the size of the single nucleon contribution. Also, the choice of the closure energy is not unique. The quasi-free peak has a large width, and different choices of the closure energy can shift the cross section up to 30%. This uncertainty is what is used in

[CE83] for a measure of the error in the calculation. The closure approximation is apparently inappropriate for low incoming pion energies as shown by the size of the correction term, however the threshold approximation chosen to model the underlying free process becomes worse as energy increases. If we empirically try to compensate the calculation for underestimating the free reaction, the calculated results only become larger, becoming uncomfortably high.

Another estimate of the $(\pi, 2\pi)$ process is given by [Roc83] for the $^{18}\text{O}(\pi^-, 2\pi^-)$ which, with some assumptions, we can relate to the $^{16}\text{O}(\pi^+, \pi^+\pi^-)$ process. Rockmore uses a Fermi gas description of the nucleus which allows a convenient way to sum over the final nuclear states and avoids tedious details of the nuclear structure. The approach was motivated by earlier applications to the threshold pion electroproduction process in nuclei [CW64]. The forms of the threshold approximation taken by Rockmore allow the phase-space calculation to be viewed as a Fermi averaging over phase-space rather than an integration over a response function requiring a lengthy Monte Carlo process. Approaching the problem in this manner allows Rockmore to relate the emission of two pions as encountered in the $(\pi, 2\pi)$ process to one pion emission as found in the electroproduction process.

The one-body pion pole term is chosen as input into the Fermi gas model. Rockmore makes the threshold approximations

$$\frac{1}{\omega_1\omega_2} \simeq \frac{1}{m_\pi^2}$$

and

$$\omega_1 + \omega_2 \simeq 2m_\pi + \frac{q_1^2 + q_2^2}{2m_\pi}.$$

The cross section can then be written as

$$\sigma(\pi, 2\pi) \simeq \frac{q}{8}\Omega \left(\frac{1}{f_\pi}\right)^6 \left(\frac{g_A}{g_V}\right)^2 \left(\frac{m_\pi}{\omega_0 - m_\pi}\right)^2 \frac{1}{(2\pi)^8} I(\eta)$$

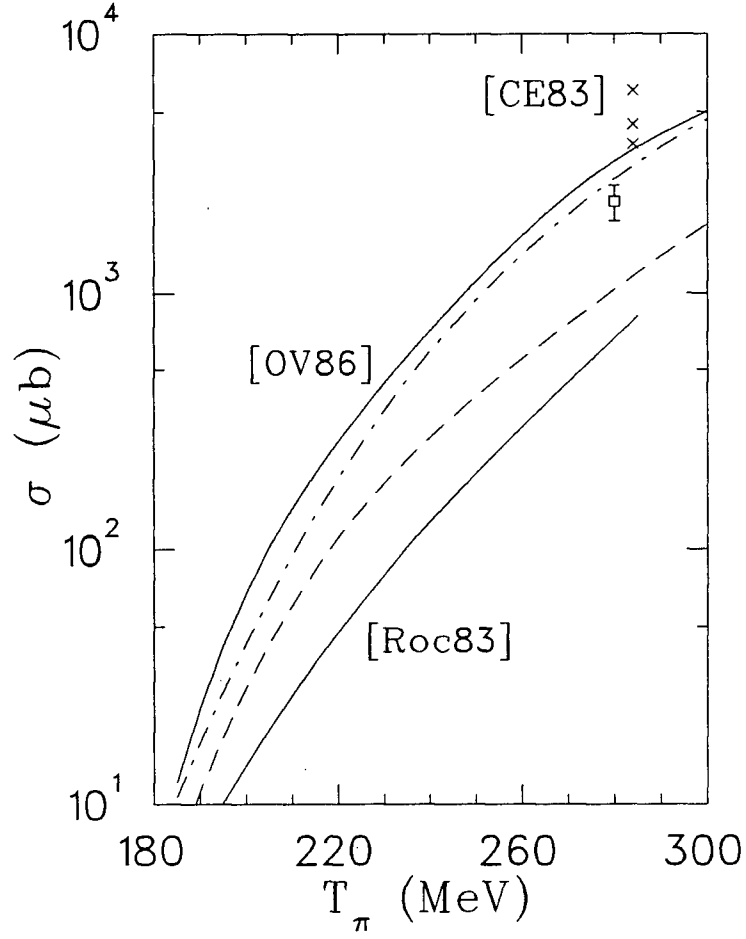


Figure 31: Predictions for the $^{16}\text{O}(\pi^+, \pi^+\pi^-)$ reaction by the three authors discussed above compared to the experimentally evaluated total cross section. Note that the Rockmore curve (lower solid curve) contains the corrections discussed in the text. The square point is the measured datum.

where

$$I(\eta) \cong \int \frac{d\vec{k} d\vec{q}_1 d\vec{q}_2}{m_\pi^2} \delta \left(\frac{(\vec{k} + \vec{q} - \vec{q}_1 - \vec{q}_2)^2}{2m^*} - \frac{\vec{k}^2}{2m^*} - \eta m_\pi + \frac{q_1^2 + q_2^2}{2m_\pi} \right) \theta(|\vec{k} + \vec{q} - \vec{q}_1 - \vec{q}_2| - p_F) \theta(p_F - k).$$

The nuclear size is described by

$$\Omega = A \left(\frac{4\pi r_0^3}{3} \right),$$

which represents a hard sphere nucleus of radius $A^{1/3}r_0$ with $r_0 = 1.2$ fm. The effective nucleon mass, m^* , is taken as $0.6m_N$ and

$$\eta = \frac{\omega_q - 2m_\pi}{m_\pi}$$

With the additional threshold approximation of

$$\vec{k} + \vec{q} - \vec{q}_1 - \vec{q}_2 \simeq \vec{k} + \vec{q},$$

the Fermi averaging is carried out and Rockmore obtains

$$I(\eta) \simeq \frac{2\pi^4}{3q} m^{*2} m_\pi^5 \eta^4.$$

The approach used for the calculation has limits of validity placed on it by the conditions $q < 2p_F$ with $p_F \simeq 260$ MeV/c and

$$\eta < \frac{q}{2m^*m_\pi} (2p_F - q).$$

These conditions mean that Rockmore's calculational method is only valid for incident pion energies of less than 200 MeV, that is, those energies just above threshold. For purposes of display, Rockmore extended the calculation beyond this region up to 280 MeV, our energy of interest.

The effects of distortions have not yet been included in the calculation. An eikonal approach is used for distorting the incident pion wave in the form

$$\psi_{\vec{q}}(\vec{r}; \pi^\pm) = e^{i\vec{q} \cdot \vec{r}} \exp \left[\frac{i2\pi A}{q} \bar{f}_0^\pm \int_{-\infty}^z \rho(\vec{b}, \xi) d\xi \right]$$

where \vec{b} is the impact parameter for an incident pion with momentum \vec{q} and the density, ρ , is taken as a hard sphere with the same radii for protons and neutrons. \bar{f}_0^\pm is the averaged forward $\pi^\pm N$ scattering amplitude. Rockmore then evaluates the attenuation effect of the distortion and corrects the undistorted cross section calculation result. In the hard sphere nuclear model, he finds that the cross section is reduced by a factor of 10 from the undistorted results. Rockmore's results for $^{18}\text{O}(\pi^-, 2\pi^-)$ are substantially lower than the results of [CE83] for $^{16}\text{O}(\pi^+, 2\pi^+)$. One would expect the results to be similar if both calculations are valid.

The purpose of Rockmore's calculation was to evaluate the cross section close to threshold. However, we would like to try to compare his result to the data produced here. To accomplish this, several corrections will be estimated for the results of Rockmore. Assuming that the nuclear cross sections will scale the same as the free cross sections, the Rockmore result is scaled by the ratio of the experimental cross sections

$$\frac{p(\pi^-, \pi^+ \pi^-) n}{p(\pi^+, 2\pi^+) n}$$

which is approximately 7-10 in the energy range we are interested in. Any effects resulting from the different thresholds for the $^{18}\text{O}(\pi^-, 2\pi^-)$ and $^{16}\text{O}(\pi^+, \pi^+ \pi^-)$ reactions are ignored and it is assumed that the cross sections for the reactions $(\pi^-, 2\pi^-)$ and $(\pi^+, 2\pi^+)$ are identical. ^{16}O has eight neutrons compared to the ten in ^{18}O , so the results are scaled by an additional 0.8. The hard sphere overestimates the absorption effects, which are essentially proportional to ρ^2 , while the single nucleon reaction mechanism is proportional to ρ and will be enhanced relative to absorption on a diffuse nuclear exterior. Rockmore also does not include final state absorption. The correction for these two absorption effects is estimated to give approximately a factor of three increase in the cross section (this estimate is based upon the the reduction in cross section from the free cross section

observed in the basic calculation of [OV86]). With these correction estimates, the results are shown in Figure 31 as the lower solid line and, as expected, are seen to be roughly equivalent to, although somewhat below, the results of [OV86] when no binding enhancement is included (Oset's results are discussed below).

The most detailed calculations available for the $A(\pi, 2\pi)$ reaction are those of Oset and Vicente-Vacas [OV86,OV87] which include published total cross section calculations as well as yet unpublished differential cross section results. With the disagreements between results of the earlier calculations discussed above kept in mind, [OV86] attempt to set out a description of the reaction that avoids, where possible or practical, some of the difficulties of the earlier models. The phenomenology of pion-nucleon and pion-nucleus reactions are used as input to model the stages involved in the calculation.

The amplitude taken for the the free process is the phenomenological form given earlier. This at least guarantees that the free cross section is adequately described as far as magnitude. The amplitude describing the free $(\pi, 2\pi)$ process will be renormalized inside nuclear matter. The effects of the nuclear medium will change the vertices, the propagators and the external particle lines. The πNN vertex in the nuclear medium is expected to change by less than 5% from the free vertex [OW76] and so the change is ignored. Other vertices are not expected to have any larger corrections. The hadronic propagators can be changed up to 20-30% [OTW82]. This change is considered to be small in [OV86] and ignored there. The only substantial effect then is the renormalization of the pionic propagators which is expected to be large due to the strong πN interaction and the low mass of the pion. The renormalization of the virtual pions is the origin of the proposed precursor effect. The only diagram of the Weinberg Lagrangian containing a virtual pion is the pion pole diagram of Figure 1. The renormalization procedure used by [OV86] is similar to that of [CE83], however,

there are some small differences in the formulation which are worth noting. The longitudinal part of the spin-isospin interaction is written as

$$V_l(q) = \frac{f^2}{m_\pi^2} \left(F^2(q) \frac{q^2}{q^2 - m_\pi^2} + g' \right).$$

The form factor F is the same monopole form as before with the cutoff 1.2 GeV/c, but it only multiplies the pion propagator and not g' . The Migdal parameter is set to 0.6. The Lindhard functions are the same form as for [CE83].

The pion pole term is the only term affected by the renormalization. Thus, that term alone should be renormalized, not the entire amplitude as done in [CE83]. Oset and Vicente-Vacas then write the T-matrix amplitude in the medium as

$$\tilde{T} \simeq T^{free} - T^{1,p} + \tilde{T}^{1,p}$$

with T^{free} being the amplitude for the free $(\pi, 2\pi)$ process, $T^{1,p}$ is the pion pole amplitude and $\tilde{T}^{1,p}$ is the renormalized pion pole amplitude

$$\tilde{T}^{1,p} = T^{1,p} \epsilon^{-1}$$

with ϵ the diamesic function. The production amplitude is modelled by the phenomenological scaled form discussed earlier. The pole part of the amplitude that is replaced is unscaled so that its contribution is not overestimated. It should be noted that as a result of the parameterization chosen for the amplitude, the only kinematic dependences present in the calculation are the $\vec{\sigma} \cdot \vec{q}$ form of the basic amplitude and the kinematic dependences in the pion pole term.

The reaction cross section is calculated by making use of the optical theorem in the form

$$\sigma = \frac{-1}{q} \int d^3r \text{Im} \Pi(q)$$

where $\Pi(q)$ is the piece of the optical potential for the diagram shown in Figure 32 for an infinite Fermi sea. The local density approximation is then made by

evaluating $\Pi(q)$ for the local value of the nuclear density in the integration over the nuclear volume. The formulation of $\Pi(q)$ will be given below. It can be written in terms of the T-matrix, the nucleon Fermi sea occupation numbers and particle propagators.

Before writing the cross section formula, the effects of absorption will be considered. Absorption effects (distortion of the pion waves) are obtained using an eikonal approximation. For the incoming pions, the optical (quasi-elastic) and true absorption are included. When a pion quasi-elastically scatters in the nucleus, it loses on average about 1/3 of its energy. As the free $(\pi, 2\pi)$ cross section decreases very rapidly as energy drops, a pion that has lost 1/3 of its energy has a negligible probability of undergoing a production reaction and thus can be discarded. For outgoing pions, quasi-elastic scattering will only change the pion's energy (and angle), not remove it from the outgoing flux, so that the pion can still be detected. Thus, the optical terms are not included by [OV86] for final state losses.

The Δ resonance can be considered to dominate the absorption for the incident pions, thus a Δ -hole phenomenology can be applied. The probability per unit length for quasi-elastic processes can be written as

$$P_Q = C(\omega) \left(\frac{1}{2}\Gamma - \frac{1}{2}\Gamma_P + C_Q \left(\frac{\rho}{\rho_0} \right)^\alpha \right) \rho$$

with

$$C(\omega) = \frac{4}{9}q \left(\frac{f^*}{m_\pi} \right)^2 \frac{m_N^2}{s} |G_{\Delta h}(\omega)|^2$$

where s is the πN center-of-mass energy, $f^*/4\pi = .36$ is the $\pi\Delta N$ coupling constant, Γ is the free Δ width and Γ_P is the Pauli correction. The local density is ρ and the normal nuclear matter density is ρ_0 . $G_{\Delta h}$ is the Δ -hole propagator written as

$$G_{\Delta h}(\omega) \simeq \left(\omega - \omega_R + \frac{1}{2}i\Gamma - \frac{1}{2}i\Gamma_P - iIm\Sigma_\Delta \right)^{-1}$$

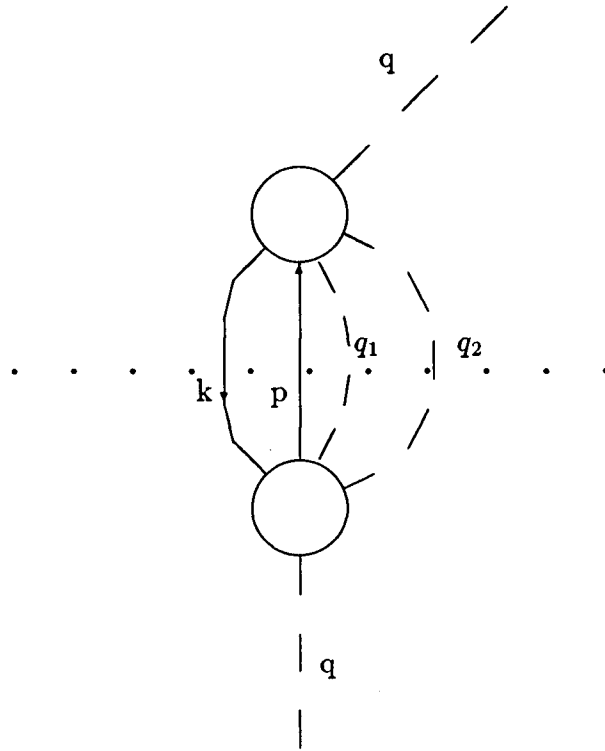


Figure 32: A diagram showing the part of the pion-nucleus optical potential corresponding to a particle-hole- 2π excitation, used for the calculation of the $(\pi, 2\pi)$ process.

with $\omega_R \simeq 2.2m_\pi$. The imaginary part of the Δ self-energy, $Im\Sigma_\Delta$, contains contributions from higher order quasi-elastic scattering and two- and three-body absorption and is written as

$$Im\Sigma_\Delta = - \left[C_Q \left(\frac{\rho}{\rho_0} \right)^\alpha + C_{A_2} \left(\frac{\rho}{\rho_0} \right)^\beta + C_{A_3} \left(\frac{\rho}{\rho_0} \right)^\gamma \right].$$

The absorption probability can be written in a form similar to the quasi-elastic scattering as

$$P_A = C(\omega) \left[C_{A_2} \left(\frac{\rho}{\rho_0} \right)^\beta + C_{A_3} \left(\frac{\rho}{\rho_0} \right)^\gamma \right].$$

The outgoing pions will mostly be of energy less than 100 MeV in the lab for incident pions up to approximately 300 MeV. The Δ -hole model is known to be inadequate for describing such low pion energies. Instead, an eikonal two-body absorption form is used with an absorption coefficient $C'(\omega)$ defined so that

$$\sigma_{abs}(\omega) = \int d^2b \left[1 - \exp \left(- \int_{-\infty}^{\infty} C'(\omega) \rho^2(b, z) dz \right) \right]$$

reproduces existing absorption total cross section data. Coulomb distortion is accounted for by multiplying the value of the impact parameter integral by the geometrical factor

$$\frac{\pi b_{max}^2}{\pi R^2}$$

and equating the result to the measured experimental cross sections. Here, b_{max} is the impact parameter for which the pion has a distance of closest approach equal to the half density radius R . By taking the pion energy at the nuclear surface to be

$$T_\pi \pm \frac{Ze^2}{R}$$

Oset and Vicente-Vacas find that the same $C'(\omega)$ can be used to describe π^+ and π^- absorption and parameterize it by

$$C'(\omega) = .20T_\pi + 2.5$$

where T_π is in MeV and C' has units of fm⁵. The phenomenological absorption approach for low energy absorption matches the contribution from the Δh model at $T_\pi \approx 95$ MeV at a density of $\frac{3}{4}\rho_0$. The outgoing attenuation factors are found to reduce the outgoing flux by about 20%.

With these considerations, the cross section can be written as

$$\begin{aligned} \sigma = & \frac{\pi}{q} \int d^2b dz \exp \left(- \int_{-\infty}^z dz' C(\omega) \right) \\ & \times \left[\frac{1}{2} \Gamma - \frac{1}{2} \Gamma_P + C_Q \left(\frac{\rho}{\rho_0} \right)^\alpha + C_{A_2} \left(\frac{\rho}{\rho_0} \right)^\beta + C_{A_3} \left(\frac{\rho}{\rho_0} \right)^\gamma \right] \rho(b, z') \\ & \times \int \frac{d^3k}{(2\pi)^3} \frac{d^3q_1}{(2\pi)^3} \frac{d^3q_2}{(2\pi)^3} n(\vec{k}) [1 - n(\vec{q} + \vec{k} - \vec{q}_1 - \vec{q}_2)] \sum_{s_i s_f} |T|^2 \\ & \times \frac{1}{2\omega(\vec{q}_1)} \frac{1}{2\omega(\vec{q}_2)} \delta(q^0 + \epsilon(\vec{k}) - \Delta E - \omega(q_1) - \omega(q_2) - \epsilon(\vec{q} + \vec{k} - \vec{q}_1 - \vec{q}_2)) \\ & \times \exp \left(- \int_{(b,z)}^{\infty} dl_1 C'(\omega) \rho^2(\vec{r}_1) \right) \exp \left(- \int_{(b,z)}^{\infty} dl_2 C'(\omega) \rho^2(\vec{r}_2) \right) \end{aligned}$$

where ΔE is the energy gap between the nuclear ground state and the first excited state of the nucleus (this allows some excitation energy to be transferred to the nucleus). One can easily recognize the elements describing the distortions. The positions of pions 1 and 2 in the final state are \vec{r}_1 and \vec{r}_2 . The lengths dl_1 and dl_2 are in the directions of \vec{q}_1 and \vec{q}_2 . The occupation number n refers to the protons and $1 - n$ to the neutrons, thus an isospin sum is not required in the cross section formula. The nucleon energies are denoted by ϵ . This formula describes only the one-body contributions to the production process and ignores possible two-body contributions.

A major effect, as it turns out, that has not yet been considered is the effect on the phase space in the momentum integrations (which is governed by the energy δ function) if the particle potential energies are considered, or equivalently, the effect of particle binding in the medium. For the nucleons, one has the difference of initial and final energies, so that if the potential is considered independent of

nucleon energy, any potential energy contribution cancels. For the incident pion, the total energy, q_0 is conserved so that there is no effect. The energies of the final state pions add, however. The pion-nucleus potential is generally attractive except for low energy pions where the s-wave repulsion can dominate. Essentially then, for a given pion momentum, the pion's energy in the medium, $\tilde{\omega}(q)$, will be lower, so that larger pion momenta can be reached. The use of this effect was found to be important in describing the Λ mesonic decay width in the nucleus [OS85].

The binding effect is included by [OV86] in the calculation by modifying the free pion propagator to include the s- and p-wave contributions to the pion self-energy. The energy integrations, which before gave the factors $(2\omega(q))^{-1}$, give now for the residues of the propagator

$$Res D = \frac{1}{2q^0 - \frac{\partial \Pi}{\partial q^0}} \bigg|_{q^0 = \tilde{\omega}(q)}$$

where Π is the pion self-energy and $\tilde{\omega}(q)$ is determined by the poles of the new propagator

$$\tilde{\omega}^2(q) - \vec{q}^2 - m_\pi^2 - Re \Pi(\tilde{\omega}(\vec{q}), \vec{q}).$$

The residue factor is introduced for each of the outgoing pions. Additionally, the δ function is replaced by

$$\delta(q^0 + \epsilon(\vec{k}) - \Delta E - \tilde{\omega}(q_1) - \tilde{\omega}(q_2) - \epsilon(\vec{q} + \vec{k} - \vec{q}_1 - \vec{q}_2)).$$

The large amount of integration implied by the cross section equation is carried out by a Monte Carlo method, avoiding approximations in the integrands at the cost of computer time. The estimated error of the integrations is given as 15% [OV86]. The results of the calculation for the $^{16}O(\pi^+, \pi^+\pi^-)$ calculation from [OV86] are shown in Figure 31. The lower dashed curve is the calculation where the effects of precursor enhancement and binding have been ignored. The dot-dash curve includes the effects of binding. This effect increases the cross section by more

than a factor of two over the whole energy range shown. The effect of including the precursor enhancement is found by Oset and Vicente-Vacas to be small, yielding only a 15-20% increase in cross section, shown as the upper solid line in Figure 31, in contrast to [CE83] which predicted large effects. A major cause of this difference is that only part of the T-matrix amplitude was renormalized.

Differential cross sections can also be calculated. The program AXPF1LIG was obtained from Vicente-Vacas and produces a matrix describing the distributions of outgoing particles based upon the equations outlined above. The matrix is produced with the final π^- angle (the QQD particle) fixed at some lab angle, while the angle of the π^+ and the energies of both final pions are unconstrained, except for being in the reaction plane. By then supplying the experimental angular and energy constraints, the matrix is evaluated by another program, AP1, also obtained from Vicente-Vacas, to produce differential cross sections as well as integrated total cross sections. The cross section magnitudes are somewhat sensitive (at the 10% level) to the shape of the nucleus on the periphery as given by the thickness parameter t . As mentioned above, the effects of quasi-elastic scattering are not included in the final state for the pions. The differential cross sections might then be expected to have difficulty describing the energy behaviour of the detected pions. Angular distributions are not expected to have large variations so that the quasi-elastic effect there will be less.

The models discussed above all assumed that the one-body mechanism dominated the $(\pi, 2\pi)$ process in nuclei. A mechanism involving the direct participation of two nucleons has been proposed as a possible contributor to the $(\pi, 2\pi)$ reaction. The double Δ model of [BTWW82,SWB83] was originally proposed to help explain some characteristics of pion absorption in nuclei. Pion absorption data indicate [MSS*80,MSS*81] that between three to five nucleons are apparently involved in the pion absorption process in the nucleus and that the

ratio of proton yields from π^+ absorption to π^- absorption was approximately four for a variety of nuclei. One would expect a ratio of approximately 10 assuming quasi-deuteron absorption.

A pion which interacts with a nucleon can form a Δ which can in turn interact with surrounding nucleons in a nucleus. From simple SU(4) quark models, one expects that a strong $\Delta N \rightarrow \Delta\Delta$ transition is allowed. Involving two more of the nucleons in the nucleus, the $\Delta\Delta$ could then de-excite into four nucleons which would be emitted from the nucleus. The $\Delta\Delta$ mechanism is shown schematically in Figure 33. The $\Delta\Delta$ would be preferentially formed in a $T = 2$ state from a $T = 1$ NN pair. Formation of $T = 1$ $\Delta\Delta$ states are suppressed by a factor of 3 relative to $T = 2$ states. The $\Delta\Delta$ state can also have a branching into a $\pi\pi NN$ final state, that is, into the pion production channel. If the incident pion energy is high enough so that the channel is not too heavily kinematically suppressed, then this branching could be substantial. This could give a large contribution to the $(\pi, 2\pi)$ cross section considering that the absorption cross section is quite large in comparison to the free $(\pi, 2\pi)$ cross section. For incident π^+ , the produced pion pairs will be π^+ pairs a large fraction of the time, so that if a measure of the ratio

$$\frac{\sigma(\pi^+\pi^+)}{\sigma(\pi^+\pi^-)}$$

is made, the result may be significantly different from that expected from a one-body mechanism. A measurement of this ratio is part of a competing $(\pi, 2\pi)$ program at SIN [AAL*84]. For $(2\pi^+)$ or $(2\pi^-)$ final state pairs, the possibility of analyzing the angular correlations of the pairs to look for the Hanbury-Brown-Twiss effect [GKW79] is present. This effect would manifest itself as intensity correlations of the outgoing pions and could possibly be used to extract information on the space-time extent of the pion production source if sufficient statistics are available in the final state. No cross section estimates for

pion production have yet been made assuming this model, only an estimate of the four nucleon absorption in ${}^4\text{He}$ has been done [SWB83].

IV.3 Monte Carlo Reaction Simulations

It should be possible to describe some of the observed experimental features of the data by examining the kinematical constraints present but ignoring the detailed dynamics of the reaction itself. The simplest approach in this direction is to calculate the phase-space distributions of the final state particles. That is, assuming the number of particles in the final state, the particle momenta distributions are calculated in a Monte Carlo approach in a statistical manner, without the consideration of factors such as relative angular momenta of the final particles. The computer code FOWL [Jam68] is used to calculate the phase-space distributions. The experimental apparatus is then introduced into the calculation by applying cuts to the output data corresponding to the physical limitations of the apparatus. The phase-space was calculated for a four-body final state for the reaction

$$\pi^+ + {}^{16}\text{O} \rightarrow \pi^+ + \pi^- + p + {}^{15}\text{O}.$$

It is possible for the $(\pi, 2\pi)$ process to proceed through many different reaction channels. These channels may have characteristic signatures differing from the pure four body phase-space prediction due to the formation and decay of various intermediate states. An existing set of subroutines describing the relativistic kinematics of a range of subprocesses [Ols87], including two body scattering, particle formation or decay and reactions with three particles in the final state, was used to describe selected multi-step processes in a Monte Carlo approach. The kinematics for each step is carried out in the center of mass (CM) frame of the particles involved and the results are converted to the lab system to

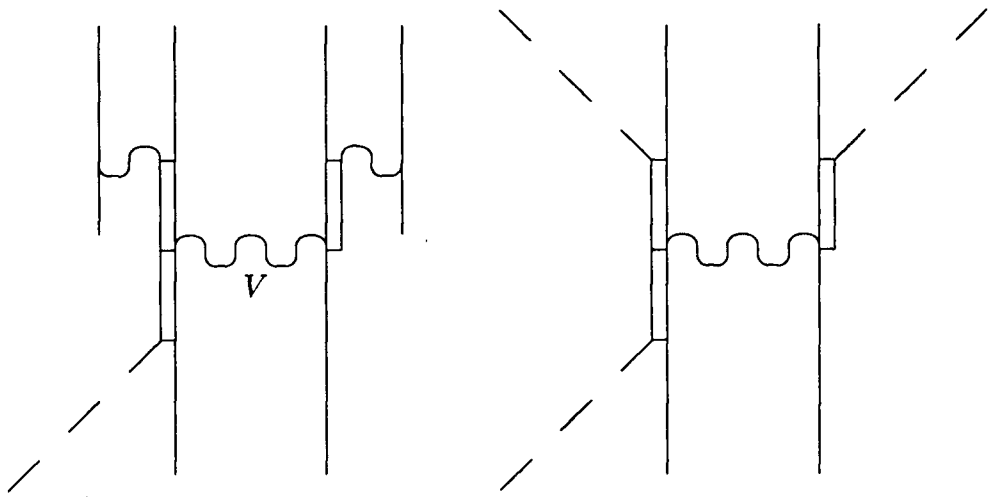


Figure 33: The $\Delta\Delta$ mechanism [BTWW82,SWB83] showing the formation of the $\Delta\Delta$ state and its decay into 4 nucleons or into two pions and two nucleons.

then carry on to the next step or trace to the apparatus.

The incoming pion four-momentum is labelled by $q_\pi = (E_\pi, \vec{q}_\pi)$ with the energy and three-momentum related by $q^2 = E_\pi^2 - \vec{q}_\pi^2 = m_\pi^2$. The incident pion is assumed to interact with a cluster of n nucleons in the nucleus with a four-momentum of $k_n = (E_n, \vec{k}_n)$ with n taken as one or two nucleons depending upon the mechanism simulated. The momentum of the cluster is chosen to have a uniform angular distribution in the lab and the magnitude is chosen from a gaussian distribution with standard deviation of

$$\sigma_n = \frac{\hbar c}{\sqrt{2}\alpha} \sqrt{\frac{n(A-n)}{A}}$$

where α is the harmonic oscillator parameter [DJDVDV74] for the target nucleus and A is the number of target nucleons.

The reaction steps are done in the CM frame, so the initial particles in each step must be boosted from the lab into the CM frame and the final particles must be boosted back into the lab frame. For the incident particle step, the velocity of the CM frame is given by,

$$\vec{\beta} = \frac{\vec{q}_\pi + \vec{k}_n}{E_\pi + E_n}$$

and the corresponding γ factor is defined by

$$\gamma = (1 - \beta^2)^{-1/2}.$$

The CM quantities are then given by, for a general four-momentum $p = (E, \vec{p})$,

$$p'_z = \gamma(p_z - \beta E)$$

$$E' = \gamma(E - \beta p_z)$$

where the z -axis here denotes the direction of the boost $\vec{\beta}$. The momenta components perpendicular to the boost are unaffected. In the case of two-body

scattering or particle decay, the magnitude of the CM momenta of the final particles is determined by the CM energy, E_{CM} , of the initial particles defined by

$$E_{CM}^2 = (\sum p)^2 = (\sum E)^2 - (\sum \vec{p})^2$$

and the masses of the final particles. The particle directions are randomly chosen in the center of mass frame.

The final state of a reaction step can contain three particles. The step can then be treated as a series of two two-body decay steps

$$a + b \rightarrow c + d' \rightarrow c + d + e.$$

The outgoing particles must then be weighted by the phase space weight corresponding to the three final momenta. This weight can be calculated making use of the recursion characteristics of phase-space factors [Hag63] which for the case of a three body final state gives a weight

$$R = \frac{\pi^2 m_{d'}}{4 E_{CM}^2 m_{d'}} \left(\left[E_{CM}^2 - (m_{d'}^2 + m_c)^2 \right] \left[E_{CM}^2 - (m_{d'}^2 - m_c)^2 \right] \right)^{1/2} \\ \left(\left[m_{d'}^2 - (m_d + m_e)^2 \right] \left[m_{d'}^2 - (m_d - m_e)^2 \right] \right)^{1/2}$$

which is to be applied to each generated event. $m_{d'}$ is the mass of the intermediate step in the decay and is randomly selected in the interval $(m_d + m_e, E_{CM} - m_c)$. If one of the particles involved in the process is a Δ , the Δ can be selected from a Lorentzian distribution

$$P(m) = \frac{\Gamma_{\Delta}}{2\pi \left(\frac{\Gamma_{\Delta}^2}{4} + (m - m_{\Delta})^2 \right)}$$

if the mass is not constrained by a formation process. Alternatively, the event can be weighted by

$$\frac{P(m)}{P(m_{\Delta})}.$$

Γ and m_Δ are the nominal free Δ characteristics with values 115 MeV and 1232 MeV.

A number of processes were considered with this Monte Carlo approach. The relative importance (that is, the amplitudes corresponding to each mechanism) of each mechanism was not considered here. The processes considered were

$$\pi^+ + n \rightarrow \pi^+ + \pi^- + p$$

$$\pi^+ + n \rightarrow \pi^+ + \Delta^0 \rightarrow \pi^+ + \pi^- + p$$

$$\pi^+ + n \rightarrow \Delta^+ \rightarrow \pi^+ + \Delta^0 \rightarrow \pi^+ + \pi^- + p$$

and

$$\pi^+ + 2n \rightarrow \Delta^+ + n \rightarrow \Delta^+ + \Delta^0 \rightarrow \pi^+ + \pi^- + p + n.$$

The first process models the pion pole term with the dynamics removed and hence yields the quasi-free phase-space distribution. The produced spectra are consistent with the model predictions from [OV87] which should be proportional to the quasi-free phase-space (ignoring, for the moment, the distortions of the space resulting from considering the pion self-energy term) and hence confirms the validity of the simulation coding. The second and third processes involve Δ propagation with the third process expected to be small from calculations of [OV85]. The second process is a modified two point process (see Figure 1) while the third is a modified three point process. Since the reaction dynamics are not considered in this simulation, the second and third processes are identical except for an additional weight factor for the intermediate Δ^+ . The last process is the $\Delta\Delta$ mechanism of [BTWW82].

The incident pion can be given a variable incident energy and trajectory with limits defined by the experimental beam characteristics. Variation of incident energy and trajectory was found to have only a small effect on the output

distributions. The inclusion of the Fermi momentum of the starting cluster was found to be important. Results of these simulations are compared to some of the data in Chapter V.

Chapter V

The Results

The only comparison made to this point between the experimental data and the various predictions has been done with the integrated total cross sections, as shown in Figure 31. The total cross section results are discussed in more detail below in section V.1. Obviously, there is much more data to be discussed than just the total cross section, namely the various differential cross sections that can be extracted. The only available differential cross section predictions are from the model of [OV86,OV87]. We can also compare predictions from phase-space calculations as well as predictions from the Monte Carlo reaction simulations to the differential cross sections. The differential cross sections are discussed in section V.2.

V.1 Total Cross Section

The measured total $^{16}\text{O}(\pi^+, \pi^+\pi^-)$ cross section is $2.25 \pm .35 \text{ mb}$, which is approximately six times the free $p(\pi^-, \pi^+\pi^-)$ cross section. The measured $^{16}\text{O}(\pi^+, \pi^+\pi^-)$ cross section is also 40% of the inclusive DCX cross section [Woo84] at this energy, which is substantially larger than previously assumed in measurements of the inclusive DCX reaction. One naively expects at most only about one-half of this measured total cross section as the effective number of neutrons in the oxygen nucleus is roughly three as determined from quasi-elastic pion scattering in this energy region, not six as implied by the $^{16}\text{O}(\pi^+, \pi^+\pi^-)$ total cross section datum. From the comparison of the theoretical predictions of

the total cross section and the measured cross section in Figure 31, it is apparent that the predictions of the model of Oset and Vicente-Vacas [OV86] give the best agreement with the datum when the effects of the nuclear potential on the outgoing pions are included. The further inclusion of precursor effects raised the cross section predictions by only 15-20%, but this worsened the agreement with the datum. Without the inclusion of the pion self-energy (that is, the binding effect), the model predictions are substantially below the data, giving only 1030 *mb* for the total cross section at 280 MeV as compared to 2750 *mb* when the binding is included. The predictions of [CE83] are not excluded by the datum, as the quoted error for this model is 30%. However, if a proper production amplitude were to be included in this calculation, the predicted cross sections would rise substantially, at least a factor of five, making the predictions of [CE83] much too high to be reconciled with the datum and indeed, well above even the inclusive DCX cross section. The total cross section prediction of [Roc83] is too low compared to the datum. For the Rockmore model, the region of validity of the calculational method is restricted to only a few tens of MeV above threshold, and cannot be expected to be too reliable at 280 MeV.

V.2 Differential Cross Sections

The Oset model, with the pion self-energy included but not the virtual pion renormalization, adequately describes the cross section magnitude. The differential cross section predictions will now be examined. The output matrix results from the theoretical model Monte Carlo [OV86,OV87] are evaluated with the relevant experimental cuts applied. The matrix contains the calculation results binned according to the laboratory values of $\theta_{\pi+}$, $T_{\pi+}$ and $T_{\pi-}$. For purposes of comparing to the experimental data, the matrix results are smoothed when plotted to remove variations arising from the statistical nature of the Monte Carlo

calculation. The π^- angle is forced beforehand to be one of the three QQD angle settings used in the experiment so that there are three separate matrix files to describe the entire data set. If the predictions of the model without the binding effect are to be examined, additional matrix files are needed.

The data is also compared, in some cases, to the predictions from a phase-space calculation for the process $^{16}\text{O}(\pi^+, \pi^+\pi^-) \{p + ^{15}\text{O}\}$, which is shown to be essentially the same in shape as the Oset model results. Predictions of some reaction simulations are also compared to the data. Only a sampling of the total data will be shown so that the reader is not swamped by mounds of pictures. The cross sections shown are all tabulated in Appendix A.

V.2.1 Positive Pion Spectra

The four-fold differential cross sections for the detected pions are evaluated using the formula in section III.2.1. The energy spectra of the measured π^+ are generally peaked at low energy, with the peaking most prominent for the settings with the QQD and CARUZ at their forward angle settings. The low energy peaking behaviour of the π^+ 's is shown in Figure 34.

The data in Figure 34 includes the results from both angular settings of the CARUZ and both momentum settings of the QQD with the QQD set at 50° . The predictions of the Oset model are shown by the double-dashed line for the calculation where the pion self-energy term, Π , has been omitted, and a double solid line for the calculation where Π is included. Note that in all the remaining plots which show results from the Oset model, a thick dashed line is used instead of the double dashed line and a thick solid line instead of a double solid line (this is simply due to the loss of line resolution in the plot upon reduction). The thick solid line in Figure 34 shows the result of a phase-space prediction for the process

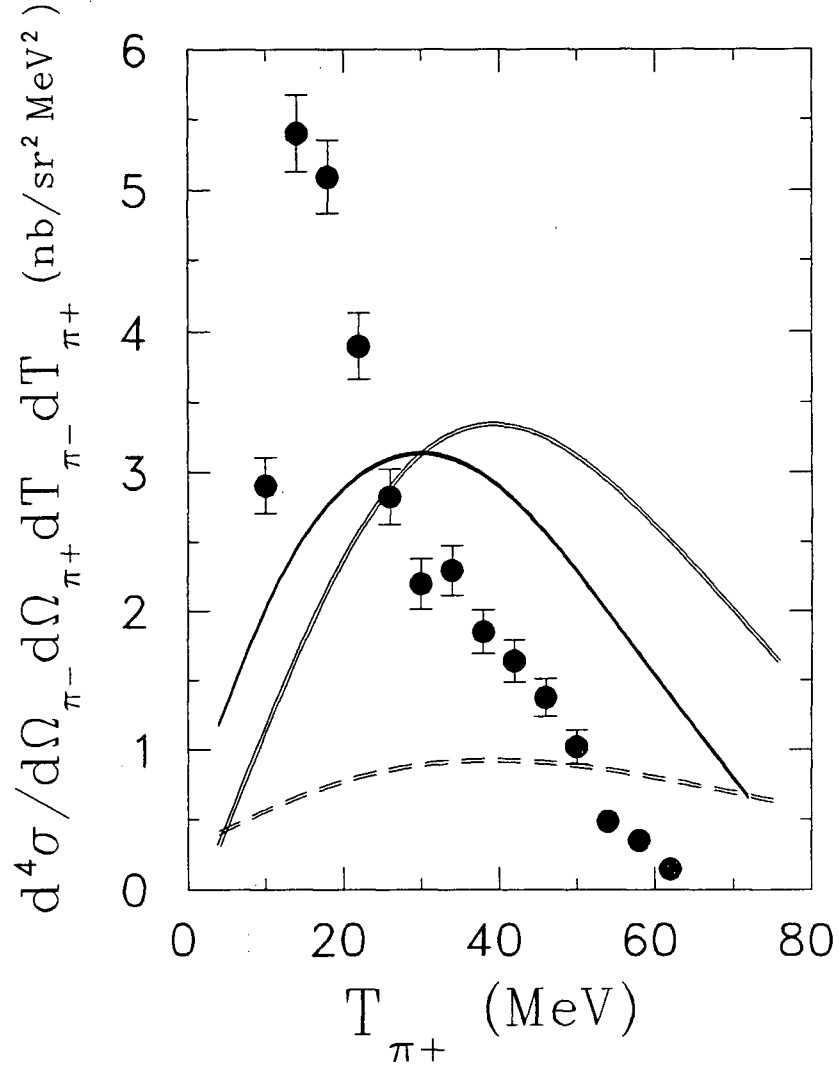


Figure 34: The energy spectrum of π^+ 's for the data set with the QCD at 50° . The thick solid line is the phase-space prediction. The two other curves are the results from [OV87] as discussed in the text.

$^{16}\text{O}(\pi^+, \pi^+\pi^-) \{p + ^{15}\text{O}\}$. The model calculation peaks at approximately 40 MeV for the π^+ , while the four-body phase-space peaks near 30 MeV, both substantially above the data which peaks below 20 MeV. The phase-space has been normalized such that the area under the phase-space curve corresponds to the area under the data (with the π^+ energy extrapolation correction). As mentioned earlier, the model calculation results are proportional to the phase-space for the quasi-free reaction, with the additional effect of the pion self-energy distorting the phase-space to some degree, and is not substantially different from the four-body phase-space prediction. Since the four-body phase-space is similar to the model calculation, it is not shown in further plots.

The data sets can be divided into subsets of pairs of QQD momentum and CARUZ angle settings and compared to the model predictions in more detail. The behaviour of the π^+ energy spectrum as a function of the QQD angle is demonstrated in Figure 35 where the data is limited to the subset with the CARUZ at 50° and the QQD accepting $65 \text{ MeV} < T_{\pi^-} < 110 \text{ MeV}$ for each of the three QQD angles; 50° , 80° , and 115° . The low energy peak appears to shift to lower energies as the QQD angle increases and disappears altogether in the 115° data. It is only for the more backward angle setting of the QQD that the measured π^+ spectrum approaches the shape of the model prediction.

The results from the kinematical Monte Carlo simulations done to model some of the potential mechanisms contributing to the $(\pi, 2\pi)$ reaction can be compared to the π^+ energy spectra to look for processes that may give a low energy peak. Figure 36 shows again the 50° data and the smoothed output from the simulations of the following two reactions; the Δ reaction

$$\pi^+ + n \rightarrow \pi^+ + \Delta^0 \rightarrow \pi^+ + \pi^- + p$$

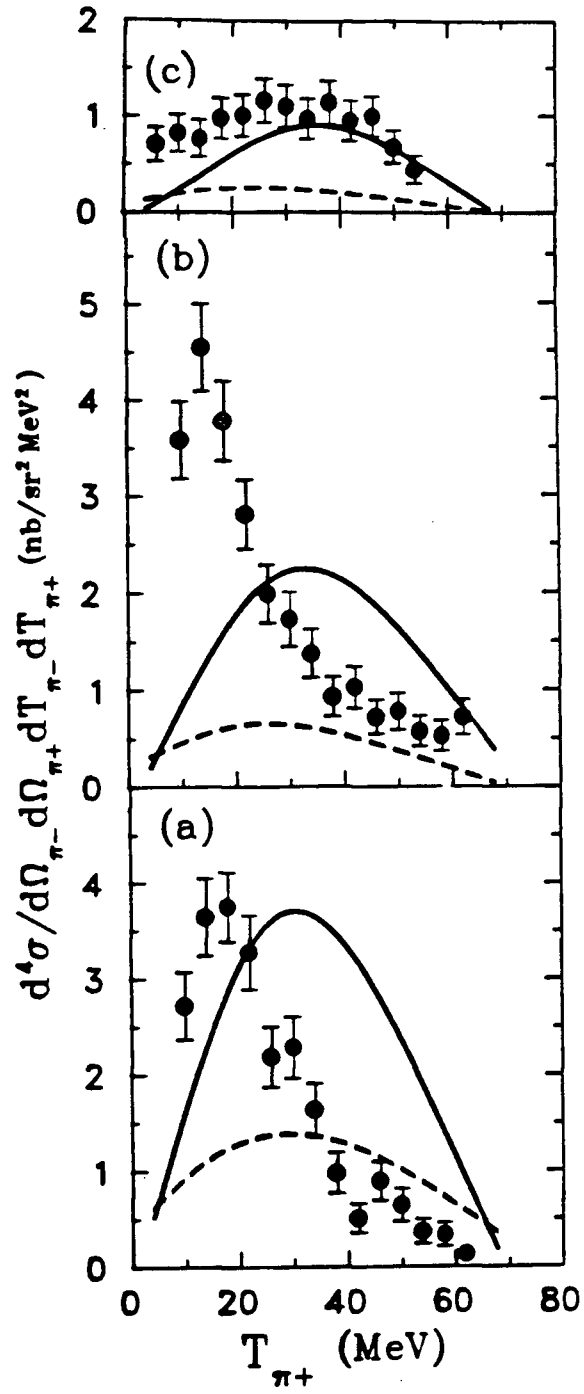


Figure 35: The energy distribution of π^+ in the CARUZ for the CARUZ at 50° and the QCD at high momentum. The QCD is at a) 50° , b) 80° and c) 115° . The curves represent the model calculations of [OV87].

and the $\Delta\Delta$ reaction

$$\pi^+ + 2n \rightarrow \Delta^+ + n \rightarrow \Delta^+ + \Delta^0 \rightarrow \pi^+ + \pi^- + p + n.$$

The simulation results have been normalized so that the area under the simulation curves correspond to the integrated area of the data. The reaction

$$\pi^+ + n \rightarrow \Delta^+ \rightarrow \pi^+ + \Delta^0 \rightarrow \pi^+ + \pi^- + p$$

gives results very similar to the Δ reaction results discussed here. The $\Delta\Delta$ results are seen to have little energy dependence, in sharp disagreement with the experiment. The Δ reaction does produce a substantial low energy peaking very similar to the data at 50° . However, at 115° , where the low energy peak is no longer present in the data, the Δ reaction mechanism still predicts its presence.

In order not to bias the comparison of the experimental results with the model predictions of Oset for the other measured kinematic variables, the data is integrated over the π^+ energy. In this way, the failure of the model to describe the π^+ energy distribution will not affect the comparison to the angular distribution of the π^+ . The angular distributions of the π^+ for the three QQD angle settings are given in Figure 37. The data shown are for the QQD set to accept the energy range $65 \text{ MeV} < T_{\pi^-} < 110 \text{ MeV}$ (the 115° data were taken only for the high momentum setting). The curves for the theoretical model predictions have the same meaning as in Figure 34. The predictions of the intermediate Δ reaction simulation are shown by the thin solid line.

The angular distribution trends of the data are nicely reproduced in shape by the model calculation, which has had the same high π^- energy cut applied to it as the data. The measured decline of the data to zero cross section at backward π^+ angles for the 115° data also nicely demonstrates the lack of sizeable background in the measurement. The agreement of the differential cross section

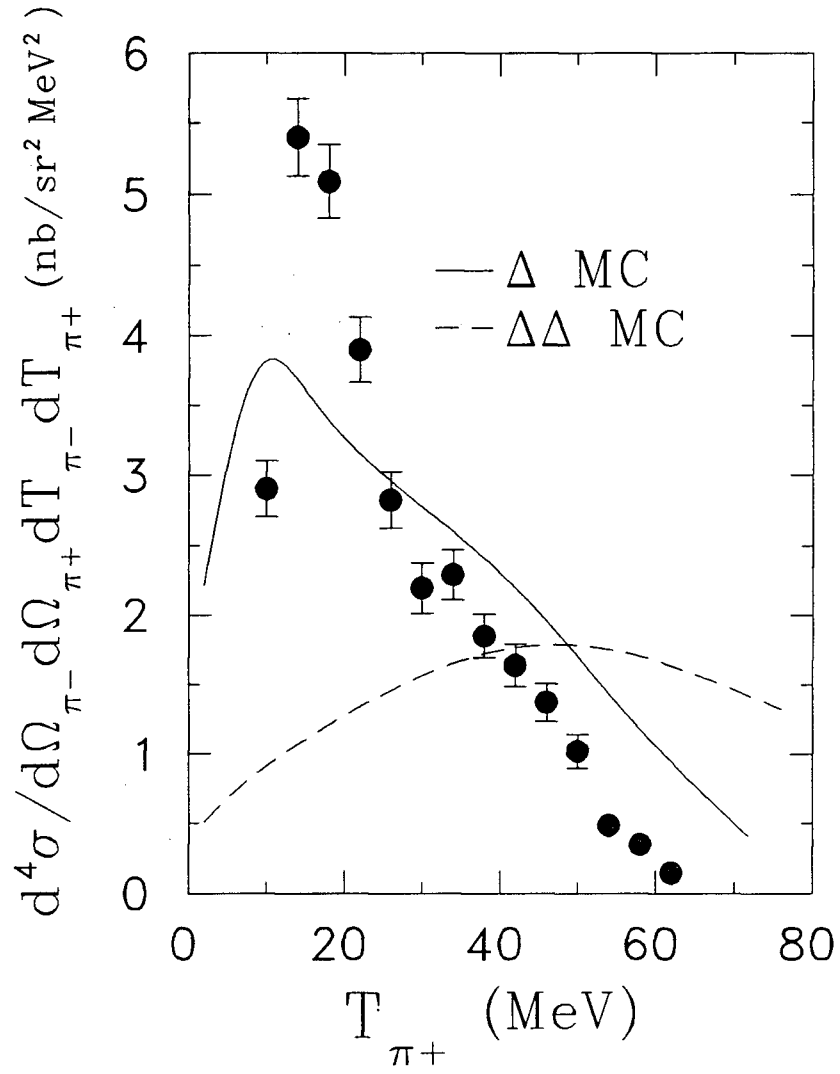


Figure 36: The energy distribution of π^+ in the CARUZ for 50° QQD data compared to the results of the intermediate Δ (solid) and $\Delta\Delta$ (dashed) reaction simulations.

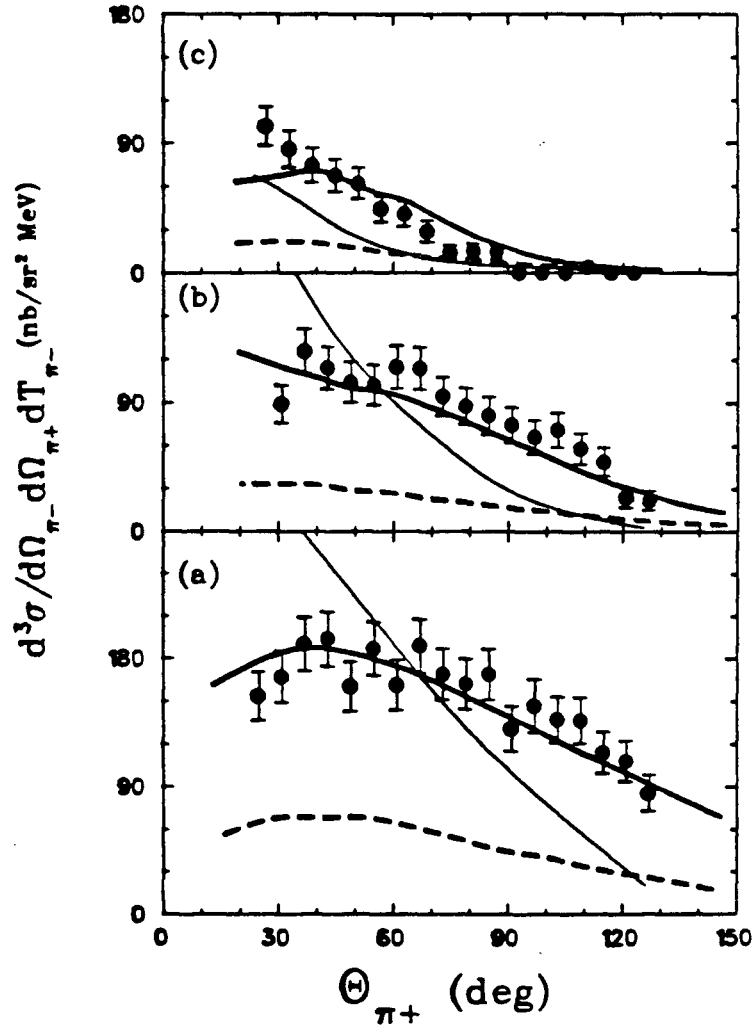


Figure 37: The angular distribution of π^+ in the CARUZ. The QQD is at a) 50° , b) 80° and c) 115° . The thin solid curve is the Δ model prediction while the thick dashed and solid lines are results of [OV87].

magnitudes is consistent with the degree of agreement of the total cross sections. The distributions tend to be forward peaked, and grow more forward peaked with increasing QQD angle, which supports the assumption of the dominance of a quasi-free mechanism. If the reaction directly involved more than one of the nucleons in the nucleus, the reaction products might be expected to be more uniformly distributed in the lab. The kinematical simulation results do display a forward peaking in the π^+ , however the peaking is sharper than the data indicate. This does not necessarily rule out the possible importance of this mechanism as the effects of final state distortions would broaden the sharp forward peaking to some degree. The kinematic simulations have been normalized to the results from the 50° QQD setting.

V.2.2 Negative Pion Spectra

The T_{π^-} spectra will be examined here as triple differential cross sections as a function of the π^- kinetic energy, similar to above where the triple differential cross section as a function of the π^+ angle was examined. The model results are then not affected by the poor description of the π^+ energy spectra. The π^- energy spectra for the three QQD angle settings is shown in Figure 38. The data, and calculated curves, are shown for the subset of data with the CARUZ at 50°.

The data generally show an increasing yield as T_{π^-} decreases, at least down to the lower limit of the measured T_{π^-} range, with an indication of a maximum yield reached in the range of 40-50 MeV. The maximum in the energy yield could be partially an instrumental effect resulting from the high energy cutoff of the CARUZ. The Oset model does a generally good job of describing the shape of the π^- energy spectra at all angles. This agreement in shape is the reason for using the model calculation shape to estimate the extrapolation correction for T_{π^-} at

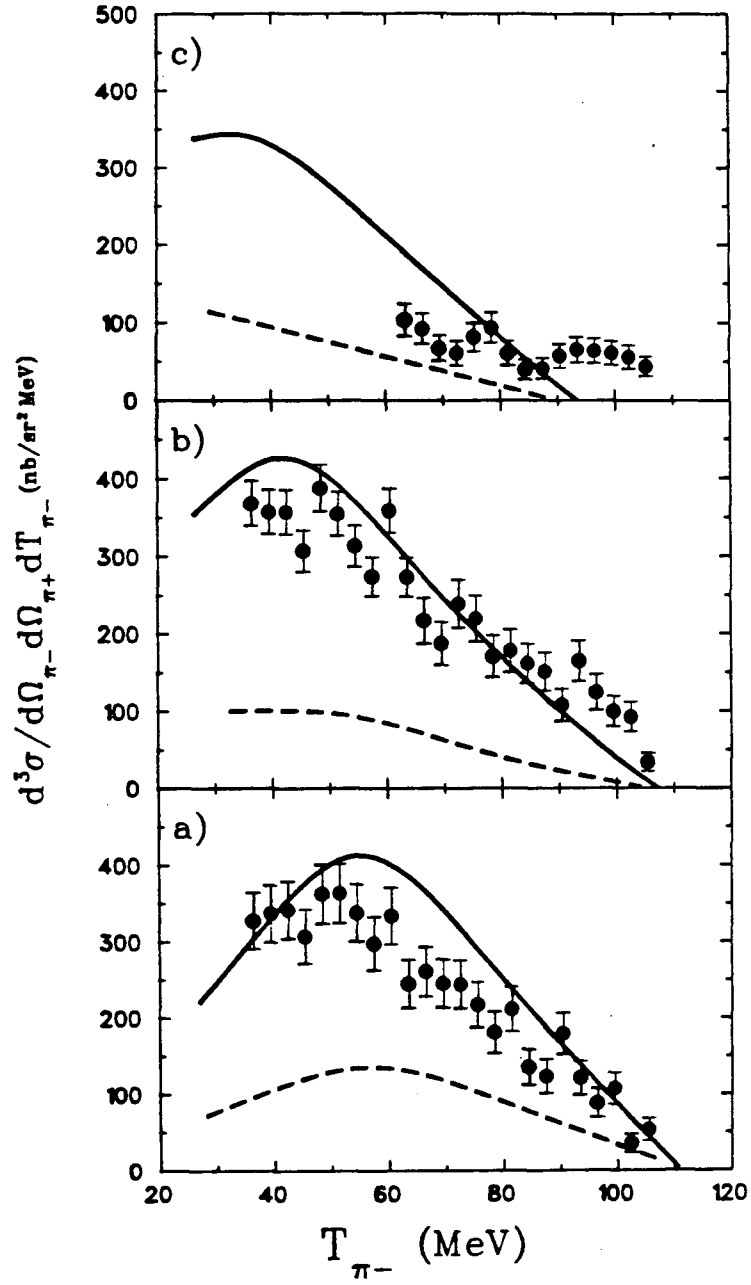


Figure 38: The energy spectrum of π^- 's for the data set with the QCD at a) 50° , b) 80° and c) 115° . The curves are results of [OV87] and are discussed in the text.

115° (see section III.2.2). There is a tendency in the data, especially at higher angles, for the calculated cross section to drop faster with increasing energy than the data at the high end of the measured π^- energy range. This tendency has been taken into account in estimating the error of the π^- extrapolation for the 115°. The Oset model predicts a maximum where the data shows it, but an inclusion of quasi-elastic effects in the model would certainly tend to lower in energy the overall energy spectrum. The Δ reaction simulation (not shown) gives a energy peak considerably above the data in the 50° set. For more backward QGD angles, this peak moves below the QGD energy cutoff.

The measured angular distribution of the π^- 's was given in Figure 27 where the Legendre polynomial fit was performed. The shape of the experimental data is reproduced by the prediction of the theoretical model (not shown), up to the 20% discrepancy between the data and theoretical model. The π^- angular distribution shows the forward angular peaking characteristic of the quasi-free reaction assumed to be responsible for the $^{16}\text{O}(\pi^+, \pi^+\pi^-)$ process.

V.2.3 Missing Mass

The data can be examined in a form that contains information from both the detected pions. The missing mass, M_X , is such a quantity and indicates the amount of available energy not taken up by the two detected pions. Such missing energy would be taken up by the target nucleus through emission of an energetic nucleon (for example, the proton resulting from quasi-free production) and/or by leaving the residual nucleus in an excited state.

The missing mass is calculated as

$$M_X = T_i - \sum T_f + Q$$

where Q is the Q-value of the reaction (-153.9 MeV), calculated assuming the

residual nucleus to be $^{16}F_{g.s.}$. The atomic mass defects used to calculate the reaction Q-value were taken from [LS78]. ^{16}F is particle unstable to proton emission. The Q-value for assuming a $p + ^{15}O_{g.s.}$ final nuclear state differs by less than 1 MeV from the value taken here.

A sample missing mass spectrum is shown in Figure 39 for the QQD at 50° accepting the T_{π^-} of 65-110 MeV. The spectrum displays no sharp peak, reaching a maximum yield at about 20 MeV. For this experimental setting, the M_X is constrained somewhat to be small by the lower π^- energy limit applied. The absence of any sharp peak indicates that no particular final state of the residual nuclear system is strongly excited. The matrix files representing the results of the theoretical calculation are coarsely binned in pion energy (8 MeV) which makes a large uncertainty in the summed energy. Also, the Oset model has already been shown to inadequately describe the T_{π^+} energy spectrum and this shortcoming would be reflected in the in the missing mass also. For these reasons, the theoretical predictions are not shown in Figure 39.

V.3 Summary

The reaction $^{16}O(\pi^+, \pi^+\pi^-)$ at 280 MeV incident pion energy has been measured with the result for the total cross section

$$\sigma_{tot} = 2.25 \pm .35 \text{ mb.}$$

The model of [OV86,OV87] was found to explain many of the features of the data. The predicted total cross section was 2.75 mb, 20% higher than the measured value, and just outside the limits of the experimental error estimate. Considering that the results of the model are sensitive to the parameterization of the nuclear density and that the quoted uncertainty of the model calculation is 15%, the model results and the data can be considered to be in agreement. The agreement

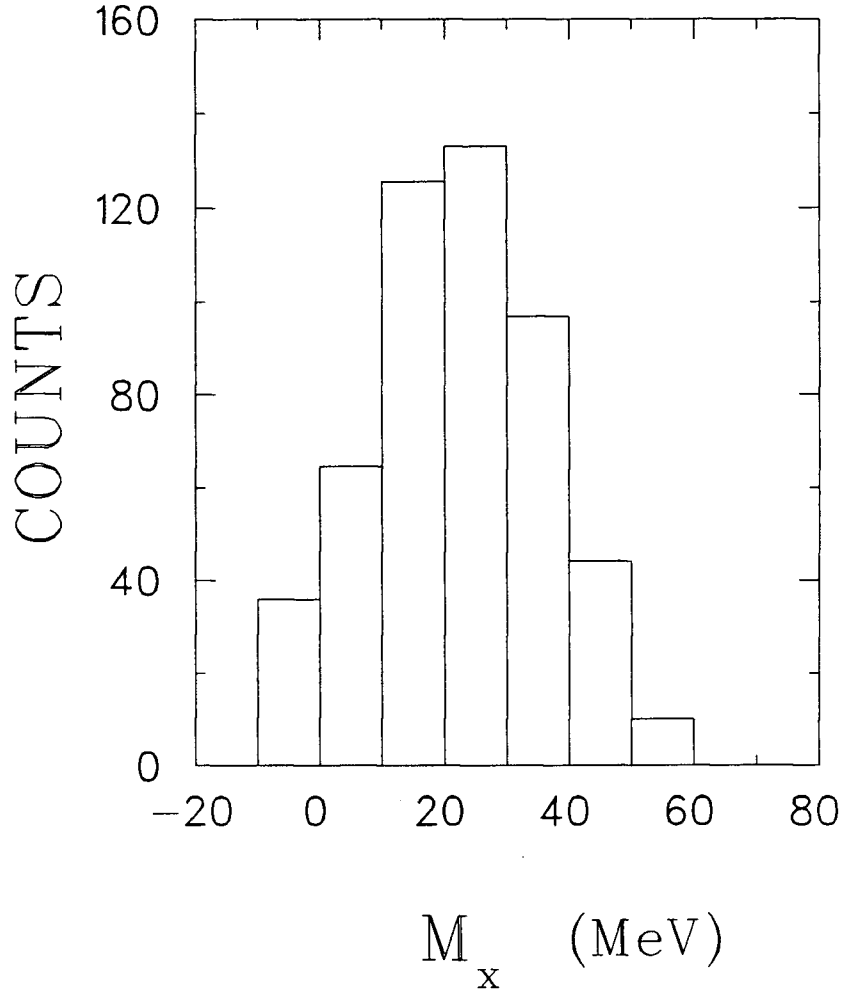


Figure 39: The missing mass spectrum for the two detected final state pions for the data set with the QCD at 50° .

of the total cross section demonstrates that the $(\pi, 2\pi)$ reaction provides a useful way to obtain information on the pion dispersion relation in the nuclear medium, $\tilde{\omega}(q)$, for outgoing pions of ($T_\pi < 100$ MeV).

The theoretical model is able to describe reasonably well three of the four measured kinematic quantities; $\theta_{\pi+}$, $\theta_{\pi-}$ and $T_{\pi-}$. The shape of the model distributions follow that of the phase-space of the quasi-free mechanism underlying the calculation. The agreement in spectra shapes indicates that the reaction is predominantly a quasi-free reaction. However, the unexpected low energy peaking of much of the $T_{\pi+}$ distribution data is not adequately described. The theoretical model did not include the presence of quasi-elastic collisions for the outgoing pions. The inclusion of such effects would be expected to lower the energies of the outgoing pions and might improve the model agreement with the data. Selected reaction mechanisms modelled with a Monte Carlo approach [Ols87] involving Δ 's in the intermediate state were found to be able to produce spectra with a low energy $T_{\pi+}$ peak, indicating that they may be important in properly describing the quasi-free mechanism in the reaction. These simulations were not however, able to consistently reproduce all the features of the measured spectra. As the simulation considered only the kinematical constraints in the mechanism and not details of the dynamics, it is not surprising that all features are not adequately described. Comparison of simulation results offered no indication that a substantial $\Delta\Delta$ mechanism was present in the data. It is expected that such $\Delta\Delta$ mechanisms will be more important in the $(\pi^+, 2\pi^+)$ reaction than the $(\pi^+, \pi^+\pi^-)$ reaction measured here.

The apparatus used in gathering the experimental data performed well. The low energy threshold of the CARUZ, 8 MeV, was found to be important, as a substantial part of the yield appeared with $T_{\pi+} < 15 - 20$ MeV, which is the approximate threshold for the apparatus used in the SIN measurement. The

CARUZ scintillators performed exceptionally well, providing a moderate resolution of ≤ 2 MeV and good angular resolution. In order to extend the dynamic range of the CARUZ, an additional slab of 5 cm thickness is to be added for the upcoming summer run which will measure the $(\pi, 2\pi)$ reaction in other nuclei as well as at different energies. This will have the benefit that more of the π^+ spectrum will be detected, reducing the uncertainties associated with extrapolating over the unmeasured phase-space. The wire chambers in the CARUZ faced large fluxes of particles and hence did not have a good efficiency. This created no analysis difficulties. The wire chamber information is potentially useful for tagging decaying pions and for improved production vertex determination. The next experimental run will employ better chambers capable of tolerating higher rates.

The QQD was able to cleanly identify pions with an intrinsic resolution of approximately 1.0 MeV. The first wire chamber encountered continual high particle fluxes which prevented the channel from being opened up further than $1\frac{1}{2}\%$ for more flux and reduced its efficiency. A PCOS chamber, similar to the chamber used in beam for counting the incident pions, will replace WC1 in the next run. It is also planned to take some data in future runs with the QQD set to accept lower momenta than measured here to further cover the phase-space. It would be advantageous to use a device with a larger solid angle and momentum acceptance than the QQD. This would shorten the required beam time to measure distributions.

The $^{16}\text{O}(\pi^+, \pi^+\pi^-)$ experiment performed resulted in the first publication [GRR*87] of coincidence data of good quality for the $(\pi, 2\pi)$ reaction on any nucleus. A paper describing the CARUZ detector in detail has also been published [RGR88]. A paper covering the full results of the oxygen data at 280 MeV has been submitted for publication [GRR*88] in the near future. This data represents the start of a program to study the $(\pi, 2\pi)$ reaction. There are still many

measurements possible. A study of the energy dependence of the reaction on ^{16}O would indicate if the model of [OV86] is valid over a range of energies. A study of the A dependence would provide information on how the medium effects change with the nuclear size. A coincident measurement of the $(\pi, 2\pi)$ reaction on the deuteron at various energies might help point out where the microscopic description of the free reaction could be improved to the point where a microscopic description of the nuclear process would be meaningful. The subject of $(\pi, 2\pi)$ in nuclei is still relatively unstudied.

Bibliography

- [AAL*84] D. Ashery, J. Alster, J. Lichtenstadt, E. Piasetzky, S.A. Wood, N.J. DiGiacomo, P.A.M. Gram, M.J. Leitch, P. McGughey, W.E. Sondheim, and J.W. Sunier. Study of the $(\pi, 2\pi)$ Reactions Near Threshold. 1984. SIN research proposal.
- [ABB*84] L.E. Antonuk, D. Bovet, E. Bovet, J.-P. Egger, J.-F. Germond, F. Goetz, P. Gretillat, C. Lunke, and E. Schwarz. Elastic and inelastic pion scattering on ^{12}C and ^{13}C at 100 MeV. *Nuclear Physics*, **A420**:435, 1984.
- [ACG*79] R.A. Arndt, J.B. Cammarata, Y.N. Goradia, R.H. Hackman, V.L. Teplitz, D.A. Dicus, R. Aaron, and R.S. Longacre. Isobar production in $\pi^- p \rightarrow \pi^+ \pi^- n$ near threshold. *Physical Review*, **D20**:651, 1979.
- [AEK71] F. Ashton, H.J. Edwards, and G.N. Kelly. The Technique of Mass Determination of Slow Cosmic Ray Particles Using a Large Aperature Range Telescope. *Nuclear Instruments and Methods*, **95**:109, 1971.
- [AJW*84] A. Altman, R.R. Johnson, U. Wienands, N. Hessey, B.M. Barnett, B.M. Forster, N. Grion, D. Mills, F.M. Rozon, G.R. Smith, R.P. Trelle, D.R. Gill, G. Sheffer, and T. Anderl. Observation of the Double Isobaric Analog Transition $^{18}\text{O}(\pi^+, \pi^-)^{18}\text{Ne}$ at 50 MeV. *Physical Review Letters*, **55**:1273, 1984.
- [ANA*81] D. Ashery, I. Navon, G. Azuelos, H.K. Walter, H.J. Pfeiffer, and F.W. Schlepütz. True absorption and scattering of pions on nuclei. *Physical Review*, **C23**:2173, 1981.
- [Bar85a] B.M. Barnett. 1985. Private Communication.
- [Bar85b] B.M. Barnett. *Nuclear Proton Radii from Low Energy Pion Scattering*. PhD thesis, University of British Columbia, 1985.
- [BBD*69] Yu. A. Batusov, S.A. Bunyatov, N. Dalkhazhav, G. Ionice, E. Losneanu, V. Mihul, V.M. Sidorov, D. Tuvdendorzh, and V.A. Yarba. Production of Mesons by Mesons and Double Charge Exchange of Negative Pions on Emulsion Nuclei in the Energy Interval 210–375 MeV. *Soviet Journal of Nuclear Physics*, **9**:221, 1969.

- [BCIR80] K.L. Brown, D.C. Carby, C.H. Iselin, and F. Rothaker. *TRANSPORT: a Computer Program for Designing Particle Beam Transport Systems*. Yellow report 80-04, CERN, 1980.
- [BGB*83] M. Blecher, K. Gotow, R.L. Burman, M.V. Hynes, M.J. Leitch, N.S. Chant, L. Rees, P.G. Roos, F.E. Bertrand, E.E. Gross, F.E. Obenshain, T.P. Sjoreen, G.S. Blanpied, B.M. Freedom, and B.G. Ritchie. Isospin effects in π^\pm elastic scattering from ^{12}C , ^{13}C , and ^{14}C at 65 and 80 MeV. *Physical Review*, **C28**:2033, 1983.
- [BGJ*79] M. Blecher, K. Gotow, D. Jenkins, F. Milder, F.E. Bertrand, T.P. Cleary, E.E. Gross, C.A. Ludemann, M.A. Moinester, R.L. Burman, M. Hamm, R.P. Redwine, M. Yates-Williams, S. Dam, C.W. Darden III, R.D. Edge, D.J. Malbrough, T. Marks, and B.M. Freedom. Positive pion-nucleus elastic scattering at 40 MeV. *Physical Review*, **C20**:1884, 1979.
- [BJK*80] C.W. Bjork, S.E. Jones, T.R. King, D.M. Manley, A.T. Oyer, G.A. Rebka, Jr., J.B. Walter, R. Carawon, P.A.M. Gram, F.T. Shivley, C.A. Bordner, and E.L. Lomon. Measurement of $\pi^-p \rightarrow \pi^+\pi^-n$ near Threshold and Chiral-Symmetry Breaking. *Physical Review Letters*, **44**:62, 1980.
- [BK85] A.W. Bennett and C. Kost. *MOLLI, Multi OffLine Interactive analysis*. 1985. TRIUMF Computing Document.
- [BL84] R.S. Bhalerao and L.C. Liu. Comparison of approximate chiral-dynamical $\pi N \rightarrow \pi\pi N$ models used in $A(\pi, 2\pi)$ calculations. *Physical Review*, **C30**:224, 1984.
- [BTWW82] G.E. Brown, H. Toki, W. Weise, and A. Wirzba. Double- $\Delta(1232)$ Formation in Pion-Nucleus Absorption. *Physics Letters*, **B118**:39, 1982.
- [CE83] J. Cohen and J.M. Eisenberg. The $(\pi, 2\pi)$ Reaction and Spin-Isospin Strength Distribution in Nuclei. *Nuclear Physics*, **A395**:389, 1983.
- [CGP*83] C. Cernigoi, N. Grion, G. Pauli, R. Rui, and R. Cherubini. A Counter for the Identification and the Energy Determination of Light Charged Particles and Neutrons of 20–100 MeV. *Nuclear Instruments and Methods*, **211**:129, 1983.
- [CS70] R.L. Craun and D.L. Smith. Analysis of Response Data for Several Organic Scintillators. *Nuclear Instruments and Methods*, **80**:239, 1970.

- [CSZ76] J.C. Comiso, F. Schlepuetz, and K.O.H. Ziock. An Unfolding Procedure for Charged Particle Spectra and Its Application to the Measurement of Stopping Power. *Nuclear Instruments and Methods*, **133**:121, 1976.
- [CW64] W. Czyż and J.D. Walecka. Electro-Production of Pions from Nuclei. *Nuclear Physics*, **51**:312, 1964.
- [DJDVDV74] C.W. De Jager, H. De Vries, and C. De Vries. Nuclear Charge- and Magnetization-Density-Distribution Parameters from Elastic Electron Scattering. *Atomic Data and Nuclear Data Tables*, **14**:479, 1974.
- [Eis80] J.M. Eisenberg. The $(\pi, 2\pi)$ Process as a Possible Probe of Pion Condensation Precursor Phenomena. *Physics Letters*, **93B**:12, 1980.
- [EM76] R.A. Eisenstein and G.A. Miller. DWPI: A Computer Program to Calculate the Inelastic Scattering of Pions from Nuclei. *Computer Physics Communications*, **11**:95, 1976.
- [FW71] A.L. Fetter and J.D. Walecka. *Quantum Theory of Many-Particle Systems*. McGraw-Hill Book Company, New York, 1971.
- [GKW79] M. Gyulassy, S.K. Kauffmann, and L.W. Wilson. Pion interferometry of nuclear collisions. I. Theory. *Physical Review*, **C20**:2267, 1979.
- [GRR*87] N. Grion, R. Rui, F.M. Rozon, T. Anderl, M. Hanna, R.R. Johnson, R. Olszewski, M.E. Sevier, R.P. Trelle, D.R. Gill, G. Sheffer, G.R. Smith, J. Ernst, Z. Wu, and J.J. Kraushaar. Measurement of the $^{16}\text{O}(\pi^+, \pi^+\pi^-)$ Reaction at $T_{\pi^+} = 280$ MeV. *Physical Review Letters*, **59**:1080, 1987.
- [GRR*88] N. Grion, R. Rui, F.M. Rozon, M. Hanna, R.R. Johnson, J. McAlister, R. Olszewski, C. Ponting, M.E. Sevier, V. Sossi, D.R. Gill, G. Sheffer, M.J. Vicente-Vacas, and E. Oset. Pion production by pions in the $^{16}\text{O}(\pi^+, \pi^+\pi^-)$ reaction at $T_{\pi^+} = 280$ MeV. *Nuclear Physics*, 1988. Submitted.
- [GT58] M.L. Goldberger and S.B. Treiman. Decay of the Pi Meson. *Physical Review*, **110**:1178, 1958.
- [Hag63] R. Hagedorn. *Relativistic Kinematics*. W.A. Benjamin, New York, 1963.
- [Hes85] N.P. Hessey. *The Pion Double Charge Exchange Reaction on ^{18}O at 50 MeV*. Master's thesis, University of British Columbia, 1985.

- [HFO*87] R. Henderson, W. Faszer, R. Openshaw, G. Sheffer, M. Saloman, S. Dew, J. Marans, and P. Wilson. A High Rate Proportional Chamber. *IEEE Transactions on Nuclear Science*, **NS-34**:528, 1987.
- [HGI*80] M. Haji-Saeid, C. Glashausser, G. Igo, W. Cornelius, M. Gazzaly, F. Irom, J. McClelland, J.M. Moss, G. Pauletta, H.A. Thiessen, and C.A. Whitten, Jr. Inelastic Proton Scattering to the ^{12}C 15.11-MeV State: A Search for Nuclear Critical Opalescence. *Physical Review Letters*, **45**:880, 1980.
- [Jam68] F. James. *Monte Carlo Phase Space*. Yellow Report 68-15, CERN, 1968.
- [JAS74] J.A. Jones, W.W.M. Allison, and D.H. Saxon. Measurement of the s-Wave, $I=0$ $\pi\pi$ Scattering Length. *Nuclear Physics*, **B83**:93, 1974.
- [KR83] C. Kost and P. Reeve. *REVMOC: a Monte Carlo beam transport program*. Internal report TRI-DN-83-28, TRIUMF, 1983.
- [LAW*86] J. Lichtenstadt, D. Ashery, S. Wood, E. Piasetzky, P.A.M. Gram, D.W. MacArthur, R.S. Bhalerao, L.C. Liu, G.A. Rebka, Jr., and D. Roberts. Pion-induced pion production on the deuteron. *Physical Review*, **C33**:655, 1986.
- [LMOP47] C.M.G. Lattes, H. Muirhead, G.P.S. Occhialini, and C.F. Powell. Processes Involving Charged Mesons. *Nature*, **159**:694, 1947.
- [LS78] C.M. Lederer and V.S. Shirley, editors. *Table of Isotopes*. John Wiley, New York, Seventh edition, 1978.
- [Man81] D.M. Manley. *Measurement and Isobar-Model Analysis of the Doubly Differential Cross Section for the π^+ produced in $\pi^-p \rightarrow \pi^+\pi^-n$* . PhD thesis, University of Wyoming, 1981. Los Alamos report LA-9101-T.
- [MBG*80] R.E. Mischke, A. Blomberg, P.A.M. Gram, J. Jansen, J. Zichy, J. Bolger, E. Boschitz, C.H.Q. Ingram, and G. Pröbstle. Inelastic Pion Double Charge Exchange on ^{16}O at 240 MeV. *Physical Review Letters*, **44**:1197, 1980.
- [MGB*80] J.M. Moss, C. Glashausser, F.T. Baker, R. Boudrie, W.D. Cornelius, N. Hintz, G. Hoffmann, G. Kyle, W.G. Love, A. Scott, and H.A. Thiessen. Excitation of Unnatural-Parity States in ^{12}C by 800-MeV Polarized Protons. *Physical Review Letters*, **44**:1189, 1980.
- [Mig78] A.B. Migdal. Pion fields in nuclear matter. *Reviews of Modern Physics*, **50**:107, 1978.

- [MMS76] B.R. Martin, D. Morgan, and G. Shaw. *Pion-Pion Interactions in Particle Physics*. Academic Press Inc., New York, 1976.
- [MSS*80] R.D. McKeown, S.J. Sanders, J.P. Schiffer, H.E. Jackson, M. Paul, J.R. Specht, E.J. Stephenson, R.P. Redwine, and R.E. Segel. How Many Nucleons are Involved in Pion Absorption in Nuclei. *Physical Review Letters*, 44:1033, 1980.
- [MSS*81] R.D. McKeown, S.J. Sanders, J.P. Schiffer, H.E. Jackson, M. Paul, J.R. Specht, E.J. Stephenson, R.P. Redwine, and R.E. Segel. Inclusive reactions of pions on nuclei. *Physical Review*, C24:211, 1981.
- [MVEL*84] C.J. Martoff, L. Van Elmbt, M. Lebrun, M. Schaad, U. Straumann, P. Truöl, K.M. Crowe, C. Joseph, J.P. Perroud, D. Ruegger, M.T. Tran, J. Deutsch, G. Grégoire, and R. Prieels. No Pre-Critical Enhancement Observed in $^{13}\text{C}(\pi^+, \gamma)^{13}\text{N}(g.s.)$ at $q \cong 2m_\pi$. *Nuclear Physics*, A430:557, 1984.
- [NE86] *Scintillators for the Physical Sciences*. Nuclear Enterprises.
- [NRDS*79] M.M. Nagels, Th.A. Rijken, J.J. De Swart, G.C. Oades, J.L. Peterson, A.C. Irving, C. Jarlskog, W. Pfeil, H. Pilkuhn, and H.P. Jakob. Compilation of Coupling Constants and Low-Energy Parameters. *Nuclear Physics*, B147:189, 1979.
- [Ols87] R. Olszewski. 1987. Private Communication.
- [OS85] E. Oset and L.L. Salcedo. Mesonic and Non-Mesonic Λ -Decay in Nuclei. *Nuclear Physics*, A443:704, 1985.
- [OSVW83] E. Oset, D. Strottman, M.J. Vicente-Vacas, and Ma Wei-Hsing. Meson-Exchange Currents in Pion-Nucleus Double-Charge-Exchange Reactions. *Nuclear Physics*, A408:461, 1983.
- [OT69] M.G. Olsson and L. Turner. Consistency of Low-Energy Parameters and Soft-Pion Scattering Theory. *Physical Review*, 181:2141, 1969.
- [OTW82] E. Oset, H. Toki, and W. Weise. Pionic Modes of Excitation in Nuclei. *Physics Reports*, 83:281, 1982.
- [OV85] E. Oset and M.J. Vicente-Vacas. A Model for the $\pi^- p \rightarrow \pi^+ \pi^- n$ Reaction. *Nuclear Physics*, A446:584, 1985.
- [OV86] E. Oset and M.J. Vicente-Vacas. Inclusive $(\pi, 2\pi)$ Reactions in Nuclei. *Nuclear Physics*, A454:637, 1986.

- [OV87] E. Oset and M.J. Vicente-Vacas. 1987. Private Communication.
- [OW76] E. Oset and W. Weise. Renormalization of the π NN-Vertex in a Nuclear Medium. *Physics Letters*, **60B**:141, 1976.
- [OWMD83] C.J. Oram, J.B. Warren, G.M. Marshall, and J. Doornbos. Commissioning of a New Low Energy $\pi - \mu$ Channel at TRIUMF. *Nuclear Instruments and Methods*, **179**:95, 1983.
- [PCE*77] J. Piffaretti, R. Corfu, J.-P. Egger, P. Gretillat, C. Lunke, E. Schwarz, and C. Perrin. π^+ and π^- Scattering from ^{12}C at 150 MeV. *Physics Letters*, **67B**:289, 1977.
- [PDD*81] B.M. Freedom, S.H. Dam, C.W. Darden, R.D. Edge, D.J. Malbrough, T. Marks, R.L. Burman, M. Hamm, M. Moinester, R.P. Redwine, M.A. Yates, F.E. Bertrand, T. Cleary, E. Gross, N. Hill, C. Ludemann, M. Blecher, K. Gotow, D. Jenkins, and F. Milder. Positive pion-nucleus elastic scattering at 30 and 50 MeV. *Physical Review*, **C23**:1134, 1981.
- [PGM*84] E. Piasetzky, P.A.M. Gram, D.W. MacArthur, G.A. Rebka, Jr., C.A. Bordner, S. Høibråten, E.R. Kinney, J.L. Matthews, S.A. Wood, D. Ashery, and J. Lichtenstadt. Pion-Induced Pion Production on the Deuteron. *Physical Review Letters*, **53**:540, 1984.
- [REF*77] L. Rosselet, P. Extermann, J. Fischer, O. Guisan, R. Mermoud, R. Sachot, A.M. Diamant-Berger, P. Bloch, G. Bunce, B. Devaux, N. Do-Duc, G. Marel, and R. Turley. Experimental study of 30000 K_{e4} decays. *Physical Review*, **D15**:574, 1977.
- [RGR88] F.M. Rozon, N. Grion, and R. Rui. A Total Absorption Range Telescope - The CARUZ. *Nuclear Instruments and Methods*, **A267**:101, 1988.
- [Ric63] J.R. Richardson. Design criteria for a 700 MeV cyclotron to accelerate negative hydrogen ions. *Nuclear Instruments and Methods*, **24**:493, 1963.
- [Roc75] R. Rockmore. Threshold pion production in pion-nucleus collisions: A simple estimate. *Physical Review*, **C11**:1953, 1975.
- [Roc83] R.M. Rockmore. Threshold estimates of $(\pi, 2\pi)$ on nuclei in the Fermi gas model: One-body mechanism. *Physical Review*, **C27**:2150, 1983.
- [Roc84] R. Rockmore. Comparison of a two-body threshold $(\pi, 2\pi)$ mechanism with the usual one-body mechanism in the deuteron. *Physical Review*, **C29**:1534, 1984.

- [Roz85] F.M. Rozon. *Elastic Pion Scattering at 50 MeV on ^{40}Ca and ^{48}Ca* . Master's thesis, University of British Columbia, 1985.
- [RSM68] C. Richard-Serré, M.J.M. Saltmarsh, and D.F. Measday. Long Čerenkov counters made of solid and liquid materials. *Nuclear Instruments and Methods*, **63**:173, 1968.
- [Sar86] S. Sarkar. *PBX*. 1986. Internal Triumf Documentation.
- [Sch84] F. Scheck. *Leptons, Hadrons and Nuclei*. North-Holland Physics Publishing, Amsterdam, 1984.
- [SDB*84] R.J. Sobie, T.E. Drake, B.M. Barnett, K.L. Erdman, W. Gyles, R.R. Johnson, H.W. Roser, R. Tacik, E.W. Blackmore, D.R. Gill, S. Martin, C.A. Wiedner, and T. Masterson. The TRIUMF Low Energy Pion Spectrometer and Channel. *Nuclear Instruments and Methods*, **219**:501, 1984.
- [SDE*84] R.J. Sobie, T.E. Drake, K.L. Erdman, R.R. Johnson, H.W. Roser, R. Tacik, E.W. Blackmore, D.R. Gill, S. Martin, C.A. Wiedner, and T. Masterson. Elastic and inelastic scattering of 50 MeV pions from ^{12}C , ^{32}S and ^{34}S . *Physical Review*, **C30**:1612, 1984.
- [SMC79] K. Stricker, H. McManus, and J.A. Carr. Nuclear scattering and low energy pions. *Physical Review*, **C19**:929, 1979.
- [Smi87] G. Smith. *The STAR Online Data Acquisition System*. Technical documentation, TRIUMF, 1987.
- [Sob84] R.J. Sobie. *Elastic and Inelastic Scattering of Low Energy Pions from ^{12}C , ^{32}S and ^{34}S* . PhD thesis, University of Toronto, 1984.
- [SWB83] B. Schwesinger, A. Wirzba, and G.E. Brown. Double- Δ excitation in pion absorption on ^4He . *Physics Letters*, **132B**:269, 1983.
- [TUH87] *TRIUMF User's Handbook*. Second edition, 1987.
- [Wei66] S. Weinberg. Pion Scattering Lengths. *Physical Review Letters*, **17**:616, 1966.
- [Wei67] S. Weinberg. Dynamical Approach to Current Algebra. *Physical Review Letters*, **18**:188, 1967.
- [Woo84] S.A. Wood. *An Experimental Study of Inclusive Pion Double Charge Exchange Reactions in the Delta Resonance Region*. PhD thesis, Massachusetts Institute of Technology, 1984. Los Alamos report LA-9932-T.

[Yuk35]

H. Yukawa. On the Interaction of Elementary Particles. I.
Proceedings of the Physico-Mathematical Society of Japan, 17:48,
1935.

Appendix A

Tabulations of Differential Cross Sections

This appendix contains tabulations of all the cross sections shown in the text figures. The first group of tables contains the data as presented in section III.2.2 in the form used for the cross section integrations. The second group contains cross sections of subsets of the QQD-CARUZ momentum/angle settings. In the case where only a subset of the data for a particular QQD angle is given, the extrapolation factors over the integrated variables has been performed in a manner similar to that used to integrate the entire data set of each QQD angle as discussed in section III.2.2. The errors quoted contain the statistical errors and the errors from extrapolations. The remaining errors are quoted as the overall normalization error and include the uncertainties shown in Table VIII.

T_{π^+}	$\theta_{\pi^-} = 50^\circ$		$\theta_{\pi^-} = 80^\circ$		$\theta_{\pi^-} = 115^\circ$	
10.0	2.905	0.201	1.754	0.156	0.494	0.105
14.0	5.402	0.274	2.424	0.183	0.528	0.109
18.0	5.091	0.261	2.537	0.187	0.479	0.106
22.0	3.897	0.232	2.210	0.175	0.586	0.116
26.0	2.825	0.199	1.514	0.145	0.500	0.108
30.0	2.196	0.182	1.557	0.147	0.683	0.124
34.0	2.291	0.178	1.264	0.132	0.602	0.116
38.0	1.849	0.160	1.114	0.124	0.584	0.115
42.0	1.638	0.151	1.134	0.124	0.569	0.114
46.0	1.375	0.136	0.894	0.110	0.476	0.103
50.0	1.019	0.121	0.897	0.111	0.497	0.103
54.0	0.488	0.070	0.472	0.099	0.391	0.092
58.0	0.351	0.067	0.408	0.084	0.223	0.072
62.0	0.147	0.045	0.290	0.063		
Norm. Errors (%)	13.6		12.8		12.8	

Table IX: The four-fold differential cross section (units of nb/(sr² MeV²)) as a function of T_{π^+} for the three QCD angle settings. The data includes both QCD momentum settings and both CARUZ angle settings.

T_{π^-}	$\theta_{\pi^-} = 50^\circ$		$\theta_{\pi^-} = 80^\circ$		$\theta_{\pi^-} = 115^\circ$	
36.5	303.418	26.940	302.458	21.573		
39.5	299.560	26.742	302.720	21.613		
42.5	325.360	28.044	311.871	22.000		
45.5	295.151	26.517	299.091	21.410		
48.5	326.952	28.124	311.983	22.027		
51.5	309.358	27.241	300.760	21.518		
54.5	312.093	27.380	254.340	19.517		
57.5	304.214	26.981	214.724	17.566		
60.5	284.905	25.979	241.957	18.904		
63.5	246.163	23.928	180.449	15.909	56.059	10.978
66.5	232.692	23.185	141.985	17.734	59.749	11.352
69.5	205.197	21.622	128.170	16.864	33.277	8.371
72.5	222.853	22.541	138.360	17.489	29.993	7.935
75.5	202.646	21.474	134.651	17.244	44.503	9.730
78.5	153.699	18.471	107.071	15.381	59.543	11.252
81.5	161.884	18.993	100.439	14.966	34.604	8.541
84.5	119.653	16.148	103.838	14.738	24.290	7.122
87.5	116.489	15.922	85.067	13.461	20.412	6.593
90.5	130.675	16.925	72.337	12.412	28.227	7.691
93.5	91.423	14.010	94.846	14.278	32.318	8.246
96.5	67.848	11.992	68.914	12.455	42.576	9.518
99.5	113.570	15.707	57.621	10.759	30.279	7.813
102.5	45.859	9.911	59.408	11.207	43.641	9.631
105.5	42.905	9.472	24.384	7.106	21.653	6.299
Norm. Errors (%)	14.0		13.3		13.5	

Table X: The triple differential cross section (units of nb/(sr² MeV)) as a function of T_{π^-} for the three QCD angle settings. The data includes both CARUZ angle settings.

θ_{π^+}	$\theta_{\pi^-} = 50^\circ$		$\theta_{\pi^-} = 80^\circ$		$\theta_{\pi^-} = 115^\circ$	
25.000	16.563	1.708			40.145	5.407
31.000	22.207	2.000	25.000	1.739	33.832	5.036
37.000	22.891	2.030	30.644	2.009	29.389	4.693
43.000	21.812	1.982	30.661	2.039	26.592	4.465
49.000	21.936	1.904	27.660	1.948	24.483	4.284
55.000	25.041	2.124	26.606	1.887	17.487	3.620
61.000	24.750	2.111	25.888	1.851	16.181	3.483
67.000	24.407	2.097	23.892	1.715	11.326	2.914
73.000	21.313	1.959	20.761	1.615	5.536	2.037
79.000	18.587	1.822	14.998	1.369	5.996	2.084
85.000	21.447	1.965	15.106	1.455	5.696	2.023
91.000	17.208	1.760	13.636	1.398	0.000	0.000
97.000	19.615	1.880	11.581	1.290	0.000	0.000
103.000	20.692	1.930	11.093	1.243	0.000	0.000
109.000	18.035	1.802	9.443	1.148	1.623	1.103
115.000	19.530	1.876	7.112	0.981	0.000	0.000
121.000	15.689	1.721	3.827	0.729	0.000	0.000
127.000	13.285	1.551	2.568	0.565		
Norm. Errors (%)	15.0		14.1		26.7	

Table XI: The double differential cross section (units of $\mu\text{b}/\text{sr}^2$) as a function of θ_{π^+} for the three QCD angle settings. The data includes both QCD momentum settings.

T_{π^+}	$\theta_{\pi^-} = 50^\circ$		$\theta_{\pi^-} = 80^\circ$		$\theta_{\pi^-} = 115^\circ$	
10.0	2.720	0.351	3.583	0.403	0.706	0.179
14.0	3.645	0.404	4.546	0.456	0.820	0.193
18.0	3.748	0.363	3.777	0.415	0.767	0.192
22.0	3.274	0.385	2.809	0.357	0.972	0.210
26.0	2.188	0.315	1.990	0.300	0.999	0.216
30.0	2.287	0.322	1.731	0.280	1.156	0.229
34.0	1.641	0.273	1.377	0.250	1.097	0.222
38.0	0.983	0.211	0.933	0.206	0.969	0.209
42.0	0.509	0.152	1.024	0.215	1.138	0.228
46.0	0.895	0.201	0.719	0.173	0.951	0.207
50.0	0.647	0.171	0.777	0.187	0.994	0.207
54.0	0.373	0.130	0.575	0.155	0.682	0.171
58.0	0.339	0.124	0.529	0.155	0.446	0.145
62.0	0.133	0.078	0.717	0.180		
Norm. Errors (%)	13.6		12.8		12.8	

Table XII: The four-fold differential cross section (units of nb/(sr² MeV²)) as a function of T_{π^+} for the three QCD angle settings. The data includes only the high QCD momentum, 50° CARUZ setting.

θ_{π^+}	$\theta_{\pi^-} = 50^\circ$		$\theta_{\pi^-} = 80^\circ$		$\theta_{\pi^-} = 115^\circ$	
25.000	153.690	17.863			101.688	14.409
31.000	166.980	18.688	88.986	13.366	85.696	13.301
37.000	190.238	20.075	125.743	16.065	74.443	12.332
43.000	193.655	20.293	113.972	15.241	67.358	11.691
49.000	160.487	18.289	104.270	14.536	62.015	11.189
55.000	186.991	19.885	102.239	14.347	44.294	9.375
61.000	161.474	18.349	114.769	15.516	40.987	9.004
67.000	188.985	20.002	113.763	15.227	28.689	7.488
73.000	169.144	18.821	94.435	13.789	14.022	5.196
79.000	162.348	18.403	87.608	15.457	15.189	5.320
85.000	169.031	18.814	81.452	16.200	14.428	5.164
91.000	130.964	16.384	68.986	14.935	0.000	0.000
97.000	146.950	19.262	61.234	14.213	0.000	0.000
103.000	137.381	16.811	65.620	14.733	0.000	0.000
109.000	136.736	16.769	53.759	13.247	4.110	2.799
115.000	114.257	15.233	45.393	12.208	0.000	0.000
121.000	108.162	14.795	22.353	8.530	0.000	0.000
127.000	85.645	13.079	20.374	8.141		
Norm. Errors (%)	14.0		13.3		13.5	

Table XIII: The triple differential cross section (units of nb/sr²) as a function of θ_{π^+} for the three QQD angle settings. The data includes only the high QQD momentum, 50° CARUZ setting.

T_{π^-}	$\theta_{\pi^-} = 50^\circ$		$\theta_{\pi^-} = 80^\circ$		$\theta_{\pi^-} = 115^\circ$	
36.5	327.750	38.289	368.489	16.878		
39.5	336.881	38.862	357.581	16.535		
42.5	341.384	39.146	356.977	16.516		
45.5	306.910	36.953	306.877	14.951		
48.5	362.306	40.437	387.672	17.484		
51.5	363.371	40.503	354.862	16.449		
54.5	337.904	38.931	313.149	15.146		
57.5	297.493	36.336	273.802	13.929		
60.5	333.769	38.670	358.539	16.565		
63.5	244.676	32.728	273.124	13.908	102.358	20.961
66.5	260.603	33.845	216.745	13.398	91.541	19.774
69.5	245.373	32.774	187.397	12.507	66.750	16.790
72.5	243.940	32.674	238.695	14.064	60.162	15.916
75.5	217.449	30.742	219.771	13.490	80.429	18.489
78.5	181.255	27.940	171.118	12.061	92.728	19.726
81.5	211.635	30.305	177.947	12.301	60.412	15.951
84.5	135.481	23.997	161.689	11.610	39.469	12.830
87.5	123.567	22.883	151.011	11.371	40.943	13.225
90.5	179.331	27.774	108.041	10.021	56.620	15.428
93.5	121.233	22.659	164.817	11.817	64.825	16.540
96.5	88.560	19.279	124.627	10.706	63.577	16.398
99.5	107.025	21.248	99.754	9.617	60.735	15.673
102.5	35.240	12.072	92.618	9.499	55.462	15.265
105.5	52.899	14.829	33.670	7.033	43.433	12.636
Norm. Errors (%)	14.0		13.3		13.5	

Table XIV: The triple differential cross section (units of nb/(sr² MeV)) as a function of T_{π^-} for the three QCD angle settings. The data includes only the 50° CARUZ angle setting.

Appendix B

Delta Coefficients

A tabulation of the set of delta coefficients used in the analysis of the experimental data to calculate the particle momentum from the QGD front wire chamber coordinates and one of the coordinates of the back end wire chambers. The form of the expansion for the calculation is, for example, for wire chamber 4,

$$x_4 = \sum_{i=1}^n \alpha_i \delta_4^{\eta_i} x_1^{\beta_i} y_1^{\gamma_i} x_3^{\epsilon_i} y_3^{\zeta_i}$$

where n is the number of coefficients in the set for x_4 . This particular coefficient set is called THREE.OUT.

i	α	η	β	γ	ϵ	ζ
1	-.298478279 E+02	0	0	0	0	0
2	0.165455592 E+01	0	0	0	1	0
3	-.823383331 E+00	0	1	0	0	0
4	0.570375333 E-02	0	0	0	0	2
5	-.717445789 E-02	0	0	0	2	0
6	-.169646312 E-01	0	0	1	0	1
7	0.180931203 E-01	0	0	2	0	0
8	-.614585733 E+01	1	0	0	0	0
9	0.390106142 E-01	1	0	0	1	0
10	-.167621728 E-01	1	1	0	0	0
11	0.466610509 E-04	1	0	0	0	2
12	-.100528581 E-03	1	0	1	0	1
13	-.119638353 E-03	1	1	0	1	0
14	-.431974004 E-04	1	1	1	0	0
15	-.601753054 E-04	1	2	0	0	0
16	0.402660221 E-01	2	0	0	0	0
17	0.111848320 E-03	2	0	0	0	1
18	-.747158658 E-03	2	0	0	1	0
19	-.256567379 E-03	2	0	1	0	0

Table XV: Coefficients for the δ_4 calculation in terms of the front wire chamber coordinates and WC4X with terms to second order in chamber coordinates and in δ .

i	α	η	β	γ	ϵ	ζ
1	-.435179443 E+02	0	0	0	0	0
2	0.111518192 E+01	0	0	0	1	0
3	-.882024288 E+00	0	1	0	0	0
4	0.456649205 E-02	0	0	0	0	2
5	-.120490678 E-01	0	0	0	2	0
6	-.439064065 E-02	0	0	1	0	1
7	0.216105618 E-03	0	0	1	1	0
8	0.635596877 E-02	0	1	0	1	0
9	-.182520598 E-02	0	1	1	0	0
10	-.912979603 E+01	1	0	0	0	0
11	0.213439504 E-03	1	0	0	0	1
12	0.564717874 E-01	1	0	0	1	0
13	0.323678796 E-04	1	0	0	0	2
14	-.745056677 E-04	1	0	0	2	0
15	-.216389046 E-03	1	1	1	0	0
16	0.563120432 E-01	2	0	0	0	0
17	-.982195721 E-03	2	0	0	1	0
18	-.138998526 E-03	2	0	1	0	0
19	0.113418128 E-02	2	1	0	0	0

Table XVI: Coefficients for the δ_5 calculation in terms of the front wire chamber coordinates and WC5X.